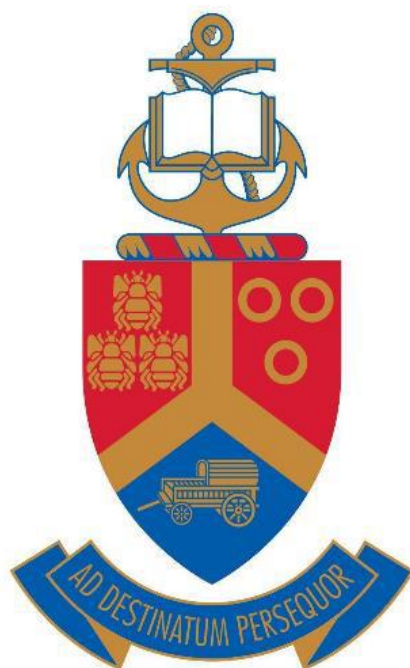


Synthesis and characterization of gold and silver nanoparticles for enhanced light collection in organic solar cells

by

Thapelo Ephraim Seimela



Submitted in partial fulfilment of the requirements for the degree

Magister Scientiae
In the Faculty of Natural and Agricultural Science
Department of Physics


Supervisor: Prof. M. M. Diale

Co-supervisor: Dr. N. Nombona

February 2022

DECLARATION

I, THAPELO EPHRAIM SEIMELA, declare that the dissertation, I hereby submit for the degree Magister Scientiae (MSc) in the department of Physics at the University of Pretoria is my work and has not been submitted previously by me for a degree at this or any other institution.

Signature 

Date 15/02/2022

DEDICATION

This dissertation is dedicated to:

My mother Mary Seimela

My sisters Tokologo, Temošo

and Kopano Seimela

ACKNOWLEDGEMENTS

- ❖ I would like to thank my supervisor, Prof. Mmantsae Diale, for her guidance, motivation, efforts, and support in helping me complete this research project.
- ❖ I would also like to thank my co-supervisor, Dr Nolwazi Nombona for her guidance with nanotechnology.
- ❖ Special thanks to Green and Clean Energy group seniors (Dr Alex Paradzah, Dr Juvet Fru, Dr Justine Nyarige and Dr Pannan Kyesmen) and fellow students (Sandile Thubane, Sizwe Sibiyi, William Pooe, Adiel Holtzhauzen, Shalot Ngunyulu Siphesihle Mguni and others) for their assistances in the lab and keeping the lab pleasant.
- ❖ I would like to express my gratitude to the Nanotechnology group (Lebo Manamela, Nokubongwa Dlamini, Lu-Nita Berrange, Ronald Nguluvhe, and others) for their assistance with nanotechnology.
- ❖ I would like to express my heartfelt gratitude to my wonderful family for their big support and understanding.
- ❖ I would like to thank the Microscopy and microanalysis for using FEG-SEM and HRTEM for analysis.
- ❖ I would like to thank the Head of the Department of Physics, Prof. Chris Theron for allowing me to study in his department.
- ❖ Finally, I would like to thank National Research Fund for financial assistance.

ABSTRACT

The study aims to synthesize plasmonic nanoparticles (NPs) using the chemical reduction method and incorporate them into poly(3,4-ethylene dioxythiophene): poly(styrene sulfonate) (PEDOT: PSS) for light scattering. The plasmonic NPs were chosen because of their remarkable physical, chemical, and optical properties. Chloroauric acid, silver nitrate and copper sulphate were reduced by sodium borohydride to obtain gold (Au), silver (Ag) and copper (Cu) NPs, respectively. Transmission electron microscopy (TEM), scanning electron microscopy (SEM), X-ray diffraction (XRD) and ultraviolet-visible spectroscopy were used to characterize the samples. The TEM results show spherical shapes of Au and AgNPs with average grain sizes of 23.7 ± 0.5 and 5.0 ± 1.2 nm, respectively. The grain sizes of CuNPs containing 5, 10, and 15 mM CuSO_4 are 6.01 ± 0.89 nm, 17.32 ± 0.55 nm, and 32.00 ± 0.75 nm, respectively.

The NPs were deposited in PEDOT: PSS and spin-coated on a glass substrate followed by the blend of poly(3-hexylthiophene): phenyl- C_{61} -butyric acid methyl (P3HT: PCBM) ester. The UV-Vis spectroscopy revealed that NPs are absorbing in the visible range by showing plasmonic resonance at approximately 534 nm for Au, 408 nm for Ag and 560 for Cu NPs along with peaks of PEDOT: PSS, PCBM and P3HT at 353, 333 and 445 nm respectively. The X-ray diffraction (XRD) patterns confirmed the FCC structure of both NPs with (111), (200), (220), and (310) phases in which the (111) peak was the most intense. From Raman spectroscopy measurements, the main peaks associated with P3HT: PCBM, PEDOT: PSS were observed. Organic solar cells (OSC) with and without nanostructures were fabricated with P3HT: PCBM as the active layer, and PEDOT: PSS as a hole transport layer. The current-density (J - V) characterizations were performed. From the J - V measurements, the OSCs containing 20 μL of CuNPs had the highest efficiency of 8.77 %. From this study, NPs showed the potential to improve light absorption in OSCs.

Table of Contents

DECLARATION	ii
DEDICATION	iii
ACKNOWLEDGEMENTS	iv
ABSTRACT	v
Table of Contents	vi
List of Figures	ix
List of Tables	xii
Chapter 1	1
1 Introduction	1
1.1 Background and motivation	1
1.2 Aim and objectives	4
1.3 Structure of the dissertation	4
1.4 References	5
Chapter 2	9
2 Plasmonic nanoparticles	9
2.1 Introduction	9
2.2 Metal nanoparticles: Properties and their significance	9
2.2.1 Noble metal nanoparticles	9
2.3 Synthesis of noble metal nanoparticles	10
2.3.1 Top-down Approaches	10
2.3.2 Bottom-up Approaches	12
2.4 Characterization of nanoparticles	23
2.5 Applications of noble metal nanoparticles	23
2.5.1 Gold nanoparticles	23
2.5.2 Silver nanoparticles	28

2.5.3	Platinum nanoparticles	30
2.6	Noble metal nanoparticles in organic solar cells.....	31
2.6.1	Properties of organic solar cells	31
2.6.2	Architecture of OSC	33
2.6.3	Plasmonic principles	33
2.7	Plasmonics in organic solar cells	35
2.7.1	Metal nanoparticles in the buffer layer	35
2.7.2	Metal nanoparticles in the active layer	35
2.8	References	37
Chapter 3.....		46
3	Experimental.....	46
3.1	Materials.....	46
3.2	Synthesis of gold and silver nanoparticles	46
3.2.1	Gold NPs.....	46
3.2.2	Silver NPs	46
3.2.3	Copper NPs	46
3.3	Substrate cleaning	47
3.4	Fabrication of solar cell.....	47
3.5	Characterization	48
3.5.1	X-ray diffraction (XRD)	48
3.5.2	Scanning Electron Microscopy (SEM)	49
3.5.3	Transmission Electron Microscopy (TEM)	50
3.5.4	Raman spectroscopy	52
3.5.5	Ultraviolet-visible (UV-Vis)	53
3.6	Electrical characterization.....	54
3.6.1	Dark current-voltage (I-V) measurements.....	54
3.6.2	Light Current density-voltage (J – V) measurements of the solar cells.....	55

3.7	References	56
Chapter 4.....		58
4	Results and discussion	58
4.1	Introduction	58
4.2	Gold and silver nanoparticles	58
4.2.1	Structural, optical and morphological properties	58
4.3	Copper nanoparticles.....	63
4.3.1	Structural, optical and morphological properties.....	63
4.4	Organic solar cell	66
4.4.1	Structural, optical, morphological properties, and electrical properties	66
4.5	Conclusions	76
4.6	References	77
Chapter 5.....		80
5	Conclusions and future work.....	80
5.1	Conclusions	80
5.2	Future work	82

List of Figures

Figure 1.1: Timeline of best research solar cell efficiencies adapted from National Research Energy Laboratory	2
Figure 2.1: Schematic illustration of micropatterning of metallic nanoparticles using different polymer substrates	11
Figure 2.2: Schematic illustration of using attrition method for synthesizing metal nanoparticles.	12
Figure 2.3: Schematic illustration for chemical reduction of Ag^+ to silver nanoparticles.....	13
Figure 2.4: Schematic diagram of microemulsion method of synthesizing metal nanoparticles	15
Figure 2.5: Schematic diagram for the synthesis of gold nanoparticles using laser ablation ..	16
Figure 2.6: Schematic illustration for using nitrate reductase as a reducing agent during synthesis of silver nanoparticles	17
Figure 2.7: Reduction of AgNO_3 to silver nanoparticles by fungi	20
Figure 2.8: Synthesis of metallic nanoparticles by using plant extract.....	22
Figure 2.9: Schematic illustration of the physiological and biological effects of gold nanoparticle-mediated photothermal and photodynamic therapy.....	26
Figure 2.10: Schematic illustration for purification of water using bactericidal paper containing silver nanoparticles.	30
Figure 2.11: Flexibility of organic solar cells in (a) rolled around and (b) wrapped around human hair.	32
Figure 2.12: Plasmonic light scattering in solar cells using metal nanoparticles as (a) bulk plasmons, (b) localised surface plasmons and (c) surface plasmons polaritons.....	34
Figure 3.1: Schematic diagram of OSC incorporated with NPs in the PEDOT: PSS	47
Figure 3.2: Image of German Bruker D2 PHASER X-ray diffractometer	49
Figure 3.3: Images of field emission scanning electron microscope (FE-SEM Zeiss SEM Microscope Crossbeam-540)	50
Figure 3.4: Image of field emission gun transmission electron microscope (FEG-TEM, Jeol 2100).	51
Figure 3.5: WITec's Raman microscope alpha300 RAS	53
Figure 3.6: Image of Agilent Cary 60 UV-Vis Spectrophotometer.....	54
Figure 3.7: Shows a picture of the Oriel Cornerstone, Newport solar simulator alongside the Keysight source measure unit (SMU) connected to a computer.....	55

Figure 4.1: XRD patterns of (a) Au NPs with (i) 0.1 M NaBH ₄ and (ii) without NaBH ₄ and (b) Ag NPs with (i) 10 mM NaBH ₄ and 5 mM NaBH ₄	59
Figure 4.2: UV-Vis spectra of (a) Au NPs with (i) 0.1 M NaBH ₄ and (ii) without NaBH ₄ and (b) Ag NPs with (i) 10 mM NaBH ₄ and 5 mM NaBH ₄	61
Figure 4.3: TEM images of Ag NPs with (a) 10 mM NaBH ₄ and (b) 5 mM NaBH ₄ along with Au NPs with (a) 0.1 M NaBH ₄ and (b) without NaBH ₄	62
Figure 4.4: XRD patterns of Cu NPs at different concentrations of CuSO ₄	63
Figure 4.5: UV-Vis spectra of Cu NPs prepared without AA (a) immediately, (b) after 1 day and prepared with AA at (c) 5 mM, (d) (i) 10 mM and (ii) 15 mM CuSO ₄	65
Figure 4.6: TEM images of Cu NPs with AA at (a) 5 mM, (b) 10 mM and (c) 15 mM CuSO ₄	66
Figure 4.7: Raman spectra of PEDOT: PSS for (a) pristine, (b) different volumes of Cu NPs, and (c) different annealing temperatures. Raman spectra of P3HT: PCBM for (a) pristine, (b) different volumes of Cu NPs, and (c) different annealing temperatures.	67
Figure 4.8: UV-Vis spectra of (a) pristine PEDOT: PSS and (b) PEDOT: PSS containing different volumes of Cu NPs.....	68
Figure 4.9: UV-Vis spectra of (a) pristine P3HT: PCBM and (b) P3HT: PCBM containing different volumes of Cu NPs.....	69
Figure 4.10: UV-Vis spectra of Cu NPs incorporated in (a) P3HT: PCBM and (b) PEDOT: PSS annealed at different temperatures	70
Figure 4.11: SEM images of Cu NPs incorporated in P3HT: PCBM for (a) 10 μL, (b) 20 μL and 30 μL; and PEDOT: PSS for (d) 10 μL, (e) 20 μL and (d) 30 μL.....	71
Figure 4.12: SEM images of Cu NPs incorporated in P3HT: PCBM at annealing temperatures of (a) 120 °C, (b) 140 °C and 160 °C; and PEDOT: PSS at annealing temperatures of (d) 120 °C, (e) 140 °C and (f) 160 °C.	71
Figure 4.13: J–V characteristic curves under illumination that compared the performance of OSC of (a) pristine and (b) Au NPs	72
Figure 4.14: J–V characteristic curves under illumination that compared the performance of OSC measured on the same day for (a) pristine, (b) 10 μL Cu NPs, (c) 20 μL Cu NPs, and (d) 30 μL Cu NPs.....	73
Figure 4.15: J–V characteristic curves under illumination that compared the performance of OSC measured after 1 week for (a) pristine, (b) 10 μL Cu NPs, (c) 20 μL Cu NPs, and (d) 30 μL Cu NPs.....	74

Figure 4.16: J–V characteristic curves under illumination that compared the performance of OSC at annealing temperatures of (a) 120 °C, (b) 140 °C and 160 °C.76

List of Tables

Table 4.1: XRD analysis of Au and Ag NPs at different concentrations of NaBH ₄	60
Table 4.2: XRD analysis of the obtained Cu NPs.....	64
Table 4.3: Summary of the obtained photovoltaic parameters from the J-V data for OSCs ...	75

Chapter 1

Introduction

1.1 Background and motivation

There is a consistent increase in energy demand with a projection of a 60 % rise expected by 2030 [1]. Fossil fuels are the primary energy source that accounts for 87 % of global energy usage. At the same time, there is a lot of greenhouse gases such as carbon dioxide (CO₂) [2] produced by the burning of these fossil fuels and other human activities [3]. These greenhouse gases not only pollute the atmosphere but have also led to global warming. However, the limited availability of these fossil fuels and the long-term adverse effects on the environment resulting from their exploitation reflects the urgency to develop alternative solutions to effectively utilize other primary energy sources which are environmentally friendly. One of these clean sources is renewable energy [4].

Renewable energy sources such as solar (sun), wind, water, and biomass [5] just to mention a few have been reported as an alternatives to these fossil fuels [6]. Among these, solar energy is an unarguably endless energy source. Solar energy has brought attention to researchers where photovoltaic devices such as solar cells are used to convert photons to electricity through the photovoltaic effect. The first solar cell by Charles Fritts in 1883 that used selenium produced a low efficiency of 1% [7, 8]. Later, Bell laboratories in 1953 reported an improvement of efficiency to 6 % using silicon solar cells. Since then, a lot of research has been conducted on silicon solar cells which have reported an improvement of the efficiency from 6 to 24 % [9]. There are numerous efforts devoted to improving the power conversion efficiency (PCE) of solar cells [10]. Several types of solar cells which include silicon, perovskites, organic and plasmonic, have been reported. Figure 1.1 shows the Timeline of best research solar cell efficiencies adapted from the National Research Energy Laboratory [11]. The silicon-based solar cell is the commercialized one in the markets since it has a higher PCE. However, the associated limitations of silicon-based solar cells include high production cost, the heavyweight of the solar panels, and a complex fabrication process. This has led the researchers to explore organic solar cells as an alternative to these silicon-based solar cells [12].

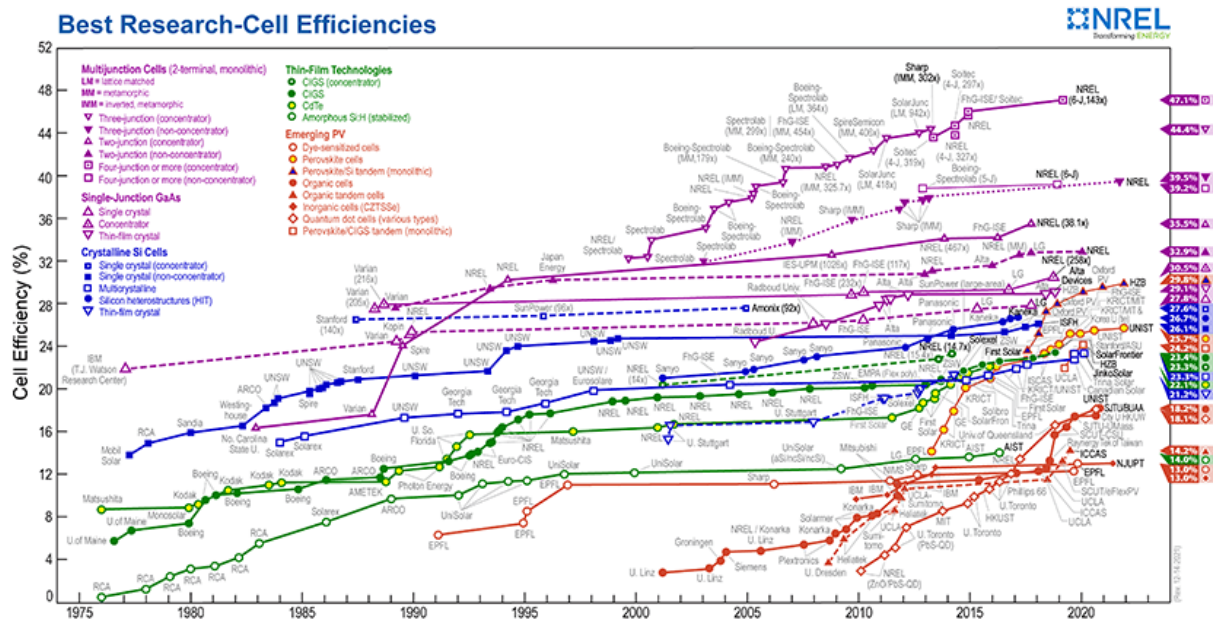


Figure 1.1: Timeline of best research solar cell efficiencies adapted from National Research Energy Laboratory

Organic solar cells (OSCs) mainly consist of conducting polymer or organic molecules that act as a photoactive layer [13]. In addition, different synthetic modifications can fine-tune OSCs for a full absorption visible region. The OSCs are easy to fabricate, cheap to produce, lightweight and flexible [13, 14]. With 17.7% PCE, there is still much to be studied about OSCs [15]. Increasing light trapping in OSCs is one of the parameters to improve their PCE.

There has been optimization of light trapping in recent thin films solar cells [16]. Different approaches in improving light trapping such as far-field scattering from subwavelength metallic nanoparticles (NPs) sustaining localized surface plasmon resonances (LSPR) has been identified by different researchers [16, 17]. They are known as plasmonic solar cells. The thickness of solar cells is very important to light absorption since a large thickness can lead to charge recombination in which the energy of the photon is lost [18]. Therefore, this method of incorporating plasmonic NPs in solar cells can help by trapping the light inside the solar cell without increasing the thickness [10].

Metal-polymer nanocomposites, which are metallic nanoparticles (NPs) embedded in a conducting polymer matrix [19], have received a lot of attention in the past two decades or so because of their tunable magnetic [20], mechanical [21], electrical [22], and optical properties

[23]. Due to their promising properties, they can be used in a wide range of applications, including sensors [24], light-emitting diodes [25], solar cells [26], and capacitors [27]. The characteristics of poly(3,4-ethylene dioxythiophene): poly(styrene sulfonate) (PEDOT: PSS) and their mix with gold (Au) and silver (Ag) nanoparticles have attracted interest in recent years among other metal-polymer nanocomposites. PEDOT: PSS is a conductive polymer with a good work function [28] and surface roughness [29] that is often employed as a buffer layer in OSCs between the anodic electrode [30, 31] and the organic photoactive layer [32].

Instead of embedding sub-wavelength-dimension plasmonic NPs into the photoactive layer [33, 34], researchers have discovered that incorporating the NPs into PEDOT: PSS sheets improves the visible spectrum absorption of the composite due to localized surface plasmon resonance (LSPR) [35-37]. In this situation, light scattering [32, 36] is increased in addition to absorption, which could be favourable for light trapping in the photoactive layer. It has also been observed that incorporating plasmonic NPs into PEDOT: PSS can improve the conductivity [38-40] of the material while simultaneously improving the surface roughness [26, 32]. Surface roughness reduces losses due to reflection and increases the scattering of incident light [41]. Hybrid Ag-PEDOT: PSS thin films have the potential in improving photovoltaic performance in OSCs [26, 32] since they have excellent optical [42], structural [43], and electrical properties [43].

In this study, colloidal Au, Ag and copper (Cu) NPs were synthesised and hybrid Au and Cu NP-PEDOT: PSS thin films were created. From visible to UV spectrum, Au, AgNPs display LSPR with a wider wavelength tunability window. Despite this appealing LSPR tunability, the integration of Au and AgNPs in PEDOT: PSS, as well as the characteristics that arise, has not yet been investigated. In this study, structural and optical characterizations of AuNPs, Ag NPs, PEDOT: PSS, and PCBM: P3HT thin films were studied using transmission electron microscopy (TEM), ultraviolet/visible spectroscopy, Raman spectroscopy, and X-ray diffraction measurements. The findings of various characterisation techniques to see how varying concentrations of Au, Ag and Cu NPs alter the optical and structural properties of PEDOT: PSS thin films, offering insights on their potential use in OSCs in the future was compared.

1.2 Aim and objectives

This dissertation aims to synthesize and fabricate the OSCs enhanced by plasmonic NPs

The objectives are:

- (a) To synthesize Au, Ag and Cu NPs using chemical reduction and study their morphology, structural, and optical properties
- (b) To study the changes in PEDOT: PSS due to incorporation of plasmonic NPs.
- (c) To fabricate the plasmonic organic solar cell using PC₆₁BM: P3HT as the active layer and investigate the electrical properties

1.3 Structure of the dissertation

This dissertation is divided into five chapters

Chapter 1 discusses the background and motivation as well as the aim and objectives of the study and the structure of the dissertation.

Chapter 2 discusses the literature review on different plasmonic NPs, their different properties and significance, synthesis, and applications as well as their use in OSCs.

Chapter 3 discusses the experimental techniques used in this study as well as the characterizations.

Chapter 4 discusses the results obtained in this study, which are observed from the characterisations.

Chapter 5 discusses the overview conclusion of the dissertation and recommendations about future work.

1.4 References

- [1] S. R. Paramati, U. Shahzad, and B. Doğan, "The role of environmental technology for energy demand and energy efficiency: Evidence from OECD countries," *Renewable and Sustainable Energy Reviews*, vol. 153, p. 111735, 2022.
- [2] W. Schlenker, W. M. Hanemann, and A. C. Fisher, "Determinants of Agricultural Output: Degree Days, Yields and Implications for Climate Change," 2004.
- [3] A. Koyamparambath, J. Santillán-Saldivar, B. McLellan, and G. Sonnemann, "Supply risk evolution of raw materials for batteries and fossil fuels for selected OECD countries (2000–2018)," *Resources Policy*, vol. 75, p. 102465, 2022.
- [4] P. Mukherjee *et al.*, "Bioreduction of AuCl₄⁻ ions by the fungus, *Verticillium* sp. and surface trapping of the gold nanoparticles formed," *Angewandte Chemie International Edition*, vol. 40, no. 19, pp. 3585-3588, 2001.
- [5] B. Bhushan, *Encyclopedia of nanotechnology* (no. 544.1). Springer Netherlands, 2012.
- [6] Q. Li *et al.*, "Exploring the relationship between renewable energy sources and economic growth. The case of SAARC countries," *Energies*, vol. 14, no. 3, p. 520, 2021.
- [7] J. Xu, J. Zhang, and K. Kuang, "Manufacturing Solar Cells: Assembly and Packaging," in *Conveyor Belt Furnace Thermal Processing*: Springer, 2018, pp. 35-41.
- [8] Z. Liu and H.-E. Wang, "Enhanced Short-Wavelength Absorption and Effective Exciton Dissociation in NC70BA-Based Ternary Polymer Solar Cells," *ACS Applied Energy Materials*, vol. 4, no. 8, pp. 8432-8441, 2021/08/23 2021.
- [9] H. Mehmood, H. Nasser, S. M. H. Zaidi, T. Tauqeer, and R. Turan, "Physical device simulation of dopant-free asymmetric silicon heterojunction solar cell featuring tungsten oxide as a hole-selective layer with ultrathin silicon oxide passivation layer," *Renewable Energy*, vol. 183, pp. 188-201, 2022.
- [10] J.-L. Wu *et al.*, "Surface plasmonic effects of metallic nanoparticles on the performance of polymer bulk heterojunction solar cells," *ACS nano*, vol. 5, no. 2, pp. 959-967, 2011.
- [11] P. Berger and M. Kim, "Polymer solar cells: P3HT: PCBM and beyond," *Journal of Renewable and Sustainable Energy*, vol. 10, no. 1, p. 013508, 2018.

- [12] R. Missingham, "Budget Review 2010–11," ed: Parliament of Australia Library. Canberra: Parliament of Australia ..., 2010.
- [13] L. Feng, M. Niu, Z. Wen, and X. Hao, "Recent Advances of Plasmonic Organic Solar Cells: Photophysical Investigations," *Polymers*, vol. 10, no. 2, p. 123, 2018.
- [14] M. Kaltenbrunner *et al.*, "Ultrathin and lightweight organic solar cells with high flexibility," *Nature Communications*, Article vol. 3, p. 770, 04/03/online 2012.
- [15] J. Gao *et al.*, "Over 17.7% efficiency ternary-blend organic solar cells with low energy-loss and good thickness-tolerance," *Chemical Engineering Journal*, vol. 428, p. 129276, 2022.
- [16] S. Morawiec, M. J. Mendes, F. Priolo, and I. Crupi, "Plasmonic nanostructures for light trapping in thin-film solar cells," *Materials Science in Semiconductor Processing*, vol. 92, pp. 10-18, 2019.
- [17] S. K. Ghosh, S. Nath, S. Kundu, K. Esumi, and T. Pal, "Solvent and Ligand Effects on the Localized Surface Plasmon Resonance (LSPR) of Gold Colloids," *The Journal of Physical Chemistry B*, vol. 108, no. 37, pp. 13963-13971, 2004/09/01 2004.
- [18] V. Jovanov, "Characterization and modeling of nanostructured silicon thin-film optoelectronic devices," Jacobs University Bremen, 2015.
- [19] Z. Cao, Z. Chen, and L. Escoubas, "Optical, structural, and electrical properties of PEDOT: PSS thin films doped with silver nanoprisms," *Optical Materials Express*, vol. 4, no. 12, pp. 2525-2534, 2014.
- [20] S. Li, M. Meng Lin, M. S. Toprak, D. K. Kim, and M. Muhammed, "Nanocomposites of polymer and inorganic nanoparticles for optical and magnetic applications," *Nano reviews*, vol. 1, no. 1, p. 5214, 2010.
- [21] O. M. Folarin, E. R. Sadiku, and A. Maity, "Polymer-noble metal nanocomposites," 2011.
- [22] G. Kickelbick, "Concepts for the incorporation of inorganic building blocks into organic polymers on a nanoscale," *Progress in polymer science*, vol. 28, no. 1, pp. 83-114, 2003.
- [23] P. J. Maake, A. S. Bolokang, C. J. Arendse, V. Vohra, E. I. Iwuoha, and D. E. Motaung, "Metal oxides and noble metals application in organic solar cells," *Solar Energy*, vol. 207, pp. 347-366, 2020/09/01/ 2020.
- [24] D. W. Hatchett and M. Josowicz, "Composites of intrinsically conducting polymers as sensing nanomaterials," *Chemical reviews*, vol. 108, no. 2, pp. 746-769, 2008.

- [25] B. C. Sih and M. O. Wolf, "Metal nanoparticle—conjugated polymer nanocomposites," *Chemical communications*, no. 27, pp. 3375-3384, 2005.
- [26] S. Woo, J. H. Jeong, H. K. Lyu, Y. S. Han, and Y. Kim, "In situ-prepared composite materials of PEDOT: PSS buffer layer-metal nanoparticles and their application to organic solar cells," *Nanoscale research letters*, vol. 7, no. 1, pp. 1-6, 2012.
- [27] S. Pothukuchi, Y. Li, and C. Wong, "Development of a novel polymer–metal nanocomposite obtained through the route of in situ reduction for integral capacitor application," *Journal of Applied Polymer Science*, vol. 93, no. 4, pp. 1531-1538, 2004.
- [28] Z. Hu, J. Zhang, Z. Hao, and Y. Zhao, "Influence of doped PEDOT: PSS on the performance of polymer solar cells," *Solar Energy Materials and Solar Cells*, vol. 95, no. 10, pp. 2763-2767, 2011.
- [29] A. Elschner, S. Kirchmeyer, W. Lovenich, U. Merker, and K. Reuter, *PEDOT: principles and applications of an intrinsically conductive polymer*. CRC press, 2010.
- [30] H. Frohne, S. E. Shaheen, C. J. Brabec, D. C. Müller, N. S. Sariciftci, and K. Meerholz, "Influence of the anodic work function on the performance of organic solar cells," *ChemPhysChem*, vol. 3, no. 9, pp. 795-799, 2002.
- [31] Z. Su, L. Wang, Y. Li, H. Zhao, B. Chu, and W. Li, "Ultraviolet-ozone-treated PEDOT: PSS as anode buffer layer for organic solar cells," *Nanoscale research letters*, vol. 7, no. 1, pp. 1-6, 2012.
- [32] S.-W. Baek, J. Noh, C.-H. Lee, B. Kim, M.-K. Seo, and J.-Y. Lee, "Plasmonic forward scattering effect in organic solar cells: a powerful optical engineering method," *Scientific reports*, vol. 3, no. 1, pp. 1-7, 2013.
- [33] D. Duche *et al.*, "Improving light absorption in organic solar cells by plasmonic contribution," *Solar Energy Materials and Solar Cells*, vol. 93, no. 8, pp. 1377-1382, 2009.
- [34] S. Vedraïne *et al.*, "Intrinsic absorption of plasmonic structures for organic solar cells," *Solar energy materials and solar cells*, vol. 95, pp. S57-S64, 2011.
- [35] M. A. Namboothiry, T. Zimmerman, F. M. Coldren, J. Liu, K. Kim, and D. L. Carroll, "Electrochromic properties of conducting polymer metal nanoparticles composites," *Synthetic metals*, vol. 157, no. 13-15, pp. 580-584, 2007.
- [36] H. Atwater and A. Polman, "Plasmonics for Improved Photovoltaic Devices," *Nature materials*, vol. 9, p. 865, 10/01 2010.

- [37] S. a. Pillai and M. Green, "Plasmonics for photovoltaic applications," *Solar Energy Materials and Solar Cells*, vol. 94, no. 9, pp. 1481-1486, 2010.
- [38] K. J. Moreno *et al.*, "Silver nanoparticles functionalized in situ with the conjugated polymer (PEDOT: PSS)," *Journal of nanoscience and nanotechnology*, vol. 9, no. 6, pp. 3987-3992, 2009.
- [39] R. G. Melendez *et al.*, "On the influence of silver nanoparticles size in the electrical conductivity of PEDOT: PSS," in *Materials Science Forum*, 2010, vol. 644, pp. 85-90: Trans Tech Publ.
- [40] N. Semaltianos, W. Perrie, S. Romani, R. Potter, G. Dearden, and K. Watkins, "Polymer-nanoparticle composites composed of PEDOT: PSS and nanoparticles of Ag synthesised by laser ablation," *Colloid and Polymer Science*, vol. 290, no. 3, pp. 213-220, 2012.
- [41] V. Jovanov *et al.*, "Influence of interface morphologies on amorphous silicon thin film solar cells prepared on randomly textured substrates," *Solar Energy Materials and Solar Cells*, vol. 112, pp. 182-189, 2013/05/01/ 2013.
- [42] H. S. Noh, E. H. Cho, H. M. Kim, Y. D. Han, and J. Joo, "Organic solar cells using plasmonics of Ag nanoprisms," *Organic Electronics*, vol. 14, no. 1, pp. 278-285, 2013/01/01/ 2013.
- [43] L. Lu, Z. Luo, T. Xu, and L. Yu, "Cooperative plasmonic effect of Ag and Au nanoparticles on enhancing performance of polymer solar cells," *Nano letters*, vol. 13, no. 1, pp. 59-64, 2013.

Chapter 2

Plasmonic nanoparticles

2.1 Introduction

Nanotechnology is the study of materials at their nanometre scale. The nanomaterials, nanoparticles, or nanostructures range from 1-100 nm in diameter. Nanoparticles of different materials, sizes, and shapes have been synthesized by various methods depending on the availability, cost, and other factors [1]. Nanoparticles of different materials have attracted much attention from different parts of the world. Different fields of research in biology, medicine, chemistry, physics, material science, engineering, etc., have been applying nanoparticles to improve their enhanced scientific results [3].

2.2 Metal nanoparticles: Properties and their significance

Nanoparticles are a collection of bonded atoms or molecules to a size ranging from 1-100 nm [4, 5]. Syntheses vary from breaking up large materials to smaller ones or the grouping of atoms and molecules to nanosized structures. Their size, shape, and composition determine the behaviour in a research field. Due to their size, the surface area of nanoparticles is much higher than their volume, making their functional properties, including electronic, magnetic, optical and piezoelectric, different compared to the bigger structures [6]. The increase in surface area to an even higher magnitude changed the behaviour of the outer atoms of the nanoparticles [7]. This factor played a major role in nanoparticles, one of which was the simplicity to interact with solutions or substances in a reaction. The nanoparticles induce surface plasmonic resonance (SPR) as they interact with light [8], which is the oscillation of electrons at their surface [9]. SPR occurs when the wavelength of the incident light matches one of the nanoparticles. The shape of nanoparticles also had different major effects on their physico-chemical properties [10].

2.2.1 Noble metal nanoparticles

Research in recent years has reported noble metals, semiconductors, ceramics, fullerenes, polymeric-, carbon-based, and lipid-based nanoparticles among others [11]. Noble metal nanoparticles including gold, silver and platinum have notably are very interesting because of their unique properties [12], which include resistance to corrosion and oxidation, non-reactiveness, higher reduction potential, high melting point and high ionization energy. These properties have brought interest in exploring the functions and applications of noble metal nanoparticles. Furthermore, the properties of noble metals were determined by parameters

such as size, shape, architecture, crystallinity and composition. A wide range of noble metal nanoparticles has been applied in research fields such as biomedical and pharmaceuticals, drug delivery, gas-sensing, solar energy, water purification etc [13-17]. Nanoparticles were further applied in commercialised products such as cosmetics, toothpaste, shampoo etc [18, 19].

2.3 Synthesis of noble metal nanoparticles

In recent years synthesis of noble metal nanoparticles have received high attention because of their increasing applications. The world of nanotechnology research had been trying to develop and improve simple, safe, affordable and reliable ways to synthesize nanoparticles. These synthetic methods are increasing and classified into different categories. Generally, the categories for synthetic methods are “top-down” and “bottom-up” approaches. The top-down approach started with a material which was then broken down into smaller components of nano-sized particles whereas the bottom-up atoms or molecules were brought together to form nanoparticles. The top-down method manufactures a large number of nanoparticles whereas bottom-up resulted in homogeneous nanoparticles. Depending on the synthesis approach, these methods were further categorized as physical, chemical and biological. Different types of nanoparticles such as nanospheres, nanowires, nanoplates, nanotubes, nanoflowers, nanocages and others have been synthesized by the above methods in the past years and some other types may be found [16, 20, 21].

2.3.1 Top-down Approaches

The process generally involves cutting tools, milling and moulding the bulk materials to smaller particles with desired size and effect. Below are some examples of the top-down approach for the synthesis of nanoparticles.

2.3.1.1 Micropatterning

Micropatterning is a method of synthesis that is mostly used in electronics, cellular biology and biomedical engineering. Micropatterning includes a wide range of techniques which include scanning lithography, electron-beam (E-beam) lithography, soft lithography, nano contact printing, nano-imprint lithography, nanosphere lithography, colloidal lithography, scanning probe lithography etc. Among these techniques, the most used was photolithography. All these methods commonly used electromagnetic radiation of light in the ultraviolet or X-ray, electrons and ions. Material of interest was irradiated by an electron

beam in which separation of nanosized particles was achieved. Figure 2.1 shows micropatterning of silver nanoparticles done on plastic substrates [22].

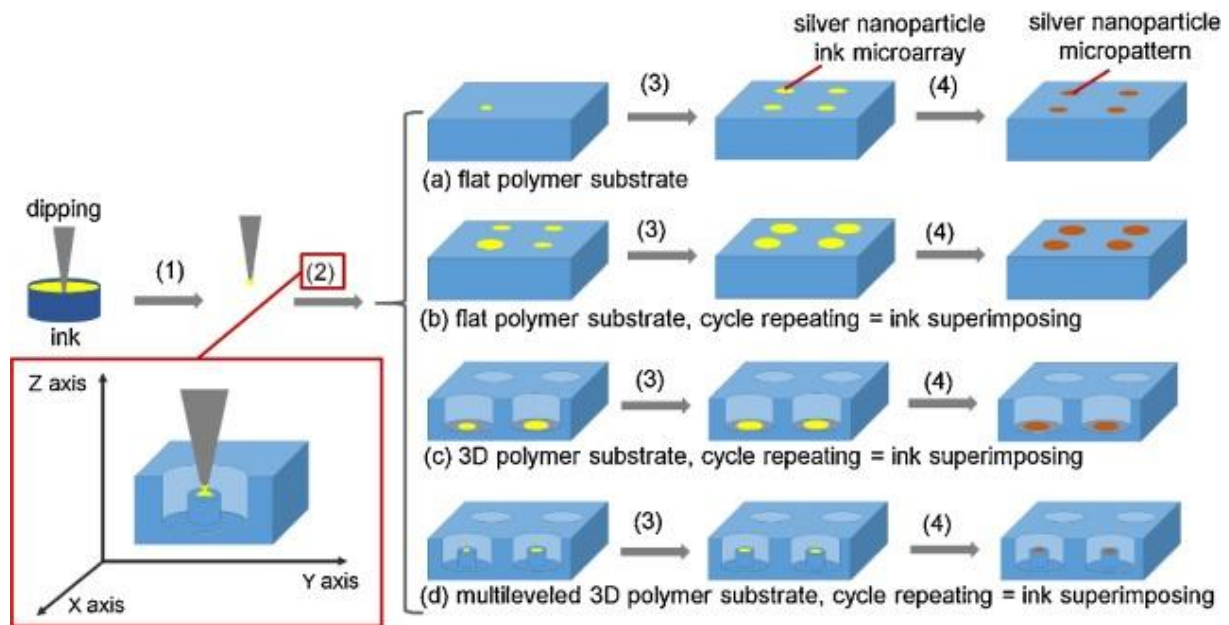


Figure 2.1: Schematic illustration of micropatterning of metallic nanoparticles using different polymer substrates [22].

2.3.1.2 Pyrolysis

Pyrolysis is used on a vapour (liquid or gas) which will then be turned into powder (solid) [23]. This process was achieved by forcibly pushing the vapour through an orifice at high pressure. The remains are burned and processed to obtain nanoparticles. Most of the time this method resulted in aggregates and agglomerates. Even though pyrolysis is one of the simple, frequently used powder production methods of synthesizing noble nanoparticles, it took high pressure and temperature which in turn required a lot of energy.

2.3.1.3 Attrition

Attrition, also regarded as “milling”, is a method of grinding bigger materials into nanoparticles. These materials are ground into a ball-milled to powder. The process had also been used in ceramic processing and powder metallurgy industries for a long time. This process depended on the energy distribution between the grinding devices. Kinetic energy had been transferred from balls to powder when reducing the grain size. Size, shape and physical properties depend on the type of mill, milling atmosphere, milling media, the intensity of milling, ball to powder weight ratio, milling time, and milling temperature. Researchers tried to counteract these parameters by the development of grinding devices for a

variety of criteria such as tumbler mills, attrition mills, shaker mills, vibratory mills, planetary mills etc. Such devices were comparable when it comes to their capacity, milling efficiency etc.

The effect of attrition came when one was producing nanoparticles in huge amounts. Also, the process had been used to produce alloy and nanocomposites. Since attrition is about grinding, this brought disadvantages such as damaged crystals and structure. This was due to the strain which the material endured during the grinding process. The damage affects the physico-chemical properties of the nanoparticles. In addition to the above problems was the contamination which came from around the environment including the atmosphere, milling tools and other surface and interface contaminations. Piras et al. have used a milling process to produce cellulose nanoparticles with the procedure as shown in Figure 2.2 [24].

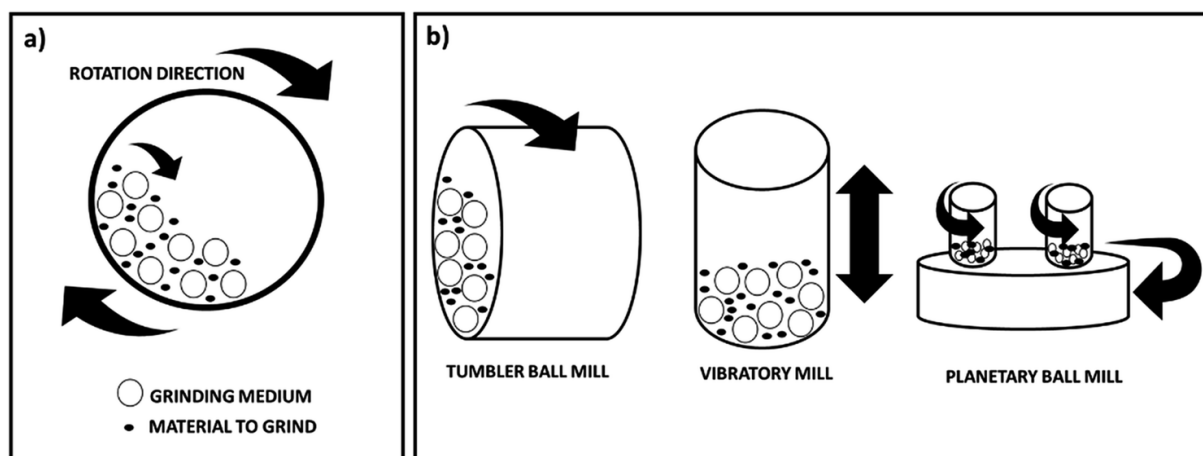


Figure 2.2: Schematic illustration of using attrition method for synthesizing metal nanoparticles [24].

2.3.2 Bottom-up Approaches

Bottom-up approaches build up nanoparticles from their basic atomic or molecular structures by assembling them using chemical properties. Different bands were recognised in this type of approach. The big advantage of the bottom-up approach is the fact that nanoparticles are stable, homogeneous, perfectly crystallographic and surface structure. This in turn brought along good news in applications. The bottom-up approach has a variety of synthetic methods which were used commonly to develop nanoparticles.

2.3.2.1 Chemical reduction method

The most common method for synthesizing noble metal nanoparticles is chemical reduction. The nanoparticles are prepared inside a solution. Generally, a precursor salt is reduced by a chemical reducing agent while the capping agent is present. Reducing agents such as hydrogen, hydrazine, alcohols, carbon monoxide, LiAlH_4 , NaBH_4 , or $\text{R}_4\text{N}^+(\text{Et}_3\text{BH}^-)$ and a capping agent such as trisodium citrate ($\text{Na}_3\text{C}_6\text{H}_5\text{O}_7$) are used to obtain metal nanoparticles.

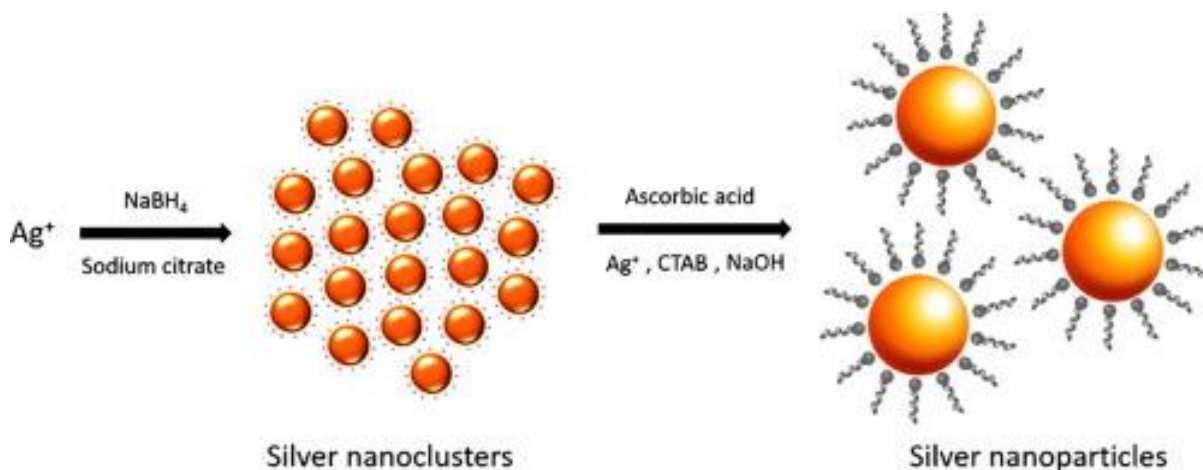


Figure 2.3: Schematic illustration for chemical reduction of Ag^+ to silver nanoparticles [25].

The Lee-Meisel and Creighton methods are the most widely used chemical reduction methods for producing noble metal nanoparticles. The Lee-Meisel method had been used to produce silver nanoparticles from silver nitrate and sulphate precursors. The precursor salts were reduced by NaBH_4 , sodium citrate and H_2 at varying temperatures. Based on the parameters such as concentration and temperature, this method produced silver nanoparticles with different sizes and morphology. A seed-mediated growth of Ag NPs was performed by Rostami *et al.* for detection of ascorbic acid in vitamin C tablets [25]. The varying pH of the reaction also resulted in control of the sizes and morphology of these nanoparticles. High pH reduced silver nitrate faster resulting in nanospheres and nanorods. Then lower pH resulted in the slower reduction of silver nitrate which produced triangle and polygon-shaped silver nanoparticles.

The Turkewich method is commonly used as the method of synthesizing gold nanoparticles. The method reduces chloroauric acid (HAuCl_4) precursor with NaBH_4 in the presence of trisodium citrate as the stabilizing agent. Also, the concentration of the reagents controls the size of nanoparticles. In this method, however, nanospheres are produced and sometimes ellipsoidal shapes. Polyethylene glycol-g-polyvinyl alcohol (PEG-g-PVA) can be used as a

reducing, stabilizing and capping agent when synthesizing gold nanoparticles. Platinum nanoparticles have also been synthesized using chemical reduction. Zhang *et al.* have reduced platinum acetylacetonate with varying concentrations of sodium polyacrylate as a stabilizing agent to produce platinum nanocubes [26]. The method of producing platinum was selective to cubic shapes. Chemical reduction is a highly appreciated method of synthesizing nanoparticles because it is very convenient. However, chemical reduction also has some drawbacks. The reaction takes a long time and requires a high temperature to be completed. Variation of shape is difficult when synthesizing noble metal nanoparticles. The major disadvantage is the toxic reagents used. Precautions need to be applied when handling and disposing of reagents as they can result in health and environmental risks. For example, NaBH_4 which is used as a reducing agent is flammable, can cause residual injuries if exposed to humans and reacts violently with water at high temperatures. These disadvantages mean that nanoparticles produced by chemical reduction cannot be used for biomedical health treatment such as cancer.

2.3.2.2 Microemulsion method

The microemulsion method uses a dispersion containing water, oil and surfactant which is applied on the reagents. These reagents are dispersed separately in two emulsions and mixed at the end. Nucleation follows to form nanoparticles. The microemulsion method existed in the early 1980s in which platinum, palladium and rhodium nanoparticles were synthesized. The microemulsions usually used are oil-in-water and water-in-oil. During the oil-in-water process, *normal micelles* form when hydrophilic head groups of surfactant molecules move out of micelles with their hydrophobic tails pointing into the direction of the core whereas the opposite occurs during the water-in-oil process in which *reverse micelles* are formed shown in Figure 2.4 [27]. The method has control over properties such as size, morphology, and homogeneity. However, this method requires high concentrations of surfactants.

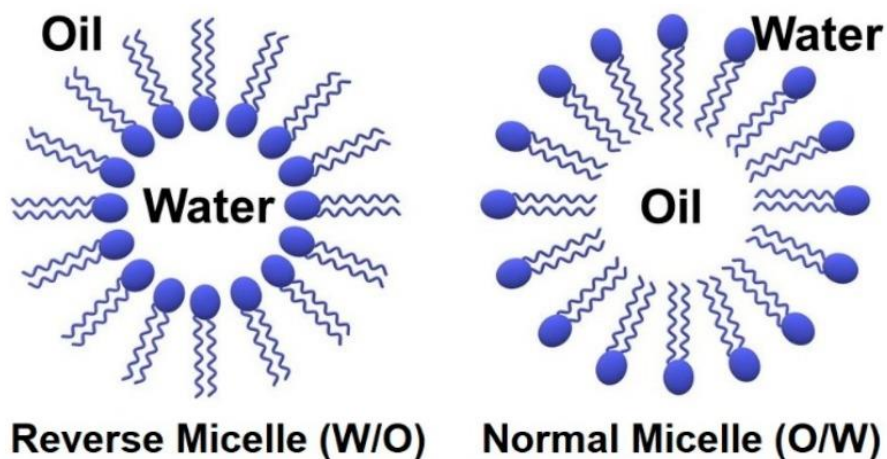


Figure 2.4: Schematic diagram of microemulsion method of synthesizing metal nanoparticles [27].

2.3.2.3 Electrochemical method

The electrochemical method of producing metal nanoparticles has evolved in the last decade. The process made use of cathode and anode. The metal sheet was dissolved at the anode and the metal nanoparticles were formed at the cathode by reduction of the intermediate metal salt.

2.3.2.4 Laser ablation

Laser ablation made use of a laser beam to remove particles from a metal surface. The material heated by the laser at a low flux containing energy was absorbed and get evaporated or sublimated. The material was converted into plasma at high laser flux. Producing nanoparticles of the desired amount can be controlled by the wavelength of the laser and the optical properties of the material. The metal nanoparticles can be synthesized in aqueous and organic solvents without the necessity of toxic reagents. Figure 2.5 shows the method used by Xu *et al.* in the synthesis of Au NPs by laser ablation in liquid in which they were applied in electrochemical detection of heavy metal ions [28].

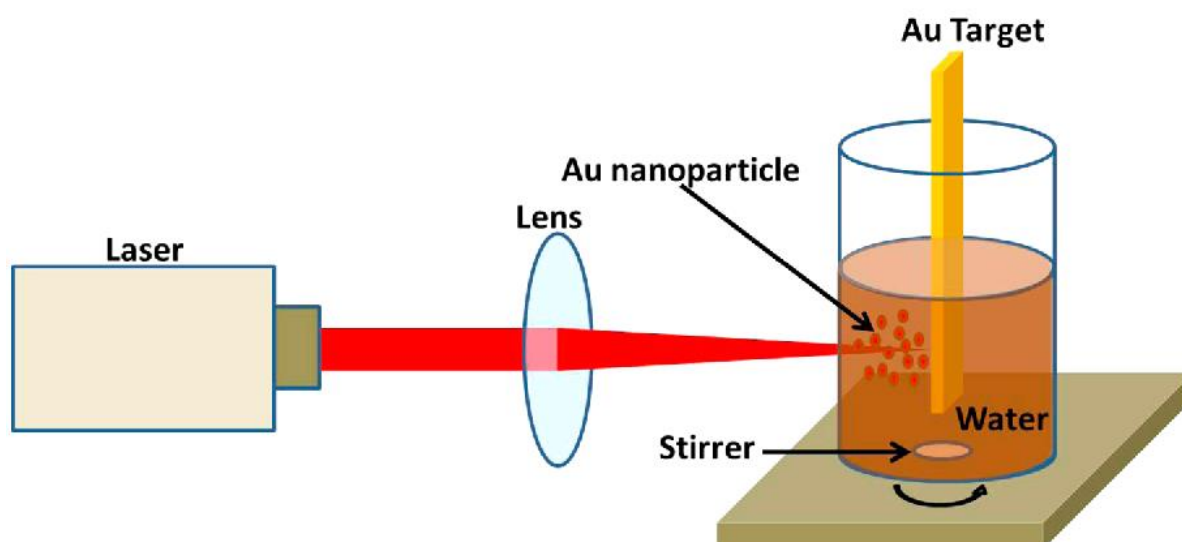


Figure 2.5: Schematic diagram for the synthesis of gold nanoparticles using laser ablation [28].

The development of laser ablation in recent years sees the technique to be an alternative method for chemical reduction in the synthesis of noble metal nanoparticles. Laser ablation has been employed by Mafune *et al.* to synthesize stable nanoparticles [29-31]. The metal plate was immersed in a surfactant-containing solution that pockets the nanoparticles to inhibit contact. Laser ablation is a fast, simple and powerful method which had been used to produce a large number of nanoparticles. Jimenez *et al.* also used the method on a solid dipped in an aqueous solution containing metal salts to be reduced to nanoparticles [32]. Laser ablation enables control over the size, morphology, and composition of nanoparticles.

2.3.2.5 Microwave method

Microwave radiations have been used in the research world for various synthetic procedures. Synthesis of metal nanoparticles using microwave involves reduction of metal salts in polymer surfactants solution. This method has successfully been utilized for the preparation of Au, Ag and Pt nanoparticles. One of the main advantages of the microwave method is the ability to control size, shape, and morphology. This can be done by variation of reaction parameters.

2.3.2.6 Green synthesis methods

Unlike other conventional methods such as chemical reduction which require harmful chemicals and high energy, the green synthesis technique make use of green chemistry.

Green synthesis is an environmentally friendly way of synthesizing metal nanoparticles since it employs a mild solvent system, non-toxic and environmentally friendly stabilizing agents.

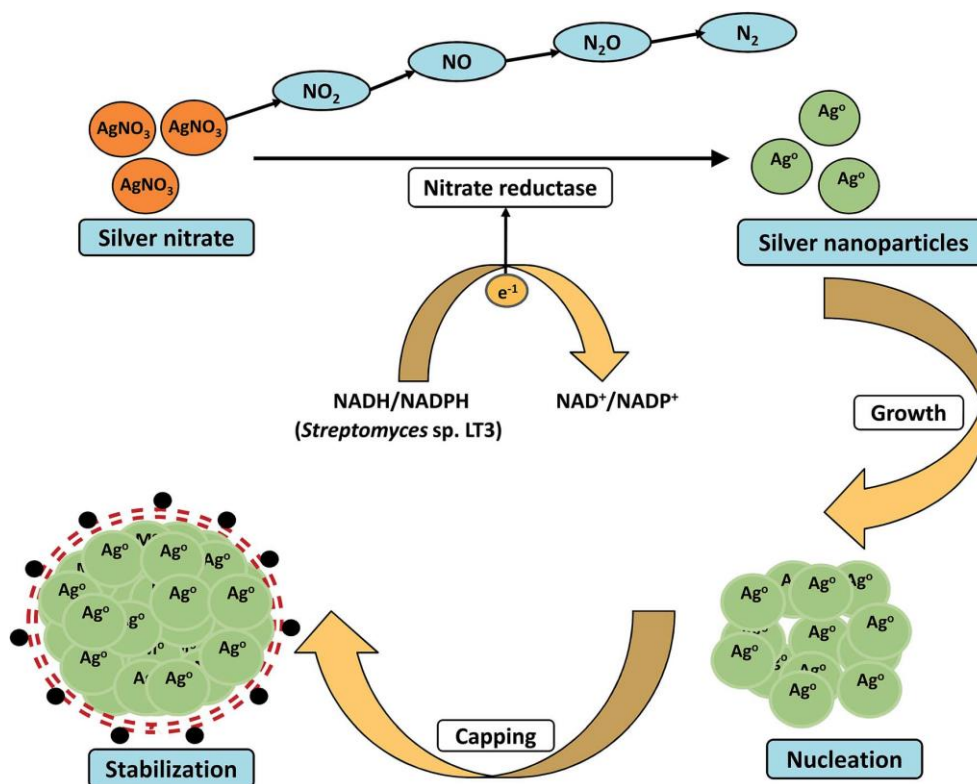


Figure 2.6: Schematic illustration for using nitrate reductase as a reducing agent during synthesis of silver nanoparticles [33]

The use of green synthesis involves imitation of nature's synthesis of nanomaterials. Biomolecules have been used as templates for synthesizing material. These biomolecules such as proteins, carbohydrates, lipids, and their building blocks, can be used as stabilizing agents for the synthesis of nanoparticles. The use of biomolecules has been used for nanoparticles synthesis in the last decade and has been developed thoroughly.

2.3.2.7 Biological methods

Methods of synthesizing metal nanoparticles vary by needed appliances, elements, etc., however, a lot are costly and non-environmentally friendly (because of toxic and hazardous chemicals). With the need to avoid above mentioned setbacks, the development of biological methods for the synthesis of metal nanoparticles were brought into the picture. Microorganisms have the ability to interact with atoms and molecules of different kinds. This potential has been taken advantage of to produce nanoparticles.

With different types of microorganisms abroad (with various properties), each one uniquely interacts with metals. The microbes are divided into two groups, unicellular prokaryotic organisms include bacteria and eukaryotic organisms which are multicellular include algae, fungi and plants. Control and variation of reaction conditions such as incubation period, concentration, pH and ratio of metal salt to metabolite etc., give a great advantage to manipulate yield and stability of nanoparticles. Below are some of the microorganisms used in the production of noble metal nanoparticles.

(a) Synthesis of nanoparticles by Prokaryotes

Prokaryotes are unicellular organisms that do not contain a nucleus, mitochondria, or any other organelle. Prokaryotes are chosen due to their characterisations which include simplicity to their structures and metabolisms. Microorganisms such as prokaryote have the ability to adapt and overcome extreme and harsh conditions when exposed to stressful metal-rich parameters. This is due to their resistance mechanisms such as suppression of influx, enhanced efflux mechanisms, extracellular complexation, intracellular chelation or precipitation and enzyme detoxification of metals.

Various nanoparticles have been synthesized by various prokaryotic microorganisms in the past years. Magnetite, siliceous material and gypsum nanoparticles have been reported. Magnetotactic bacteria are employed to synthesize magnetic nanocrystals such as Fe_3O_4 or Fe_3S_4 with sizes ranging from 35-120nm using magnetosomes. Cadmium sulphide (CdS) nanoparticles can be synthesized using both *Klebsiella aerogenes* and *Schizosaccharomyces pombe* by the mineralization process.

An earlier study by Klaus et al. reported the synthesis of intracellular nanocrystals for metallic Ag and monoclinic Ag_2S compositions of spherical, truncated triangular and irregular shapes by using *Pseudomonas stutzeri* (AG259), which is regarded as metal accumulating bacterium [34]. Shahverdi et al. employed *Klebsiella pneumoniae*, *Escherichia coli* and *Enterobacter cloacae* which are members of Enterobacteriaceae, to synthesize silver nanoparticles [35]. Silver nanocrystals were also synthesized by *Bacillus licheniformis* from the precursor of silver nitrate.

Gold nanoparticles have also been synthesized by bacterial methods. *Bacillus subtilis* have been employed by Southam and Beveridge to accumulate and reduce Au^{3+} . Nanotriangles/prisms were formed by organic sulphur and phosphate. A photosynthetic

bacterium called *Rhodopseudomonas capsulate* was used to synthesize gold nanoparticles by He et al. *Bacillus licheniformis* have previously been reported in the synthesis of silver nanoparticles, however, it can also be used for extracellular synthesis of stable gold nanocubes [36]. Intracellular synthesis of gold nanoparticles, done by reducing Au^{3+} using anaerobic bacterium *Shewanella algae* have also been reported. *Stenotrophomonas maltophilia* has been employed to synthesize gold nanoparticles from soil samples that come from gold mines. The spherical shapes have been reduced from Au^{3+} to Au^0 by NADPH-dependant enzyme. The nucleation and synthesis of gold, silver and gold-silver alloy crystallites have been successfully done by using *Lactobacillus* which is from the buttermilk.

Platinum nanoparticles synthesis by prokaryotes has few reports as compared to silver and gold nanoparticles. Bacterium *Schewanella*, which is used for the synthesis of gold nanoparticles, can also be used for the bioreduction and deposition of platinum nanoparticles. Bioreduction of hexachloroplatinic acid by *Acinetobacter calcoaceticus* leads to platinum nanoparticles.

(b) Synthesis of nanoparticles by Eukaryotes

With the synthesis of nanoparticles by using bacteria, researchers developed an interest in biological methods. The bacterial methods may have advantages over many methods however, it has various disadvantages such as handling and low synthesis efficiency. The use of multicellular eukaryotic organisms has risen to be a potential candidate in nanoparticles synthesis since they have an advantage over other methods such as easy to handle, low maintenance cost and easy downstream processing.

i. Synthesis of nanoparticles by fungi

One of the eukaryotic organisms (fungi) has demonstrated the ability to interact with metal and metal oxide to produce their respective nanoparticles. Sastry et al. have demonstrated *Verticillium* species' ability to produce gold nanoparticles both at its surface and within its cytoplasmic membrane by reducing AuCl_4 [37]. *Fusarium oxysporum* has been used for the extracellular synthesis of gold and silver nanoparticles which were highly stable. Fungi have also reduced other metals to create Pt, Zr, Si, Ti and metal carbonate nanoparticles. Figure 2.7 shows the procedure of reducing AgNO_3 to Ag by using fungi [38].

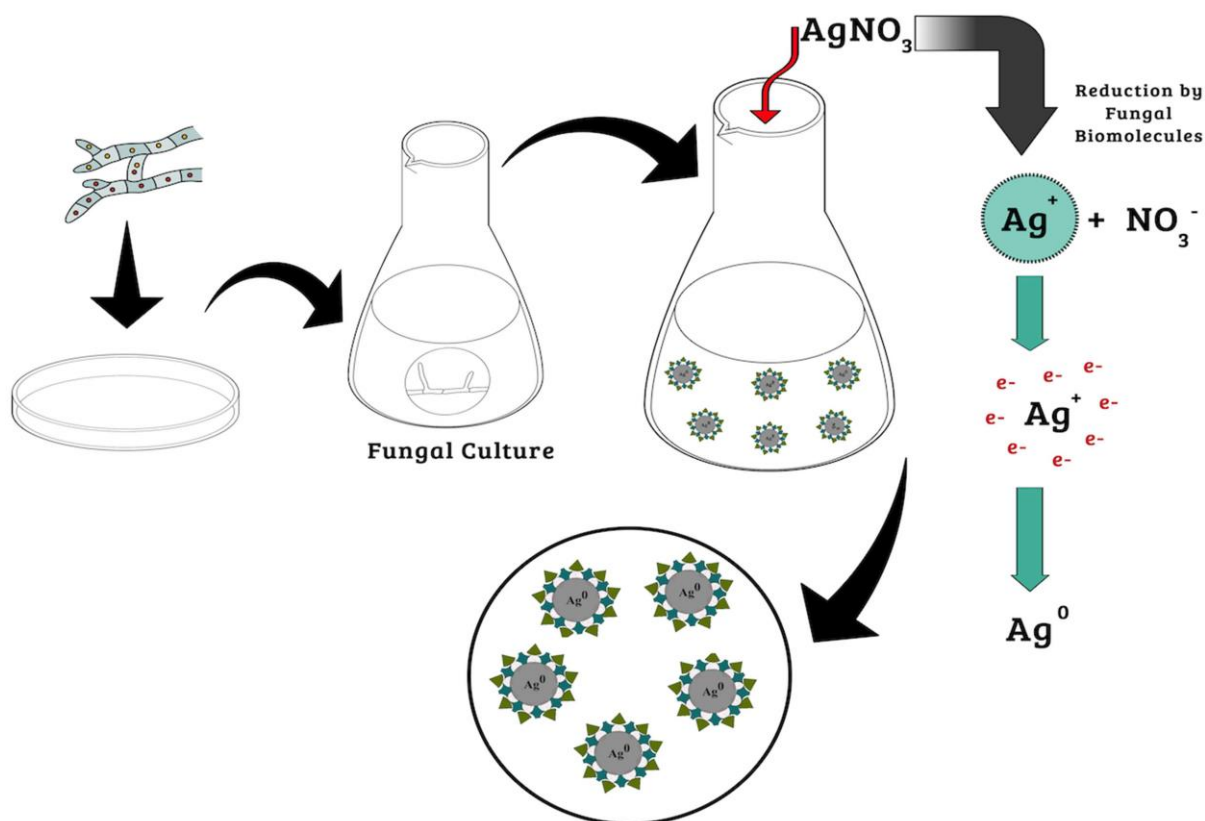


Figure 2.7: Reduction of AgNO_3 to silver nanoparticles by fungi [38].

The intra- and extracellular synthesis of platinum nanoparticles have been reported by Riddin et al in which they produced sizes of 10–100 nm with hexagons, pentagons, circles, square and rectangle shapes [39]. Variation of pH, temperature and salt concentration has been taken into consideration. The reduction of platinum ions to platinum nanoparticles has been studied by applying a fungal hydrogenate enzyme. The study involved mycosynthesis of platinum nanoparticles for further understanding.

Aspergillus flavus has been used as an environmentally friendly and cost-effective method to successfully synthesize silver nanoparticles using cell-free filtrate. This study also involved mycosynthesis in which the extracellular protein profile was analysed for understanding. The synthesis involved 32 and 35kDa proteins in which the silver nanoparticles were stabilized.

ii. Synthesis of nanoparticles by algae

Algae have the potential to synthesize metal nanoparticles by extraction. An extract of *Chlorella vulgaris* has been employed by Xie et al. to synthesize silver nanoparticles at room temperature [40]. The process was done by involving Tyr and Asp/Glu residues from hydroxyl and carboxyl groups respectively, which were then followed by anisotropic growth

of silver nanoparticles. Sinha et al. used *Pithophora oedogonia*, a freshwater green alga for the synthesis of silver nanoparticles [41].

Gold nanoparticles were also reported under synthesis by algal extracts. Marine alga called seaweed was used in the production of gold nanoparticles by Singaravelu et al. by applying elaborate screening [42]. Gold nanoparticles of sizes between 8-12 nm with high stability were discovered when *Sargassum wightii* were used. Another marine alga known as *Ecklonia cava* has been used to rapidly reduce chloroauric acid to gold nanoparticles. The process finished within a minute at 80 °C to completely form nanoparticles. The stability of nanoparticles produced by algae is very high inside a solution which gives the process advantage.

iii. Synthesis of nanoparticles by plants

The use of photosynthesis from plants for the production of nanoparticles has been seen as a true green synthesis. The approach uses plant extract from parts of the trees such as leaves, flowers, fruit, bark, gum, peel etc. with various plants to choose from. Gardea-Torresdey et al. have synthesized gold nanoparticles by using live alfalfa plant by reducing Au³⁺ ions to Au⁰ from solid media [43]. Plant secretome was used as a reducing agent where absorption, nucleation and growth of gold nanoparticles followed.

Shankar et al. have reported the usage of neem leaf extract for the synthesis of stable silver, gold and bimetal Au/Ag nanoparticles [44]. Terpenoids found in neem were used in the reduction of metal ions for the formation of bimetal nanoparticles. The resulting silver nanoparticles were dominated by spherical shapes with ranges of 5-35 nm in diameter. Neem leaf (moth) also produced a capping agent which was wrapped around the nanoparticles. Gold nanoparticles resulted in planar shapes. Bimetal nanoparticles of Au/Ag ranged between 50-100 nm. Shah et al. made use of the aqueous extract of *Ferocactus echidne* (which is regarded to be beneficial to medicine), to synthesize silver nanoparticles [45]. The plant naturally has polyphenols and ascorbic acid, which are believed to be reducing agents for silver nitrate to silver nanoparticles. Ankamwar et al. employed a tamarind leaf extract for rapid reduction of AuCl₄ in their synthesis of single-crystalline gold nano triangles [46]. Shankar et al. have reported a rapid reduction for extracellular synthesis of gold nanoparticles using both geranium leaves (*Pelargonium graveolens*) and its endophytic fungus (*Colletotrichum* sp.) [44]. By only using fungus, the reaction was not rapid. Gold nanoparticles were also synthesized by using coriander leaf extract.

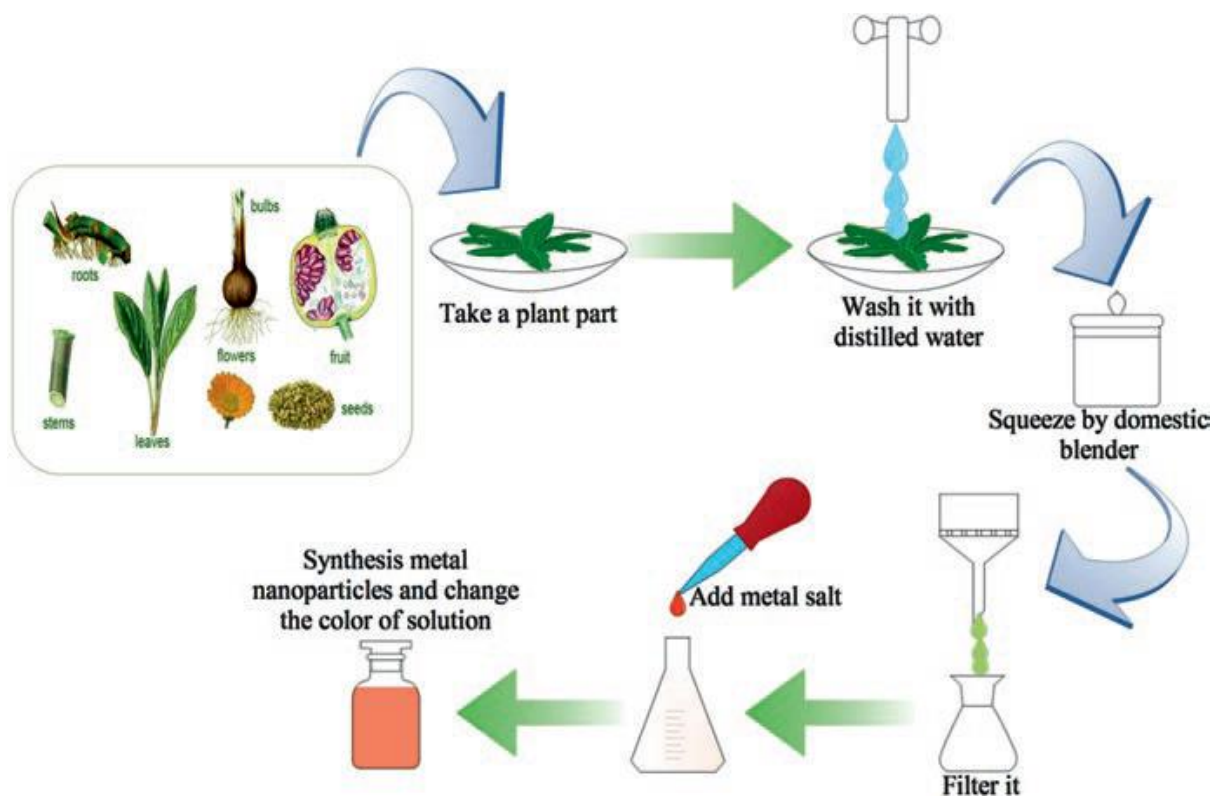


Figure 2.8: Synthesis of metallic nanoparticles by using plant extract [47].

Apart from using plant extract from boiling plant leaves as in previous methods, other forms such as bioreduction can be used. Huang et al. used sundried biomass of *Cinnamomum camphora* leaf in the synthesis of silver and gold nanoparticles [48]. The advantages of this sundried leaf gave the motivation for the synthesis over boiled leaf extract. With control over size and shape being the centre of nanoparticles production, it was proposed that adjusting parameters such as the amount of plant biomass dried during the reaction can be made. The reaction occurs in such a way that metal ions are reduced by polyols whereas nanoparticles are stabilized by water-soluble heterocyclic compounds.

Paul et al. synthesized gold nanoparticles with the shell extract of green coconut (*Cocos nucifera* Linn) at room temperature. Na_2PtCl_4 has been reduced by *Cacumen platycladi* extract to produce platinum nanoparticles [49].

With the above-mentioned methods physical, chemical and biological synthesis of noble metal nanoparticles, it is noted that there are also a variety of advantages and disadvantages depending on each type. The need for more environmentally friendly, cost-effective, scalable with properties controllable is still growing. The above methods should be chosen looking at the required applications which also vary according to properties.

2.4 Characterization of nanoparticles

Since nanoparticles are synthesized for different purposes, this brings the need for characterising them. It is a very important step to see the success of the synthesis of metal nanoparticles. Their interaction with light at the nanometre level makes this procedure to co-work with characterisations. Different characterisation techniques have been used to investigate various properties of synthesized nanoparticles. Depending on the phase (usually liquid or solid) of the medium containing nanoparticles, different characterisation instruments are available to accommodate them.

Scanning and transmission electron microscopies (SEM and TEM) are used for examining the size, shape and morphology of metal nanoparticles synthesized. Ultraviolet/visible (UV/Vis) spectroscopy determines the wavelength in which nanoparticles absorb light. X-ray diffraction (XRD) determine the phases present in nanoparticles which will help with crystal structure and crystallite size. The elemental composition of nanoparticles is characterised by Energy dispersive X-ray analysis (EDX). Atomic force microscopy (AFM) is used to measure the surface topography of nanoparticles.

2.5 Applications of noble metal nanoparticles

Noble metal nanoparticles have been developed in recent years with their growing applications in fields such as electronics, information technology, energy, catalysis, automobile, defence and security, cosmetics, biosensor, food and packaging, ecology, environment, and agriculture because of their unique properties.

2.5.1 Gold nanoparticles

As a precious metal, gold has already been regarded as a commercial product associated with royalty in previous years. Gold has already been applied to a lot of industries from ancient times. Gold nanoparticles are on top of the pyramid in applications as compared to other nanoparticles. Gold has unique properties at the nanometer level which can be controlled and applied in different fields. More world problems can be solved by using gold nanoparticles as their improvement. For problems such as catalysis and cancer treatment, gold nanoparticles have been in the centre. Along with drug delivery and diagnosis to treatment which includes tumour-targeting technologies. They can also be applied to bio-sensing for detecting cancer cells at an early stage. Other applications include products commercialised in supermarkets.

2.5.1.1 Labelling and visualization

Gold nanoparticles have been applied in many different types of visualization and bio-imaging techniques. These techniques are used to check and observe present chemical and physical properties and to identify different infectants. For this reason, gold nanoparticles are focused on the observation and visualization region for providing contrast. With colloidal gold of spherical shapes applied in microscopic studies as labels, there are also shapes such as labelling nanorods, nanoshells, nano-cages, nanostars, and other types of particles that have been applied in labelling and visualization in recent years. Gold interaction with light at the nano scale is seen as one of the most uncomplicated detection techniques. Gold nanoparticles induce a phenomenon known as SPR when light is absorbed and scattered.

Immunostaining, which was first described by Albert Coons in 1941, is a technique used for detecting molecules or parts of molecules such as antigens by using antibodies. Gold nanoparticles have found an interest in immunostaining as an application. The molecules or cell compartments present in a cell need to be in contrast with the other structures of the cell. The interaction between biomolecules and nanoparticles behaves similar to interactions between amino acids and side chains and the metal atoms in coupling biomolecular systems and generate novel materials. Gold nanoparticles incorporated in proteins/enzymes, antigens/antibodies, and DNA/oligonucleotides can be applied to different systems such as affinity separations, bio-sensing, bioreactors, and the construction of biofuel cells. In order for gold nanoparticles to be applied in detecting cancer cells, they can be bound to the cancer cell membrane for modification. This can give a signal resulting from the interaction between the cell membrane and aggregation of gold nanoparticles which will differentiate cancer cells from normal cells of the body.

2.5.1.2 Diagnostics

Recent features of clinical diagnostics have frequently been using gold nanoparticles fused along with receptors. Gold nanoparticles which have also been employed to detect antigens and for immunostaining has provided various advantages in bio-diagnostics.

Biomolecules such as proteins, which were also described previously for synthesizing metal nanoparticles, can be merged with gold nanoparticles by using different methods such as electrostatic interactions, covalent bonding using linker molecules, etc. This occurs when the surface density of adsorbed protein is increased by strong interaction between the surface of

nanoparticles and proteins. The orientation of protein molecules will significantly be given by the size of the nanoparticles.

The merging of antigen and antibodies with gold nanoparticles have been a great help with developing various immunological detection methods. Tests of nanoparticles of different proteins and DNA were developed with various methods. Based on the absorption spectrum where the redshift of gold nanoparticles is observed, these methods can detect the interaction between nanoparticles and biomolecules. The information can also be used for development in detecting various antigens human chorionic gonadotropin, cancer cells, *Leptospira* cells in urine as well as estimation of immunoglobulins, thrombin, glucose, protease activity and other purposes. Nossier et al. have detected the presence of hyaluronidase in urine by using gold nanoparticles (coated with CTAB) interaction with hyaluronic acid [50]. The process involved breaking down hyaluronic acid into small particles using hyaluronidase, this, in turn, prevent aggregation of gold nanoparticles showing enzyme in urine. Gehrman et al have coated gold nanoparticles with cmHsp70.1 monoclonal antibody to enable detection of Hsp70-positive tumours [51]. Apart from existing clinical diagnosis methods which involves immunoassays of gold nanoparticles, various applications such as immune chromatographic test strips on gold nanoparticles have been found. These are done by enhancing the signal of enzymes used in both primary and secondary antibodies by gold nanoparticles. Instead of nanospheres, irregular-shaped gold nanoparticles are used in chemiluminescent analysis of antibodies such as anti-IgG for determining the presence of IgG content in human plasma.

2.5.1.3 Therapeutic applications

(a) Photothermal therapy

The absorption peak of gold nanoparticles is in the visible region which makes photothermal therapy depends on the fact that their radiation will become hot in that region. Thermal cancer therapy has been under development with the use of laser radiations to allow modification and control in the treatment of targeted tumour tissues. Photothermal damaging of cells has shown significant purpose in various infections including cancer cells. Biodegradable liposomes gold nanoparticles recently employed by Rengan et al. for the *in-situ* degradation of hepatocytes have shown a role in the ablation of the tumour. Figure 2.9 shows the schematic representation of tumour cells treatment by Au NPs [52].

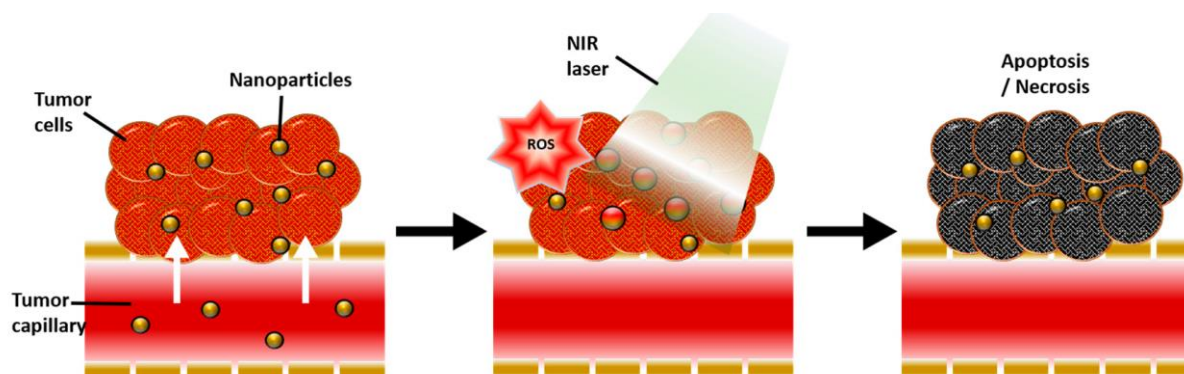


Figure 2.9: Schematic illustration of the physiological and biological effects of gold nanoparticle-mediated photothermal and photodynamic therapy [52].

Huang et al. have coupled antibodies with gold nanoparticles in the treatment of cancer cells [53]. These gold nanoparticles were useful with LSPR absorption which assured that laser frequency can be selective when it comes to heating and destroying cancer cells over healthy ones by using lower laser power. The reason for gold nanoparticles to use less laser power rely on their high absorption coefficients, which give them an advantage over conventional dyes employed in photothermal therapy and hence they result in massive destruction of cells causing less invasiveness. Dark-field imaging can be employed in therapy. Jain et al. have developed a photothermal therapy method that can be used to treat cancer cells that are resistant to chemotherapy [54]. Further development of photothermal therapy can be done considering numerous problems such as size and shape of nanoparticles with desired optical properties, enhanced accumulation of nanoparticles in tumours and applying the right amount of optical radiation and developing radiation source for heating gold nanoparticles.

Side effects resulting from the accumulation of gold nanoparticles in organs can be limited by coupling gold nanoparticles with a biopolymer such as polyethylene glycol or antibodies. In this case, particle concentration can be increased to target the specific tumour cells by merging the proteins with gold nanoparticles. A virus can also be destroyed by gold nanoparticles along with bacteria, denaturation of proteins and nucleic acids.

(b) Photodynamic therapy

Photodynamic therapy functions are almost similar to photothermal therapy. Photodynamic therapy makes use of photosensitizers to the patient body and laser irradiation is applied to the tissue at a wavelength of the absorption peak of dye. When using this technique, tumour cells are damaged using heat from a laser. Singlet oxygen is formed through the

photochemical generation and high active radicals are created to induce necrosis and apoptosis in tumour cells. The therapy also hinders tumour from feeding by applying damage on its micro-vessels which ultimately kill the tumour. However, the organism can develop immunity to photosensitizer which is one of the disadvantages of this method. Various research groups have employed gold nanoparticles to different nanocomposites because of their persistence to last longer.

(c) Drug vectors

Drug vectors are employed in pharmacology and medicine to deliver drugs, genes, and imaging agents to targeted cells and tissues. It is important to use a stable drug vector that can deliver agents into the circulatory system under appropriate conditions. The use of gold nanoparticles for drug delivery has already been reported due to their properties such as biocompatibility, optical properties, and their ability to merge with biomolecules and drugs. This procedure can be performed by using antigen-antibody and ligand-receptor interactions.

Drug delivery has been reported with great improvements when gold nanoparticles are merged with antitumors in the field of medicine. Labala et al. employed this technique by applying gold nanoparticles to polyvinylpyrrolidone and polyethyleneimine for transporting imatinib mesylate drugs to treat melanoma [55]. Liu et al. have incorporated gold nanoparticles in vincristine sulphate and applied to liposome for drug delivery responding to ultraviolet light [56]. Gold nanoparticles have been applied in the delivery of antibiotics and antibacterial agents. Burygin et al. have employed antibiotic-gold nanoparticles for various pathogenetic strains [57]. Gold nanoparticles have been reported by Thovhogi et al. to treat obesity by taking advantage of targeting ability and binding specificity of adipose homing peptide-functionalized gold nanoparticles to white adipose tissues [58]. Gold nanoparticles are also applied in gene therapy in which the gene can be constructed by either over-expression of the introduced gene or by partial or complete suppression of damaged or expressive genes.

2.5.1.4 Catalysis

Catalysis can also use metal nanoparticles to improve numerous chemical reactions such as hydrogenation, hydroformylation, carbonylation etc. This can be done by doping manganese oxide (MnO_2) used in water oxidation to improve its turn-over frequency. Kou et al. doped MnO_2 with gold nanoparticles which resulted in an increase of 8.2-fold in photochemical and

6-fold in electrochemical reactions better than uncoated MnO₂ [59]. Titanium silicate has also been doped with gold nanoparticles to increase the conversion of styrene-to-styrene oxides.

2.5.2 Silver nanoparticles

Silver nanoparticles are applied in commercialised household products such as cosmetics, toothpaste, soap, shampoos, detergents, washing machines, water purification systems as well as in the field of environmental remediation because of their unique antimicrobial and catalytic properties.

2.5.2.1 Antimicrobial agent

Silver has been employed in medicine from ancient times due to its healing and anti-disease properties. Silver vessels also have a role in the disinfection of water. Indian cuisine also employed silver during garnishing. In recent years silver nanoparticles constitute an antimicrobial agent in wound dressings, textiles, food storage containers and personal care appliances.

Sondi et al. used silver nanoparticles to destroy the cell membrane and cell wall of *Escherichia coli*, gram-negative bacteria found in the lower intestines of mammals [60]. Panáček et al. used silver nanoparticles against methicillin resistant *Staphylococcus aureus* which resulted in high bactericidal activity [61]. Silver nanoparticles need to be stable in order to work better since aggregates were found to decrease antimicrobial activity. To overcome the issue of aggregation in silver nanoparticles, the use of stabilising agents and variation of reaction parameters such as pH, temperature, the concentration of initial salt plays an important role. Sivera et al. stabilized silver nanoparticles in a pH range of 2-13 which resulted in lasting microbial activity [62].

Biofilm formation of *E. coli*, *S. aureus*, *Enterococcus sp.*, *Candida albicans* and *P. Aeruginosa* can be prevented by coating plastic catheters with silver nanoparticles. The process can also be applied against *B. Subtilis*. Silver nanoparticles have been reported in antimicrobial activity of polymethylmethacrylate (PMMA) in which they were loaded inside. Merging silver nanoparticles with antibiotics become valuable when applied against *S. aureus* and *E. coli* using the diffusion method. Attachment of silver nanoparticles to the cell membrane of bacteria can prevent respiration. Reduction in bacterial growth can be brought by dissipation of proton motive which occurs as a result of Ag⁺-membrane protein or phospholipids bilayer and therefore de-generation of the membrane and death of the cell.

2.5.2.2 Gas/Vapour sensing detectors

Tao et al. have used a thin monolayer of silver nanowires for the detection of chemicals employed in explosives [63]. The silver nanoparticles were closely packed in order to detect 2,4-dinitrotoluene in the chemical site. This is usually used in land mines and given off as vapour which was further detected using Raman spectroscopy. The use of the Langmuir-Blodgett assembly technique goes by floating nanowires on liquid have been reported.

2.5.2.3 Catalysis

Metal nanoparticles such as Au, Ag, and Pt along with their respective ions can catalyse luminal-H₂O₂ systems. Silver nanoparticles have been used as catalysts in dye degradation. Bastus et al. used silver nanoparticles stabilized by sodium citrate/tannic acid to reduce rhodamine B dye [64]. The catalytic activity of gelatin stabilised silver nanoparticles was used by Sinha et al. in the reduction of aromatic nitro compounds [65].

2.5.2.4 Water sterilization/purification

The properties of silver which include activity at low concentrations, odourless and have extremely low toxicity to humans possessed a high advantage in water sterilization. The process has been in use for a long time. Katadyn silver, which is described as spongy preparation of metallic silver along with the small proportion of palladium or gold was studied. In this case surface area of silver to be in contact with water has been increased. Microorganisms found in swimming pools can be hindered from growing through coating by silver nanoparticles.

Dankovich and Gray merged bactericidal paper with silver nanoparticles during purification of water which turned to be affordable as shown in Figure 2.10 [66]. Loo et al. have recently discovered the use of silver nanoparticles for disinfection of up to 3 logs of bacteria present in water within 15 minutes. Fernández et al. developed the use of silver nanoparticles in nitrocellulose membrane for purifying water [67].

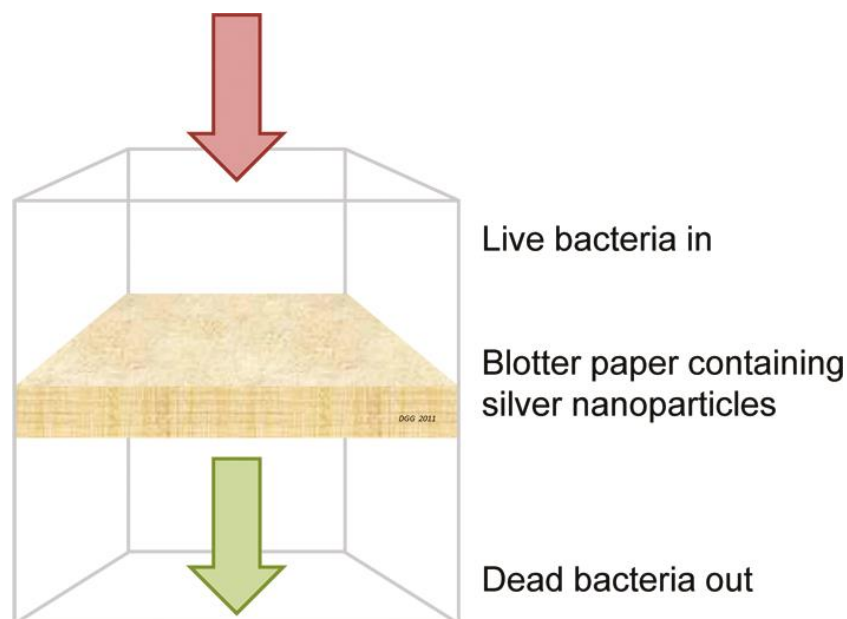


Figure 2.10: Schematic illustration for purification of water using bactericidal paper containing silver nanoparticles [67].

2.5.3 Platinum nanoparticles

Platinum is a noble metal that has seen a wide range of applications through its nanoparticles. They include commercialized products in cosmetics and pharmaceuticals, catalysis and other biomedical applications. Below are some platinum nanoparticles applications.

2.5.3.1 Biomedical applications

Treatment of cancer has been developed by using metal nanoparticles such as platinum included in drugs such as cisplatin, carboplatin, oxaliplatin, nedaplatin, lobaplatin and hepatoplatin. Platinum nanoparticles can be combined with other nanoparticles including bimetallic nanoclusters, alloy or core-shell in the biomedical sector. FePt@CoS₂ nanocrystals were experimented with against HeLa cells and resulted in higher killing efficiency as compared to cis-platin. The damage of cancer cells was found to be efficient when platinum nanoparticles were combined with irradiation which gives a big hope in cancer treatment.

2.5.3.2 Biosensors

Biosensors come into consideration in fields such as forensics, diagnostics, and environmental monitoring for detecting pathogens, harmful toxins and other biological agents. The sensor is composed of the recognition element and transducer. The recognition element helps in binding the target analyte molecule while the transducer's purpose is to

transduce the signal of the binding event. Signal to noise ratio can be increased by using nanoparticles in sensing applications.

Platinum nanoparticles are used for electrochemical analysis. The carbon film electrode has been modified with platinum nanoparticles for usage in a highly sensitive H_2O_2 sensor. The catalytic oxidation of H_2O_2 resulted in positive sensitivity to H_2O_2 which was better than the platinum bulk electrode. Deposition of gold-platinum (AuPt) alloy nanoparticles and carbon electrodes was used in the preparation of biosensors with ionic liquid and chitosan composite to detect the reduction of H_2O_2 . Li et al. have created a nonenzymatic glucose sensor by using nickel and platinum nanoparticles which reduced graphene oxide [68]. Carbon nanotubes and platinum nanoparticles were used in electrochemistry to create a biosensor.

2.5.3.3 Catalysis

Nanoparticles have been at the centre of catalysis in terms of factors such as enzyme loading, surface area and resistance to mass transfer. The different shapes of nanoparticles such as nanotubes, nanofibers and nanofibrous matrices have been brought to the table for optimization of biocatalysts. The electron transport chain of mitochondria has employed platinum nanoparticles for complex I (NADH: ubiquinone oxidoreductase activity) catalysation. Biocatalyzation use of platinum can also work in chemical reactions.

2.6 Noble metal nanoparticles in organic solar cells

Green and renewable energy have seen rapid growth in the recent fight against global warming. One of the renewable energy projects on the rise is solar energy which uses solar cells to convert sunlight to electrical energy. Sunlight is abundant throughout the world and can be a critical way to energise our systems. However, at the moment the conversion of sunlight with solar cells is still very low [69]. Inorganic solar cells such as silicon solar cells are leading in the market [2, 70]. However, producing silicon solar cells is expensive as compared to other energy sources available. Organic solar cells (OSCs) have come into interest due to their remarkable characteristics including low-cost production. There is a lot of improvement to be made on OSCs for them to be commercialised since their PCE is very low.

2.6.1 Properties of organic solar cells

OSCs are composed of polymers (organic compounds) sandwiched between two electrodes (anode and cathode) which are used as electronics for the conversion of sunlight to electrical

energy. Research in OSCs has been brought to attention simply due to the properties which include ultra-thin, lightweight, low-cost, low-temperature fabrication, semi-transparency, and mechanical flexibility [71]. **Error! Reference source not found.** illustrates the flexibility of SCs which makes durability better [2, 4]. Various architectures such as tandem cells, plasmon-enhanced cells, and the use of carbon nanomaterials with organic materials have been developed in recent years for the progression of OSCs.

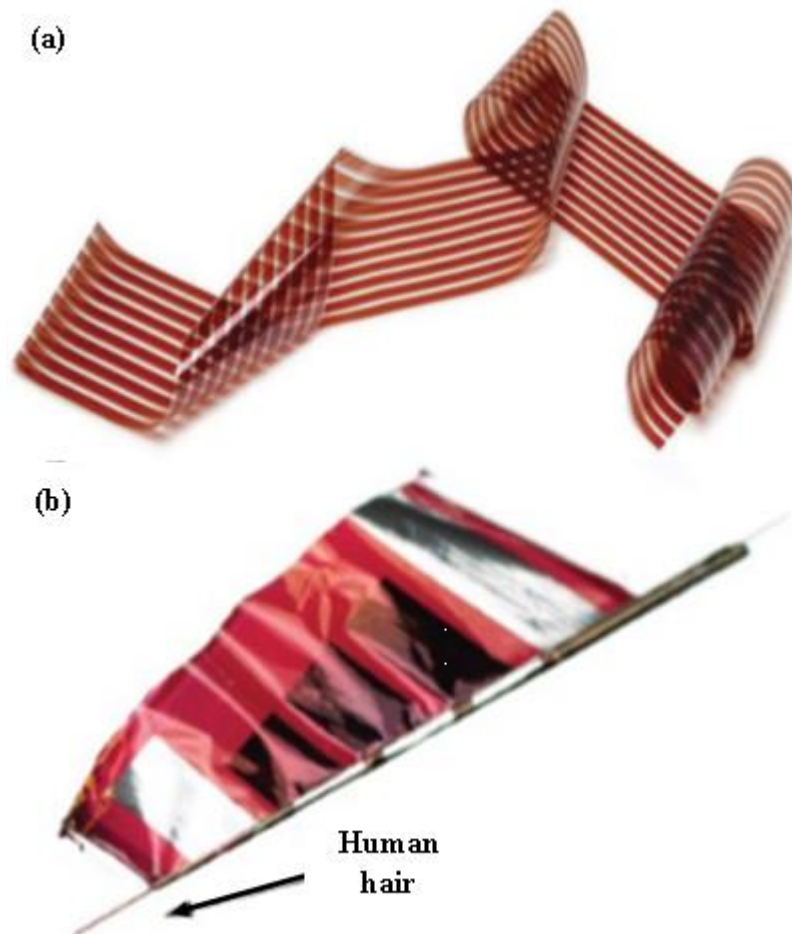


Figure 2.11: Flexibility of organic solar cells in (a) rolled around [2] and (b) wrapped around human hair [4].

OSCs are formed by donor and acceptor materials which form donor-acceptor structures upon contact. When the light of enough photon energy enters the donor material, a hole is formed when an electron of equal energy is transferred from the highest occupied molecular orbital (HOMO) to the lowest unoccupied molecular orbital (LUMO) creating an exciton (photoexcitation pair). For charge transfer to occur, the exciton must be dissociated before it recombines.

2.6.2 Architecture of OSC

The basic structure of OSC contains donor and acceptor which interact upon contact. This is a bilayer heterojunction (containing two layers) also referred to as planar which is sandwiched between two electrodes resulting in ohmic contact. The donor is in contact with a transparent cathode of high work function whereas the acceptor is in contact with an anode of low work function. Iodine-doped tin oxide (ITO) and fluorine-doped tin oxide have been extensively used as anodes. Bulk heterojunction OSCs have been developed with a larger separation (1 nm) between the donor and acceptor entities [2]. As light enters the solar cell through the anode, excitons dissociate in the donor-acceptor to anode and cathode. In a planar heterojunction solar cell, a lot of charge recombination occurs due to the short diffusion. This causes the OSC to have low PCE since only the exciton near the donor-acceptor interface dissociates successfully. The bulk heterojunction overcomes the problem by inserting a photoactive layer between donor and acceptor layers [69]. The photoactive layer should however not be too thick (not more than 100 nm) as this will result in charge recombination which will reduce PCE.

2.6.3 Plasmonic principles

Plasmonics is derived from plasmons which are quantum plasma oscillations or oscillations of electron density in a metal. These electrons are formed in a valence shell of metals such as gold, silver, copper and others in which the electrons will move against the direction of the electric field from the light. There have been three types of plasmons.

Volume or bulk plasmons occur when the free electrons induced in a metal oscillate in a longitudinal wave manner [72]. These kinds of plasmons can also be excited in semiconductors and insulators in their valence band. An electron beam is shown on the homogeneous electrons already present in a solid which will, in turn, form an induced Coulomb force to create quantised longitudinal oscillations of electrons in a certain frequency. The energy of volume plasmons is given by:

$$E_p = \hbar\omega_p = \hbar \sqrt{\frac{4\pi e^2 N}{m}}$$

where $\hbar = h/2\pi$, h is the Planck's constant, ω_p is the angular frequency, N is the electron density, e is the electron charge and m is the mass of an electron.

Surface plasmons occur at the interface of two materials (e.g., metal surface or metal and dielectric material) and have lower energy as compared to volume plasmons. The two types are surface plasmon polaritons which occur at a planar surface and localised surface plasmons which occur at a closed surface of a small particle, both are excitation of charged motion and electromagnetic fields [73]. The longitudinal oscillations are induced by the electric field components parallel to the surface whereas the electromagnetic waves are induced by the electric field vertical to the surface. The vertical electric field shows a transverse wave.

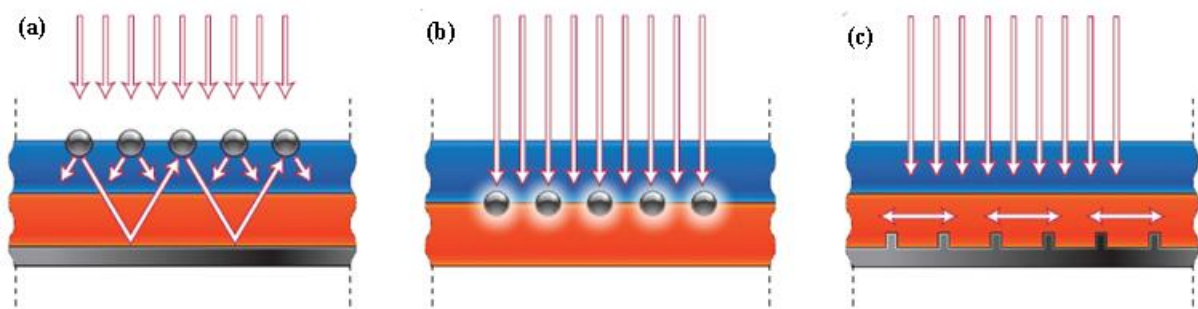


Figure 2.12: Plasmonic light scattering in solar cells using metal nanoparticles as (a) bulk plasmons, (b) localised surface plasmons and (c) surface plasmons polaritons [73].

Surface plasmon polaritons (SPP) are electromagnetic excitations that travel or propagates between metal and dielectric or metal and air interface perpendicular to the surface of interest. Excitations of SPPs can be brought by either electrons or photons. By firing a beam of electrons on metal will result in scattering the electrons already present on a metal which will transfer energy into the bulk plasma and SPPs are formed. The energy SPP is given by:

$$E_{SPP} = \hbar \omega_P / \sqrt{2}$$

SPPs are applied in microscopy and lithography by enabling subwavelength optics, photonics data storage, light generation and bio-photonics among others.

Localised surface plasmons occur when the incident light strikes a metal nanoparticle with a lesser wavelength. For this to happen, the oscillating electric field is irradiated by light in which the restoring force from the Coulomb attraction will arise and course the electrons to oscillate. Unlike the SPPs, LSPs are non-propagating plasmons. The energy is given by:

$$E_{LSP} = \hbar \omega_P / \sqrt{3}$$

Applications vary from measuring resonant frequency, surface plasmon resonance, creation of super lenses and so on.

2.7 Plasmonics in organic solar cells

The short diffusion length present in OSCs (10 – 40 nm) gave rise to the use of plasmonic NPs to increase scattering in the ultra-thin photoactive layer [74]. This technique traps more photons inside the photoactive layer without increasing the size of the photoactive layer itself. NPs can be incorporated in one of the polymers.

2.7.1 Metal nanoparticles in the buffer layer

Au NPs as the buffer layer results in elevation of light absorption in the active layer [75]. The exciton dissociation will then occur at the donor/acceptor interface. Ng *et al.* has incorporated Au NPs nanocubes (NCs) in PTB7:PCBM which resulted in PCE of about 8.2% [76]. Petridis *et al.* archived PCE of 6.28% with the inclusion of NPs in PCPDTBT:C₇₀PCBM in which the photons were transmitted back to the active layer [77]. Qia *et al.* varied the diameter of Au NPs in the buffer layer which improved the solar cell by 20% due to the strong SPR effect from larger particles [78]. Au NPs consist of broader LSPR in the visible spectrum as compared to Ag NPs. However, Ag NPs contains a higher scattering factor than Au NPs. In this case, it can also be useful if both (Au and Ag NPs) are included in the buffer layer at the same time to overcome individual effects of each other. Baek *et al.* combined the two metal NPs to enhance PCE of various devices with Au@Ag core-shell NCs [79].

The incorporation of Ag NPs in the buffer layer has also shown an increase in the performance of OSC due to their plasmonic effect in the near-infrared and visible spectrum [80]. Noh *et al.* incorporated Ag nanoprisms (NPSs) in P3HT:PCBM in which the PCE of their bulk heterojunction solar cell was to be 5.1% [81]. Wang *et al.* have used Ag nanowires (NWs) as a transparent conducting electrode to obtain PCE of 7.58% in their efficient flexible OSC [82]. This PCE was enhanced by high light trapping and scattering from Ag NW mesh into the active layer.

2.7.2 Metal nanoparticles in the active layer

Carrier mobility of OSCs can be improved by embedding metal NPs in the active layer which will also enhance PCE [83]. Wang *et al.* have incorporated octahedral Au NPs in P3HT:

PCBM, PCDTBT: PCBM and Si-PCPDTBT: PCBM to reduce exciton quenching and cell resistance which resulted in a PCE of 4.36%, 6.45% and 4.54%, respectively [84]. Au NPs has resulted in multiple light scattering which caused longer optical path without increasing the thickness and enhanced PCE of the solar cell. Xu *et al.* have integrated Au-silica NSs and NRs in the active layer of p-DTS (FBTTh₂):PC₇₀BM which resulted in an increase of J_{sc} from 12.04 to 12.69 and 15.14 mA/cm² respectively without changing V_{oc} and fill factor (FF) [85]. The integration of Au-silica NSs and NRs in the active layer of p-DTS (FBTTh₂):PC₇₀BM have resulted in PCE of 6.9 and 8.2% respectively.

Ag nanostructures of various forms have diverse properties, such as absorbance and reflectivity. Several studies have shown that Ag nanoparticles have a more effective light scattering effect than Au nanostructures. As a result, a comparison of Ag nanoplates and AgNPs in the active layer of various devices revealed differing degrees of optical reflectance and absorption spectra. Due to the electron/hole carrier mobility in AgNWs based devices, which is 1.5 times greater than AgNPs based devices, Kim et al. presented a comparative study of AgNPs and AgNWs in the active layer of P3HT: PCBM to raise the device's performance to 3.56 and 3.91%, respectively, owing to the electron/hole carrier mobility in AgNWs based devices, which is 1.5 times greater than AgNPs based devices. As a result of the increase in J_{sc} and PCE, electrical conductivity improves. Chen et al. synthesized different ratios of AuAg alloy NPs with numerous stabilizing ligands to intermingle with P3HT:PC₆₁BM layer, with PCE of 4.73 and 3.53 %, respectively, compared to AgNPs-based device with 4.60 per cent efficiency.

2.8 References

- [1] S. Link and M. A. El-Sayed, "Size and temperature dependence of the plasmon absorption of colloidal gold nanoparticles," *The Journal of Physical Chemistry B*, vol. 103, no. 21, pp. 4212-4217, 1999.
- [2] O. A. Abdulrazzaq, V. Saini, S. Bourdo, E. Dervishi, and A. S. Biris, "Organic Solar Cells: A Review of Materials, Limitations, and Possibilities for Improvement," *Particulate Science and Technology*, vol. 31, no. 5, pp. 427-442, 2013/09/03 2013.
- [3] P. K. Jain, X. Huang, I. H. El-Sayed, and M. A. El-Sayed, "Noble metals on the nanoscale: optical and photothermal properties and some applications in imaging, sensing, biology, and medicine," *Accounts of chemical research*, vol. 41, no. 12, pp. 1578-1586, 2008.
- [4] M. Kaltenbrunner *et al.*, "Ultrathin and lightweight organic solar cells with high flexibility," *Nature Communications*, Article vol. 3, p. 770, 04/03/online 2012.
- [5] B. K. Mehta, M. Chhajlani, and B. D. Shrivastava, "Green synthesis of silver nanoparticles and their characterization by XRD," *Journal of Physics: Conference Series*, vol. 836, p. 012050, 2017/05/31 2017.
- [6] V. Pareek, A. Bhargava, R. Gupta, N. Jain, and J. Panwar, "Synthesis and applications of noble metal nanoparticles: a review," *Advanced Science, Engineering and Medicine*, vol. 9, no. 7, pp. 527-544, 2017.
- [7] B. R. Cuenya, "Synthesis and catalytic properties of metal nanoparticles: Size, shape, support, composition, and oxidation state effects," *Thin Solid Films*, vol. 518, no. 12, pp. 3127-3150, 2010.
- [8] K. L. Kelly, E. Coronado, L. L. Zhao, and G. C. Schatz, "The optical properties of metal nanoparticles: the influence of size, shape, and dielectric environment," ed: ACS Publications, 2003.
- [9] P. K. Jain, X. Huang, I. H. El-Sayed, and M. A. El-Sayed, "Review of some interesting surface plasmon resonance-enhanced properties of noble metal nanoparticles and their applications to biosystems," *Plasmonics*, vol. 2, no. 3, pp. 107-118, 2007.
- [10] R. Narayanan and M. A. El-Sayed, "Shape-dependent catalytic activity of platinum nanoparticles in colloidal solution," *Nano letters*, vol. 4, no. 7, pp. 1343-1348, 2004.

- [11] N. T. Thanh and L. A. Green, "Functionalisation of nanoparticles for biomedical applications," *Nano Today*, vol. 5, no. 3, pp. 213-230, 2010.
- [12] A. H. A. Nasria, S. Thahab, and S. Hussain, "JOURNAL OF KUFA– PHYSICS."
- [13] J. B. ten Hove, L. M. Schijven, J. Wang, and A. H. Velders, "Size-controlled and water-soluble gold nanoparticles using UV-induced ligand exchange and phase transfer," *Chemical communications*, vol. 54, no. 95, pp. 13355-13358, 2018.
- [14] L. L. Rouhana, J. A. Jaber, and J. B. Schlenoff, "Aggregation-resistant water-soluble gold nanoparticles," *Langmuir*, vol. 23, no. 26, pp. 12799-12801, 2007.
- [15] K. Sneha, A. Esterle, N. Sharma, and S. Sahi, "Yucca-derived synthesis of gold nanomaterial and their catalytic potential," *Nanoscale research letters*, vol. 9, p. 627, 11/23 2014.
- [16] J. Hu, Z. Wang, and J. Li, "Gold nanoparticles with special shapes: controlled synthesis, surface-enhanced Raman scattering, and the application in biodetection," *Sensors*, vol. 7, no. 12, pp. 3299-3311, 2007.
- [17] T. Taufikurohmah, "TEM Analysis of Gold Nanoparticles Synthesis in Glycerin: Novel Safety Materials in Cosmetics to Recovery Mercury Damage," *Research Journal of Pharmaceutical, Biological and Chemical Sciences*, vol. 5, pp. 397-407, 01/01 2014.
- [18] J. Li, T. Zhao, T. Chen, Y. Liu, C. N. Ong, and J. Xie, "Engineering noble metal nanomaterials for environmental applications," *Nanoscale*, vol. 7, no. 17, pp. 7502-7519, 2015.
- [19] T. Pradeep, "Noble metal nanoparticles for water purification: a critical review," *Thin solid films*, vol. 517, no. 24, pp. 6441-6478, 2009.
- [20] N. R. Jana, L. Gearheart, and C. J. Murphy, "Wet chemical synthesis of silver nanorods and nanowires of controllable aspect ratio Electronic supplementary information (ESI) available: UV–VIS spectra of silver nanorods. See <http://www.rsc.org/suppdata/cc/b1/b100521i>," *Chemical Communications*, no. 7, pp. 617-618, 2001.
- [21] P. K. Jain, K. S. Lee, I. H. El-Sayed, and M. A. El-Sayed, "Calculated absorption and scattering properties of gold nanoparticles of different size, shape, and composition: applications in biological imaging and biomedicine," *The journal of physical chemistry B*, vol. 110, no. 14, pp. 7238-7248, 2006.
- [22] L. Ammosova, Y. Jiang, M. Suvanto, and T. A. Pakkanen, "Precise micropatterning of silver nanoparticles on plastic substrates," *Applied Surface Science*, vol. 401, pp. 353-361, 2017/04/15/ 2017.

- [23] S. Kim, B. Liu, and M. Zachariah, "Synthesis of nanoporous metal oxide particles by a new inorganic matrix spray pyrolysis method," *Chemistry of materials*, vol. 14, no. 7, pp. 2889-2899, 2002.
- [24] C. Piras, S. Fernandez Prieto, and W. Borggraeve, "Ball milling : A green technology for the preparation and functionalisation of nanocellulose derivatives," *Nanoscale Advances*, 01/09 2019.
- [25] S. Rostami, A. Mehdinia, and A. Jabbari, "Seed-mediated grown silver nanoparticles as a colorimetric sensor for detection of ascorbic acid," *Spectrochimica Acta Part A: Molecular and Biomolecular Spectroscopy*, vol. 180, pp. 204-210, 2017/06/05/ 2017.
- [26] J. Zhang and J. Fang, "A General Strategy for Preparation of Pt 3d-Transition Metal (Co, Fe, Ni) Nanocubes," *Journal of the American Chemical Society*, vol. 131, no. 51, pp. 18543-18547, 2009/12/30 2009.
- [27] M. Soleimani Zohr Shiri, W. Henderson, and M. R. Mucalo, "A Review of The Lesser-Studied Microemulsion-Based Synthesis Methodologies Used for Preparing Nanoparticle Systems of The Noble Metals, Os, Re, Ir and Rh," *Materials (Basel, Switzerland)*, vol. 12, no. 12, Accessed on: 2019/06//. doi: 10.3390/ma12121896
- [28] X. Xu *et al.*, "Fabrication of Gold Nanoparticles by Laser Ablation in Liquid and Their Application for Simultaneous Electrochemical Detection of Cd²⁺, Pb²⁺, Cu²⁺, Hg²⁺," *ACS Applied Materials & Interfaces*, vol. 6, no. 1, pp. 65-71, 2014/01/08 2014.
- [29] F. Mafuné, J.-y. Kohno, Y. Takeda, T. Kondow, and H. Sawabe, "Formation of gold nanoparticles by laser ablation in aqueous solution of surfactant," *The Journal of Physical Chemistry B*, vol. 105, no. 22, pp. 5114-5120, 2001.
- [30] F. Mafuné, J.-y. Kohno, Y. Takeda, T. Kondow, and H. Sawabe, "Formation and size control of silver nanoparticles by laser ablation in aqueous solution," *The Journal of Physical Chemistry B*, vol. 104, no. 39, pp. 9111-9117, 2000.
- [31] F. Mafuné, J.-y. Kohno, Y. Takeda, T. Kondow, and H. Sawabe, "Structure and stability of silver nanoparticles in aqueous solution produced by laser ablation," *The Journal of Physical Chemistry B*, vol. 104, no. 35, pp. 8333-8337, 2000.
- [32] E. Jimenez, K. Abderrafi, R. Abargues, J. L. Valdes, and J. P. Martinez-Pastor, "Laser-ablation-induced synthesis of SiO₂-capped noble metal nanoparticles in a single step," *Langmuir*, vol. 26, no. 10, pp. 7458-7463, 2010.

- [33] G. Gahlawat and A. R. Choudhury, "A review on the biosynthesis of metal and metal salt nanoparticles by microbes," *RSC Advances*, 10.1039/C8RA10483B vol. 9, no. 23, pp. 12944-12967, 2019.
- [34] T. Klaus, R. Joerger, E. Olsson, and C.-G. Granqvist, "Silver-based crystalline nanoparticles, microbially fabricated," *Proceedings of the National Academy of Sciences*, vol. 96, no. 24, pp. 13611-13614, 1999.
- [35] A. R. Shahverdi, A. Fakhimi, H. R. Shahverdi, and S. Minaian, "Synthesis and effect of silver nanoparticles on the antibacterial activity of different antibiotics against *Staphylococcus aureus* and *Escherichia coli*," *Nanomedicine: Nanotechnology, Biology and Medicine*, vol. 3, no. 2, pp. 168-171, 2007.
- [36] S. He, Z. Guo, Y. Zhang, S. Zhang, J. Wang, and N. Gu, "Biosynthesis of gold nanoparticles using the bacteria *Rhodospseudomonas capsulata*," *Materials Letters*, vol. 61, no. 18, pp. 3984-3987, 2007.
- [37] P. Mukherjee *et al.*, "Bioreduction of $AuCl_4^-$ ions by the fungus, *Verticillium sp.* and surface trapping of the gold nanoparticles formed," *Angewandte Chemie International Edition*, vol. 40, no. 19, pp. 3585-3588, 2001.
- [38] M. Guilger-Casagrande and R. d. Lima, "Synthesis of Silver Nanoparticles Mediated by Fungi: A Review," (in English), *Frontiers in Bioengineering and Biotechnology*, Review vol. 7, no. 287, 2019-October-22 2019.
- [39] T. Riddin, M. Gericke, and C. Whiteley, "Analysis of the inter-and extracellular formation of platinum nanoparticles by *Fusarium oxysporum f. sp. lycopersici* using response surface methodology," *Nanotechnology*, vol. 17, no. 14, p. 3482, 2006.
- [40] J. Xie, J. Y. Lee, D. I. Wang, and Y. P. Ting, "Silver nanoplates: from biological to biomimetic synthesis," *ACS nano*, vol. 1, no. 5, pp. 429-439, 2007.
- [41] S. N. Sinha, D. Paul, N. Halder, D. Sengupta, and S. K. Patra, "Green synthesis of silver nanoparticles using fresh water green alga *Pithophora oedogonia* (Mont.) Wittrock and evaluation of their antibacterial activity," *Applied Nanoscience*, vol. 5, no. 6, pp. 703-709, 2015.
- [42] G. Singaravelu, J. Arockiamary, V. G. Kumar, and K. Govindaraju, "A novel extracellular synthesis of monodisperse gold nanoparticles using marine alga, *Sargassum wightii* Greville," *Colloids and surfaces B: Biointerfaces*, vol. 57, no. 1, pp. 97-101, 2007.
- [43] J. Gardea-Torresdey *et al.*, "Formation and growth of Au nanoparticles inside live alfalfa plants," *Nano letters*, vol. 2, no. 4, pp. 397-401, 2002.

- [44] S. S. Shankar, A. Ahmad, R. Pasricha, and M. Sastry, "Bioreduction of chloroaurate ions by geranium leaves and its endophytic fungus yields gold nanoparticles of different shapes," *Journal of Materials Chemistry*, vol. 13, no. 7, pp. 1822-1826, 2003.
- [45] A. T. Shah, M. I. Din, S. Bashir, M. A. Qadir, and F. Rashid, "Green synthesis and characterization of silver nanoparticles using *Ferocactus echidne* extract as a reducing agent," *Analytical Letters*, vol. 48, no. 7, pp. 1180-1189, 2015.
- [46] B. Ankamwar, M. Chaudhary, and M. Sastry, "Gold Nanotriangles Biologically Synthesized using Tamarind Leaf Extract and Potential Application in Vapor Sensing," *Synthesis and Reactivity in Inorganic, Metal-Organic, and Nano-Metal Chemistry*, vol. 35, no. 1, pp. 19-26, 2005/01/01 2005.
- [47] M. Gholami-Shabani, Z. Gholami-Shabani, M. Shams-Ghahfarokhi, F. Jamzivar, and M. Razzaghi-Abyaneh, "Green Nanotechnology: Biomimetic Synthesis of Metal Nanoparticles Using Plants and Their Application in Agriculture and Forestry," in *Nanotechnology: An Agricultural Paradigm*, R. Prasad, M. Kumar, and V. Kumar, Eds. Singapore: Springer Singapore, 2017, pp. 133-175.
- [48] J. Huang *et al.*, "Biosynthesis of silver and gold nanoparticles by novel sundried *Cinnamomum camphora* leaf," *Nanotechnology*, vol. 18, p. 105104, March 01, 2007 2007.
- [49] K. Paul, B. G. Bag, and K. Samanta, "Green coconut (*Cocos nucifera* Linn) shell extract mediated size controlled green synthesis of polyshaped gold nanoparticles and its application in catalysis," *Applied nanoscience*, vol. 4, no. 6, pp. 769-775, 2014.
- [50] A. I. Nossier, S. Eissa, M. F. Ismail, M. A. Hamdy, and H. M. E.-S. Azzazy, "Direct detection of hyaluronidase in urine using cationic gold nanoparticles: a potential diagnostic test for bladder cancer," *Biosensors and Bioelectronics*, vol. 54, pp. 7-14, 2014.
- [51] M. K. Gehrman *et al.*, "Imaging of Hsp70-positive tumors with cmHsp70. 1 antibody-conjugated gold nanoparticles," *International journal of nanomedicine*, vol. 10, p. 5687, 2015.
- [52] H. S. Kim and D. Y. Lee, "Near-infrared-responsive cancer photothermal and photodynamic therapy using gold nanoparticles," *Polymers*, vol. 10, no. 9, p. 961, 2018.

- [53] X. Huang, P. K. Jain, I. H. El-Sayed, and M. A. El-Sayed, "Plasmonic photothermal therapy (PPTT) using gold nanoparticles," *Lasers in medical science*, vol. 23, no. 3, pp. 217-228, 2008.
- [54] P. K. Jain, I. H. El-Sayed, and M. A. El-Sayed, "Au nanoparticles target cancer," *nano today*, vol. 2, no. 1, pp. 18-29, 2007.
- [55] S. Labala, P. K. Mandapalli, A. Kurumaddali, and V. V. K. Venuganti, "Layer-by-layer polymer coated gold nanoparticles for topical delivery of imatinib mesylate to treat melanoma," *Molecular pharmaceutics*, vol. 12, no. 3, pp. 878-888, 2015.
- [56] Y. Liu *et al.*, "Delivery of vincristine sulfate-conjugated gold nanoparticles using liposomes: a light-responsive nanocarrier with enhanced antitumor efficiency," *International journal of nanomedicine*, vol. 10, p. 3081, 2015.
- [57] G. Burygin, B. Khlebtsov, A. Shantrokha, L. Dykman, V. Bogatyrev, and N. Khlebtsov, "On the enhanced antibacterial activity of antibiotics mixed with gold nanoparticles," *Nanoscale research letters*, vol. 4, no. 8, pp. 794-801, 2009.
- [58] N. Thovhogi, N. Sibuyi, M. Meyer, M. Onani, and A. Madiehe, "Targeted delivery using peptide-functionalised gold nanoparticles to white adipose tissues of obese rats," *Journal of Nanoparticle Research*, vol. 17, no. 2, pp. 1-8, 2015.
- [59] C. H. Kuo *et al.*, "Understanding the role of gold nanoparticles in enhancing the catalytic activity of manganese oxides in water oxidation reactions," *Angewandte Chemie International Edition*, vol. 54, no. 8, pp. 2345-2350, 2015.
- [60] I. Sondi and B. Salopek-Sondi, "Silver nanoparticles as antimicrobial agent: a case study on E. coli as a model for Gram-negative bacteria," *Journal of colloid and interface science*, vol. 275, no. 1, pp. 177-182, 2004.
- [61] A. Panáček *et al.*, "Silver colloid nanoparticles: synthesis, characterization, and their antibacterial activity," *The Journal of Physical Chemistry B*, vol. 110, no. 33, pp. 16248-16253, 2006.
- [62] M. Sivera *et al.*, "Silver nanoparticles modified by gelatin with extraordinary pH stability and long-term antibacterial activity," *PloS one*, vol. 9, no. 8, p. e103675, 2014.
- [63] A. Tao *et al.*, "Langmuir–Blodgett silver nanowire monolayers for molecular sensing using surface-enhanced Raman spectroscopy," *Nano letters*, vol. 3, no. 9, pp. 1229-1233, 2003.

- [64] N. G. Bastús, F. Merkoçi, J. Piella, and V. Puentes, "Synthesis of highly monodisperse citrate-stabilized silver nanoparticles of up to 200 nm: kinetic control and catalytic properties," *Chemistry of Materials*, vol. 26, no. 9, pp. 2836-2846, 2014.
- [65] T. Sinha, M. Ahmaruzzaman, A. Sil, and A. Bhattacharjee, "Biomimetic synthesis of silver nanoparticles using the fish scales of *Labeo rohita* and their application as catalysts for the reduction of aromatic nitro compounds," *Spectrochimica Acta Part A: Molecular and Biomolecular Spectroscopy*, vol. 131, pp. 413-423, 2014.
- [66] T. A. Dankovich and D. G. Gray, "Bactericidal Paper Impregnated with Silver Nanoparticles for Point-of-Use Water Treatment," *Environmental Science & Technology*, vol. 45, no. 5, pp. 1992-1998, 2011/03/01 2011.
- [67] J. G. Fernández, C. A. Almeida, M. A. Fernández-Baldo, E. Felici, J. Raba, and M. I. Sanz, "Development of nitrocellulose membrane filters impregnated with different biosynthesized silver nanoparticles applied to water purification," *Talanta*, vol. 146, pp. 237-243, 2016.
- [68] M. Li, X. Bo, Z. Mu, Y. Zhang, and L. Guo, "Electrodeposition of nickel oxide and platinum nanoparticles on electrochemically reduced graphene oxide film as a nonenzymatic glucose sensor," *Sensors and Actuators B: Chemical*, vol. 192, pp. 261-268, 2014.
- [69] L. Feng, M. Niu, Z. Wen, and X. Hao, "Recent Advances of Plasmonic Organic Solar Cells: Photophysical Investigations," *Polymers*, vol. 10, no. 2, p. 123, 2018.
- [70] L. Meng *et al.*, "Organic and solution-processed tandem solar cells with 17.3% efficiency," *Science*, vol. 361, no. 6407, pp. 1094-1098, 2018.
- [71] J.-L. Wu *et al.*, "Surface plasmonic effects of metallic nanoparticles on the performance of polymer bulk heterojunction solar cells," *ACS nano*, vol. 5, no. 2, pp. 959-967, 2011.
- [72] A. Rider, K. Ostrikov, and S. Furman, "Plasmas meet plasmonics Everything old is new again," *European Physical Journal D*, vol. 66, 09/01 2012.
- [73] H. Atwater and A. Polman, "Plasmonics for Improved Photovoltaic Devices," *Nature materials*, vol. 9, p. 865, 10/01 2010.
- [74] M. Notarianni, K. Vernon, A. Chou, M. Aljada, J. Liu, and N. Motta, "Plasmonic effect of gold nanoparticles in organic solar cells," *Solar Energy*, vol. 106, pp. 23-37, 2014.

- [75] P. J. Maake, A. S. Bolokang, C. J. Arendse, V. Vohra, E. I. Iwuoha, and D. E. Motaung, "Metal oxides and noble metals application in organic solar cells," *Solar Energy*, vol. 207, pp. 347-366, 2020/09/01/ 2020.
- [76] A. Ng *et al.*, "Enhanced performance of PTB7:PC₇₁BM solar cells via different morphologies of gold nanoparticles," (in eng), *ACS applied materials & interfaces*, vol. 6, no. 23, pp. 20676-20684, 2014/12// 2014.
- [77] C. Petridis, K. Savva, E. Kymakis, and E. Stratakis, "Laser generated nanoparticles based photovoltaics," *Journal of Colloid and Interface Science*, vol. 489, pp. 28-37, 2017/03/01/ 2017.
- [78] L. Qiao *et al.*, "Localized surface plasmon resonance enhanced organic solar cell with gold nanospheres," *Applied Energy*, vol. 88, no. 3, pp. 848-852, 2011/03/01/ 2011.
- [79] S.-W. Baek *et al.*, "Au@Ag Core–Shell Nanocubes for Efficient Plasmonic Light Scattering Effect in Low Bandgap Organic Solar Cells," *ACS Nano*, vol. 8, no. 4, pp. 3302-3312, 2014/04/22 2014.
- [80] W. R. Erwin, H. F. Zarick, E. M. Talbert, and R. Bardhan, "Light trapping in mesoporous solar cells with plasmonic nanostructures," *Energy & Environmental Science*, vol. 9, no. 5, pp. 1577-1601, 2016.
- [81] H. S. Noh, E. H. Cho, H. M. Kim, Y. D. Han, and J. Joo, "Organic solar cells using plasmonics of Ag nanoprisms," *Organic Electronics*, vol. 14, no. 1, pp. 278-285, 2013/01/01/ 2013.
- [82] B. Y. Wang *et al.*, "Enhanced light scattering and trapping effect of Ag nanowire mesh electrode for high efficient flexible organic solar cell," *Small*, vol. 11, no. 16, pp. 1905-1911, 2015.
- [83] Y.-Y. Yu and S.-H. Chan, "Metallic nanoparticles in active layer for hybrid photovoltaic device applications," *Thin Solid Films*, vol. 544, pp. 175-181, 2013/10/01/ 2013.
- [84] D. H. Wang *et al.*, "Enhanced power conversion efficiency in PCDTBT/PC70BM bulk heterojunction photovoltaic devices with embedded silver nanoparticle clusters," *Advanced Energy Materials*, vol. 1, no. 5, pp. 766-770, 2011.
- [85] D. T. Nguyen, T. Tran, L. Nguyen Ngoc, L. Long, and Vu, *SYNTHESIS OF GOLD NANOPARTICLES FROM BULK METALLIC GOLD BY A SONOELECTROCHEMICAL METHOD*. 2010.

Chapter 3

Experimental

3.1 Materials

All materials used in this experiment were obtained from Sigma Aldrich. Chloroauric acid (HAuCl_3), silver nitrate, copper (II) sulphate pentahydrate ($\text{CuSO}_4 \cdot 5\text{H}_2\text{O}$), ascorbic acid, polyvinyl pyrrolidone (PVP), trisodium citrate, sodium hydroxide (NaOH), sodium borohydride (NaBH_4), and P3HT: PC_{61}BM were all used as received. PEDOT: PSS and indium tin oxide (ITO) coated glass substrates were purchased for Ossila.

3.2 Synthesis of gold and silver nanoparticles

3.2.1 Gold NPs

The Au NPs used in this study were synthesized by the chemical reduction method from Tom et al [1]. A total of 18.5 mL of water and 0.5 mL of 10^{-2} M trisodium citrate were thoroughly mixed. 0.5 mL (1 mM) HAuCl_3 was added to the solution, and the mixture was stirred for 30 minutes. 0.1 M NaBH_4 (0.5 mL) was gradually added to the above mixture and stirred until the colour changed to purple. The same concentration of aqueous trisodium citrate and chloroauric acid was used to prepare Au NPs with a diameter of 5 – 13 nm, which were then heated together until the colour changed to wine red.

3.2.2 Silver NPs

Citrate-stabilized Ag NPs were synthesized using a method described by Doty et al [2]. A 200 mL solution of AgNO_3 (0.25 mM) and trisodium citrate (0.25 mM) were mixed with a 10 mL aqueous solution of NaBH_4 (10 mM). After 30 minutes of stirring, the reaction produced a yellow colloidal Ag solution. The technique was repeated with half the concentration of NaBH_4 in the second group of Ag NPs (5 mM NaBH_4). The resulting colloidal solution, in this case, had a bright yellow colour.

3.2.3 Copper NPs

Citrate-capped Cu NPs were synthesized with a procedure adapted from Dang et al [3]. 52.8 mg of ascorbic acid was dissolved in 15 ml of deionized water to make an ascorbic acid solution [3].

Separately, a $\text{CuSO}_4 \cdot 5\text{H}_2\text{O}$ (0.01 M) solution in deionized water was produced and added to the ascorbic acid solution under vigorous magnetic stirring. To adjust nanoparticle size, PVP

(0.01 M) was applied. The pH was then adjusted to 12 by adding a dropwise solution of NaOH (1 M) in deionized water. After about 1 hour of stirring at room temperature, a 0.1 M NaBH₄ solution in deionized water was added to the mixture and stirred vigorously for about 10 minutes [3]. The reaction mixture's initial blue colour faded to yellow, then pale brown. The copper NPs were separated and rinsed with deionized water by centrifugation, with excess PVP removed using acetone as a non-solvent. The precipitates were dried for 3–4 hours.

3.3 Substrate cleaning

The substrates used in the study are ITO pre-patterned glass substrates with dimensions of 20 mm x 15 mm x 2 mm. The substrates were cleaned by immersing them in a NaOH solution for 10 minutes and then washing them with deionized water [4]. The substrates were soaked in ethanol and agitated in an ultrasonic bath for 10 minutes after being rinsed. The substrates were then rinsed with deionised water and agitated in acetone under the same conditions, before being rinsed again with deionised water and blown dry with nitrogen gas [4]. To improve wettability, the cleaned substrates were exposed to UV ozone cleaner for 15 minutes.

3.4 Fabrication of solar cell

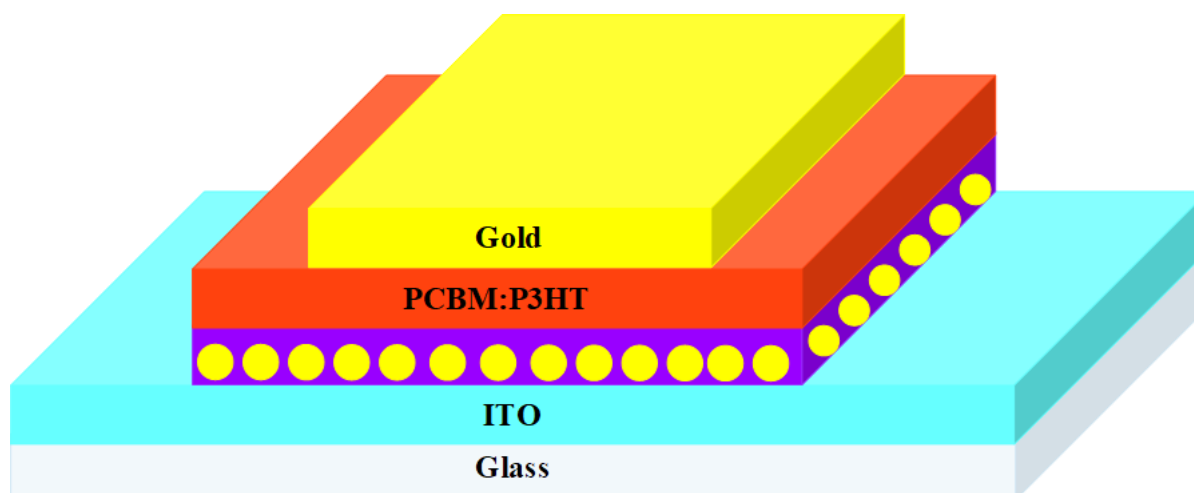


Figure 3.1: Schematic diagram of OSC incorporated with NPs in the PEDOT: PSS

PEDOT: PSS was first filtered through a hydrophilic filter before spin-coated on glass at 3 000 rpm for 30 s. The first solution was without NPs whereas the second contained NPs. The annealing temperatures for both thin films were 120°C for 15 min which was then allowed to cool to room temperature. P3HT and PCBM were dissolved in dichlorobenzene in

a molar ratio of 1:1 and stirred with a magnetic stirrer for 12 h. The P3HT: PCBM blend was spin-coated on top of PEDOT: PSS at 3 000 rpm for 30 s and annealed at 120°C for 5 min. The samples were put in corning glass desiccator for 24 h, to allow natural drying. 100 nm thick Au contacts were thermally evaporated at a working pressure of 4.5×10^{-6} mbar and deposition rate of 0.1 Å/s using a resistive evaporator. The schematic diagram of the solar created above is illustrated in Figure 3.1.

3.5 Characterization

3.5.1 X-ray diffraction (XRD)

X-ray diffraction (XRD) is a popular non-destructive method for studying crystalline phases of materials [5]. It provides details on the material's quality, crystalline phase, orientation, composition, lattice characteristics, faults, stress, and strain. Cu , for example, produces x-rays with $a = 1.789 \text{ \AA}$, while Cu produces x-rays with $a = 1.5406 \text{ \AA}$. When Bragg's law is satisfied, constructive interference occurs when an x-ray beam with a specific wavelength strikes a sample at a specific incidence angle [5, 6],

$$n\lambda = 2d \sin\theta$$

where n is an integer, d is the spacing between diffracting planes, λ is the wavelength and θ is the incident angle. In a typical XRD scan, the collection of d -spacing values gives a distinguishing feature of the samples under examination [7]. The crystal structure of a material can be determined based on the d -spacing of crystallographic planes in the sample [8]. For example, the lattice parameters, $a = b = c$, for a cubic crystal, can be calculated using the following expression,

$$\frac{1}{d^2} = \frac{h^2 + k^2 + l^2}{a^2}$$

where h , k and l are Miller indices and a is lattice parameter. The Miller indices (hkl) are a set of parallel planes in a crystal with d_{hkl} spacing. Data from XRD may be used to compute crystallite size by using the following equation:

$$D = \frac{0.9\lambda}{\beta_{hkl} \cos \theta}$$

where D is the average crystallite size, β is the full width at half-maximum in the 2θ scan and λ is the wavelength of the X-rays and θ is the Bragg's angle [9]. In this study, XRD analysis

was carried out using a German Bruker D2 PHASER X-ray diffractometer with CuK_α radiation (1.5418 \AA) source depicted in Figure 3.2. It is a powder XRD analyser, and the samples were dried first before doing any measurements.



Figure 3.2: Image of German Bruker D2 PHASER X-ray diffractometer

3.5.2 Scanning Electron Microscopy (SEM)

Scanning electron microscopy (SEM) is frequently used to determine the surface morphology of materials at both the micro and nanoscales [10]. The electron gun, a series of electromagnetic lenses, and apertures make up the SEM optical setup. The electron gun emits a concentrated electron beam at a fine probe for surface scanning. For generating an electron beam, the acceleration voltage can be as high as 40 kV, however, for surface scan, 1 kV or less is preferable. When an electron beam reaches the surface of a sample, it is dispersed by atoms, resulting in signals. Signals created include secondary electrons, Auger electrons, distinctive X-rays, reflected electrons, and visible light. Images of the sample morphology are acquired using secondary electrons. In this study, a field emission scanning electron microscope (FE-SEM Zeiss SEM Microscope Crossbeam-540) shown in Figure 3.3 both

acquired by an in-lens detector operating at an accelerating voltage of 2.0 kV were used to examine the surface morphologies of samples. The samples were first dried and coated with carbon under vacuum to improve conductivity and loaded into the chamber.



Figure 3.3: Images of field emission scanning electron microscope (FE-SEM Zeiss SEM Microscope Crossbeam-540)

3.5.3 Transmission Electron Microscopy (TEM)

Transmission electron microscopy (TEM) is a technique for providing high-resolution imaging as well as crystallographic data. Because of the short wavelengths of the electrons used, this technique produces images of material microstructures with much higher magnification and resolution [11]. The beam of focused high energy electrons is transmitted

through a very thin sample, interacting with it as it passes through under ultra-high vacuum conditions. The interaction produced scattered electrons of varying energies, which then generate an image of the sample. Depending on how the electron beam interacts with the material, TEM can produce distinct pictures. The image of an electron diffracted pattern used to investigate crystallography is created by elastic scattering of electrons, with the dark field image coming from one diffracted beam and the bright field image coming from the transmitted beam.



Figure 3.4: Image of field emission gun transmission electron microscope (FEG-TEM, Jeol 2100).

Because the sample must be electron transparent for the beam to pass through and very thin, sample preparation for TEM imaging is particularly complicated. In this study, powders that

settled in the beaker after centrifugation was dissolved in ethanol and sonicated for 15 minutes with an ultrasonic frequency sweeper. A very thin film was formed on the TEM carbon-coated copper grid by drop-casting 1 μm of uniformly dispersed solution with a micro-pipette and drying for at least 30 minutes before loading into the analysis chamber. Electron micrographs and matching selected area diffraction patterns of the samples were captured by field emission gun transmission electron microscope (FEG-TEM, Jeol 2100) illustrated in Figure 3.4.

3.5.4 Raman spectroscopy

Raman spectroscopy is a non-destructive technique for studying a material's vibrational, rotational, and low-frequency modes. It employs electromagnetic waves, most notably infrared light with much longer wavelengths on the order of 10^{-7} m. The vibrational energy of molecules is well-matched by infrared light. Raman spectroscopy is based on the inelastic scattering of monochromatic light, which produces scattered photons with different frequencies than the incoming or absorbed photons [12]. Differences in frequency provide crucial information about the material's vibrational modes. When a laser source interacts with a sample, the sample emits radiation, which is captured by a lens and sent as a signal into a grating monochromator. As a result, the signal is measured using a photomultiplier tube camera before being processed by a computer, which plots the intensity versus the Raman shift.

WITec's Raman microscope alpha300 RAS was used to conduct Raman experiments on all material presented in the thesis. The excitation wavelength was 514 nm with a power of 0.012 W, and the LWX50 and LWX100 microscope objectives were used interchangeably for focusing.

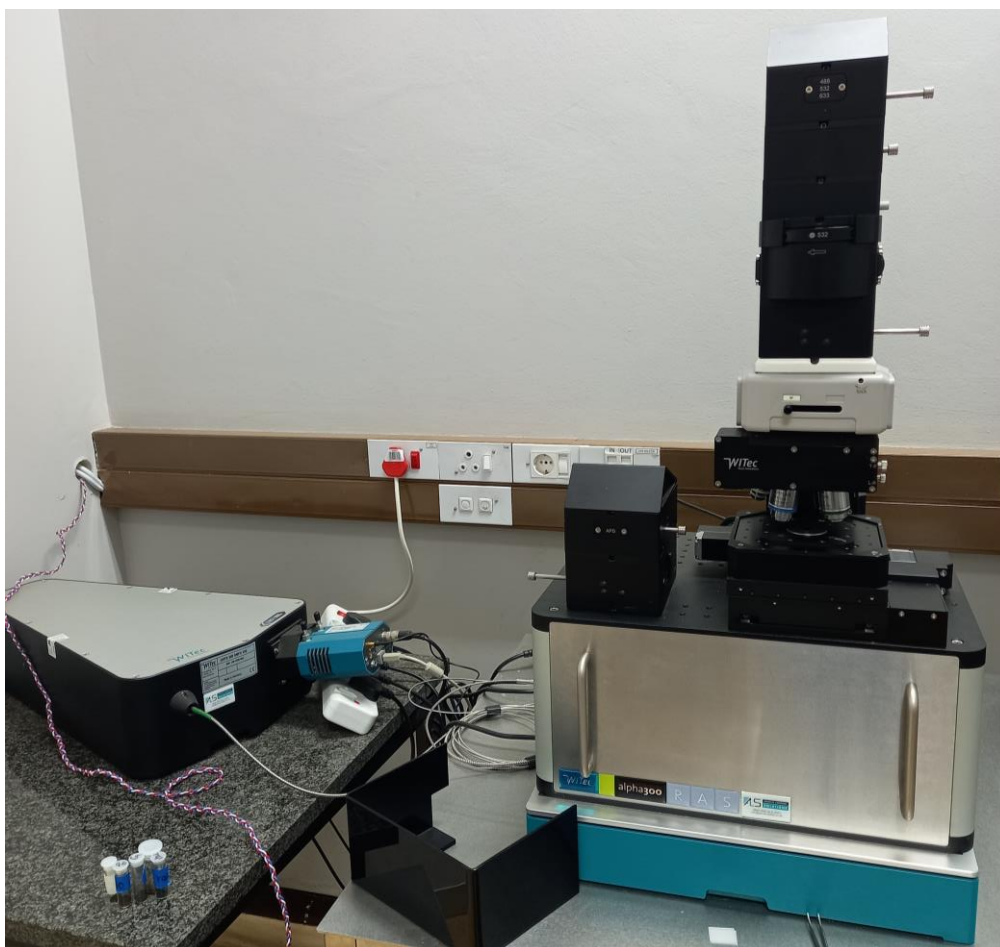


Figure 3.5: WITec's Raman microscope alpha300 RAS

3.5.5 Ultraviolet-visible (UV–Vis)

Ultraviolet and visible spectroscopy (UV–Vis) is a technique for investigating how UV–Vis radiation interacts with a sample. UV–Vis radiations have enough energy to excite an electron from a filled band to a higher unfilled band or orbital [13]. Some of the radiant energy will be absorbed, transferred, and reflected during this electronic transition. UV–Vis absorption measures the amount of light that passes through (I) and compares it to the initial intensity (I_0). The scan range for UV–Vis's absorption is 200 – 400 nm for UV and 400 – 800 nm for vis. The optical absorbance was measured using an Agilent Cary 60 UV–Vis Spectrophotometer in this investigation. The UV is covered by a deuterium lamp with a wavelength range of 190 – 350 nm, while the visible/near infrared area is covered by a halogen lamp with a wavelength range of 350 – 900 nm. Different molecules absorb different wavelengths of radiation in different samples. As a result, the absorption spectrum of semiconductors shows a maximum for a specific incoming wavelength designated as λ_{max} , providing information on the semiconductor's excitonic levels. Baseline correction was done

first, by positioning deionised H₂O and clean ITO substrates and with the coated side towards the light sources, before measuring the absorbance of the NPs and solar cell samples respectively. The light source was kept in front of the deposited surface. The absorbance measurements were done at wavelengths ranging from 200 to 800 nm. For UV–Vis absorption measurements of the P3HT: PCBM photoactive layer, the same approach was used. The Agilent Cary 60 UV–Vis Spectrophotometer has a schematic presented in Figure 3.6.



Figure 3.6: Image of Agilent Cary 60 UV-Vis Spectrophotometer

3.6 Electrical characterization

3.6.1 Dark current-voltage (I-V) measurements

The current voltage (I-V) measurements have been utilised to evaluate the performance of solar cells. By applying a bias to the solar cell, this technique allows for the measurement of current as a function of input voltage. The electrical properties of OSC were investigated using room temperature dark I-V measurements. For measurements, an Ossila Solar Cell I-V Test System /SMU 1 Voltage Source with a current accuracy of $\pm 500 \mu\text{A}$ and voltage scan sizes ranging from -1 V to +1 V were used. The voltage increment was set to 0.02 V with a settling time of 1 μs . The pixel area was chosen between $1 - 4 \times 10^{-3}$. Using the standard

thermionic emission theory, the ideality factor (n), barrier height, series resistance (R_s), and reverse saturation current (I_0) were calculated from the $I - V$ measurement.

3.6.2 Light Current density-voltage ($J - V$) measurements of the solar cells

The $J - V$ measurements of the fabricated OSCs were tested using the Oriel Solar simulator, Oriel® LCS-100TM Small Area Sol1A Series (Oriel Cornerstone, Newport) shown in Figure 3.7. This system consists of a 100 W xenon arc lamp, a reflector, and an optical filter for better spectral collection. A beam homogenizer, variable aperture for irradiance modification, and AM1.5 filter were used to pass light from a Xenon lamp with an incorporated elliptical reflector. Under conventional illumination of 1 sun circumstances (1000 W/m^2), AM1.5, and room temperature, measurements of light $J - V$ were taken. The intensity of irradiance was first calibrated with the 91150V Calibrated Reference Cell and Meter. Each dark measurement was accompanied by a set of light measurements. The scan voltage was swept from -1 V to 1 V.

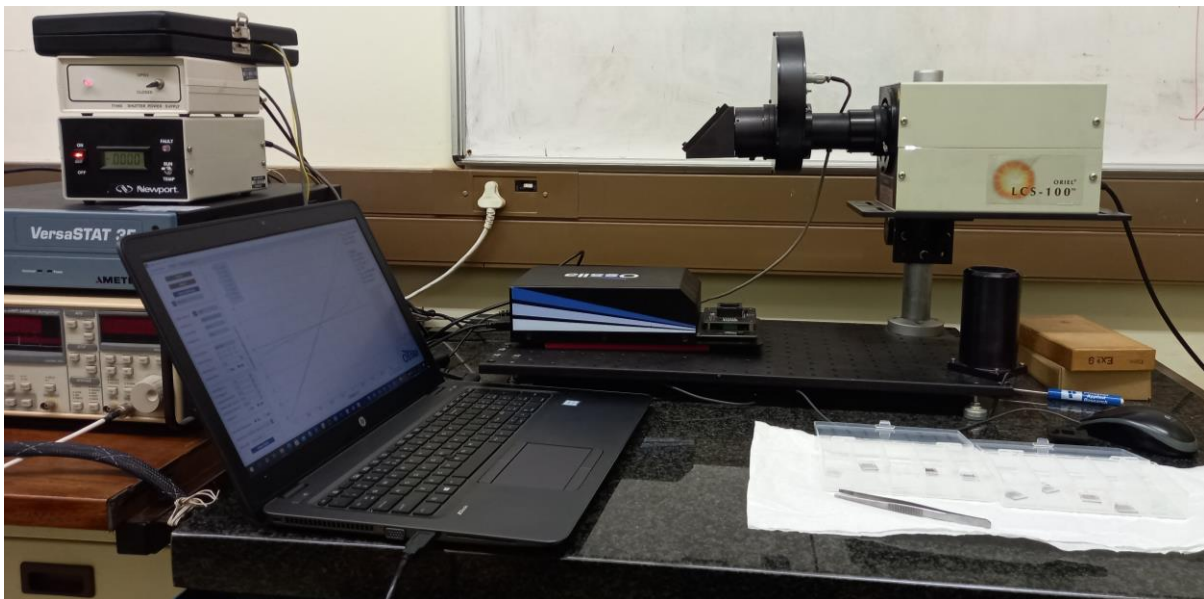


Figure 3.7: Shows a picture of the Oriel Cornerstone, Newport solar simulator alongside the Keysight source measure unit (SMU) connected to a computer.

3.7 References

- [1] R. T. Tom, V. Suryanarayanan, P. G. Reddy, S. Baskaran, and T. Pradeep, "Ciprofloxacin-protected gold nanoparticles," *Langmuir*, vol. 20, no. 5, pp. 1909-1914, 2004.
- [2] R. C. Doty, T. R. Tshikhudo, M. Brust, and D. G. Fernig, "Extremely stable water-soluble Ag nanoparticles," *Chemistry of Materials*, vol. 17, no. 18, pp. 4630-4635, 2005.
- [3] T. M. Dung Dang, T. T. Tuyet Le, E. Fribourg-Blanc, and M. Chien Dang, "The influence of solvents and surfactants on the preparation of copper nanoparticles by a chemical reduction method," *Advances in Natural Sciences: Nanoscience and Nanotechnology*, vol. 2, no. 2, p. 025004, 2011/04/21 2011.
- [4] J. S. Nyarige, T. P. J. Krüger, and M. Diale, "Structural and optical properties of hematite and L-arginine/hematite nanostructures prepared by thermal spray pyrolysis," *Surfaces and Interfaces*, vol. 18, p. 100394, 2020/03/01/ 2020.
- [5] Y. Leng, *Materials characterization: introduction to microscopic and spectroscopic methods*. John Wiley & Sons, 2009.
- [6] B. R. Rehani, P. Joshi, K. N. Lad, and A. Pratap, "Crystallite size estimation of elemental and composite silver nano-powders using XRD principles," 2006.
- [7] T. Hao and R. E. Riman, "Calculation of interparticle spacing in colloidal systems," *Journal of colloid and interface science*, vol. 297, no. 1, pp. 374-377, 2006.
- [8] Y. Onuki *et al.*, "Rapid measurement scheme for texture in cubic metallic materials using time-of-flight neutron diffraction at iMATERIA," *Journal of Applied Crystallography*, vol. 49, no. 5, pp. 1579-1584, 2016.
- [9] V. Uvarov and I. Popov, "Metrological characterization of X-ray diffraction methods for determination of crystallite size in nano-scale materials," *Materials characterization*, vol. 58, no. 10, pp. 883-891, 2007.
- [10] K. Akhtar, S. A. Khan, S. B. Khan, and A. M. Asiri, "Scanning electron microscopy: Principle and applications in nanomaterials characterization," in *Handbook of materials characterization*: Springer, 2018, pp. 113-145.
- [11] M. Winey, J. B. Meehl, E. T. O'Toole, and T. H. Giddings Jr, "Conventional transmission electron microscopy," *Molecular biology of the cell*, vol. 25, no. 3, pp. 319-323, 2014.

- [12] N. Kumar, S. Mignuzzi, W. Su, and D. Roy, "Tip-enhanced Raman spectroscopy: principles and applications," *EPJ Techniques and Instrumentation*, vol. 2, no. 1, p. 9, 2015.
- [13] M. Picollo, M. Aceto, and T. Vitorino, "UV-Vis spectroscopy," *Physical sciences reviews*, vol. 4, no. 4, 2019.

Chapter 4

Results and discussion

4.1 Introduction

In this chapter, colloidal Au, Ag and Cu NPs were synthesised and hybrid Au, Ag and Cu NP-PEDOT: PSS thin films were created. From UV-Vis spectrum, Au, Ag and Cu NPs display LSPR with a wider wavelength tunability window. Despite this appealing LSPR tunability, the integration of NPs in PEDOT: PSS, as well as the characteristics that arise, has not yet been investigated. Structural and optical characterizations of Au, Ag, Cu NPs, PEDOT: PSS, and P3HT: PCBM thin films were carried out using techniques such as transmission electron microscopy (TEM), ultraviolet/visible spectroscopy, Raman spectroscopy, and X-ray diffraction measurements. We compare the findings of various characterisation techniques to see how varying concentrations of NPs alter the optical and structural properties of PEDOT: PSS thin films, offering insights into their potential use in organic solar cells in the future. The electrical properties of the device created above are also discussed.

4.2 Gold and silver nanoparticles

4.2.1 Structural, optical and morphological properties

4.2.1.1 Structural properties

The X-ray diffraction (XRD) pattern of gold nanoparticles has peaks of (111), (200), (220) and (311) shown in Figure 4.1 (a). The peaks were indexed at 39.13° , 44.6° , 64.76° and 76.24° , respectively and these, in turn, represent a face centred cubic (FCC) crystal structure which is consistent with the literature [1-3]. The (111) peak proved to be the most intense and according to Sneha *et al.*, this implies that the growth orientation of the nanoparticles was fixed in its direction [1]. The XRD peaks for the Au NPs were at the same angles which means that the concentration of NaBH_4 did not affect the structure. XRD for Ag NPs also confirmed an FCC structure for both sets with (111), (200), (220) and (311) peaks at 39.46° , 44.94° , 64.79° and 76.22° , respectively, as shown in Figure 4.1 (b). The (111) peak is again the most intense.

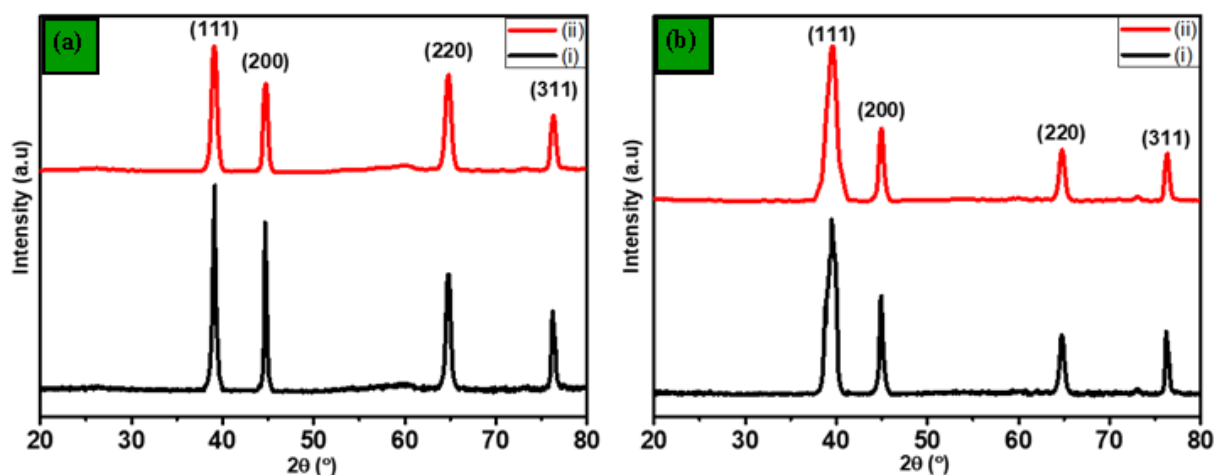


Figure 4.1: XRD patterns of (a) Au NPs with (i) 0.1 M NaBH₄ and (ii) without NaBH₄ and (b) Ag NPs with (i) 10 mM NaBH₄ and 5 mM NaBH₄

The XRD analysis of Au and Ag NPs are tabled in Table 4.1. This was done in order to calculate the crystallite sizes, D-spacing and lattice parameters of the obtained NPs. This was done by profile fitting in order to determine the peak positions and widths in their respective calculations. The crystallite sizes of Au NPs containing 0.1 M NaBH₄ and without NaBH₄ range from 6 to 17 nm and 15 to 26 nm, respectively. Ag NPs have crystallite sizes of between 12 and 17 nm for 10 mM NaBH₄ and 14 to 25 nm for 5 mM NaBH₄. By looking at these results in both NPs, it seems like the lower concentrations of NaBH₄ amount to higher crystallite sizes. There were no crystallographic impurities found in either Au or Ag NPs since the present peaks in XRD all belong to the NPs. This ensures the success of the synthesis of these NPs using chemical reduction.

Table 4.1: XRD analysis of Au and Ag NPs at different concentrations of NaBH₄

Sample	Peak	2theta (deg)	β (deg)	D (nm)	d-spacing (nm)	a (nm)
Au NPs (0.1 M NaBH ₄)	111	39,503	1,319	6,336	0,228	0,395
	200	44,946	0,627	13,561	0,202	0,403
	220	64,774	0,72	12,940	0,144	0,407
	311	76,307	0,576	17,354	0,125	0,414
Au NPs (No NaBH ₄)	111	39,091	0,488	17,102	0,230	0,399
	200	44,712	0,327	26,015	0,203	0,405
	220	64,778	0,616	15,118	0,144	0,407
	311	76,296	0,487	20,515	0,125	0,414
Ag NPs (10 mM NaBH ₄)	111	39,503	0,478	17,482	0,228	0,395
	200	44,946	0,637	13,349	0,202	0,403
	220	64,774	0,73	12,762	0,144	0,407
	311	76,307	0,586	17,058	0,125	0,414
Ag NPs (5 mM NaBH ₄)	111	39,091	0,498	16,758	0,230	0,399
	200	44,712	0,337	25,242	0,203	0,405
	220	64,778	0,626	14,876	0,144	0,407
	311	76,296	0,497	20,103	0,125	0,414

4.2.1.2 Optical properties

The particles synthesized were soluble in water. However, water solubility alone will not be enough for these particles to be effective in solar cell applications. The stability of these nanoparticles in high ionic strength environments is depicted in Figure 4.2. The UV/Vis spectrum of the Au NPs shows an intense peak at 534 nm which broadens as the wavelength increases indicating the agglomerated part of the NPs as shown in Figure 4.2 (a), (i). Doty et al. also found similar results, where agglomeration was observed due to wavelength increase and broadening of the peak [4]. The second spectrum in the Figure 4.2 shows, the intense peak at 534 nm does not broaden which indicates that there is little, or no agglomeration as shown in Figure 4.2 (a), (ii). The second peak indicates the presence of Au nanorods (NRs) from the solution [5]. The UV/Vis absorption spectrum of Ag NPs containing 10 mM of NaBH₄ has a very broad peak between 510 and 750 nm as shown in Figure 4.2 (b) (i). The broad peak indicates the decrease in interplanar spacing between NPs, in agreement with

Doty *et. al* [4]. The ellipsoids also play a big role in the stretched peak. An intense peak at 410 nm for Ag NPs containing 5 mM of NaBH₄ is shown in Figure 4.2 (b) (ii), which means that the plasmonic resonance is centred at that wavelength [4]. The intense peak is due to the lack of agglomeration in the solution.

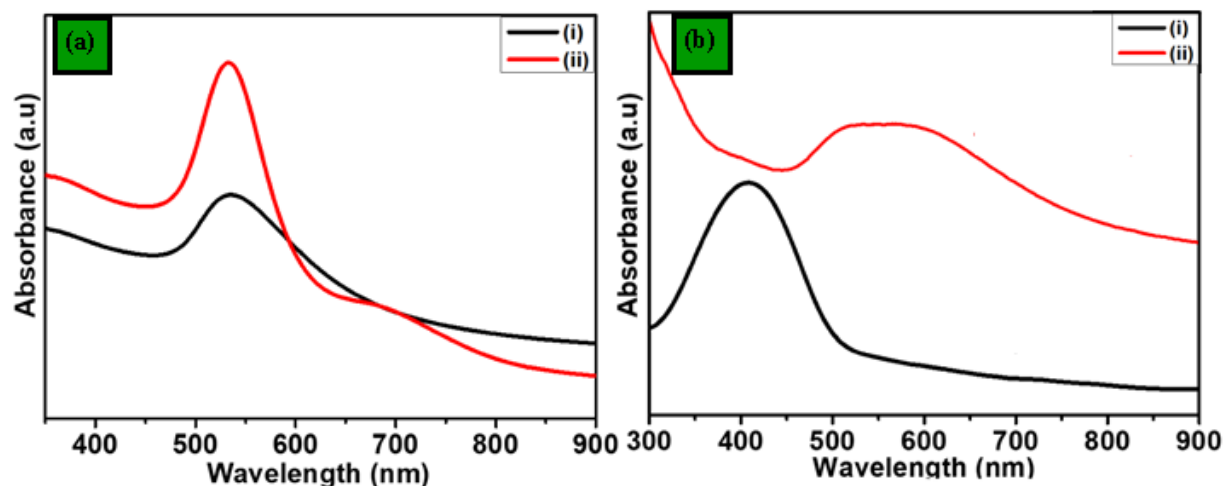


Figure 4.2: UV-Vis spectra of (a) Au NPs with (i) 0.1 M NaBH₄ and (ii) without NaBH₄ and (b) Ag NPs with (i) 10 mM NaBH₄ and 5 mM NaBH₄

4.2.1.3 Morphological properties

TEM images of the water-soluble citrate stabilized Ag and Au nanoparticles are presented in Figure 4.3. Figure 4.3 (a) and (b) show citrate-stabilized Ag nanoparticles produced from two different concentrations of NaBH₄. The particles in Figure 4.3 (a) have a diameter of 12.5 ± 0.4 nm produced from NaBH₄ at a concentration of 10 mM whereas the particles in Figure 4.3 (b) have a diameter of 5.0 ± 1.2 nm and are produced from 5 mM NaBH₄. All the particles are well-separated and spherical in shape.

Water-soluble citrate-stabilized Au nanoparticles produced from two different concentrations of NaBH₄ are illustrated in Figure 4.3 (c) and (d). The particles in Figure 4.3 (c) with a diameter of 17.0 ± 0.4 nm, have been synthesized with 0.1 M NaBH₄. The particles are spherical but not uniformly shaped and agglomerated. The particles in Figure 4.3 (d) with a diameter of 23.7 ± 0.5 nm synthesized without the use of NaBH₄, were formed when the solution was heated to 100°C. Some particles are still agglomerated and lose their spherical shapes. Agglomeration occurs as the particles get larger, where collisions more likely produce ellipsoids rather than spheres [4, 6]. This result is in agreement with Doty *et al.*, who

reported that after the initial nucleation of 1-2 nm Ag clusters, the mechanism for particle growth is aggregation on Ag nanoparticles [4].

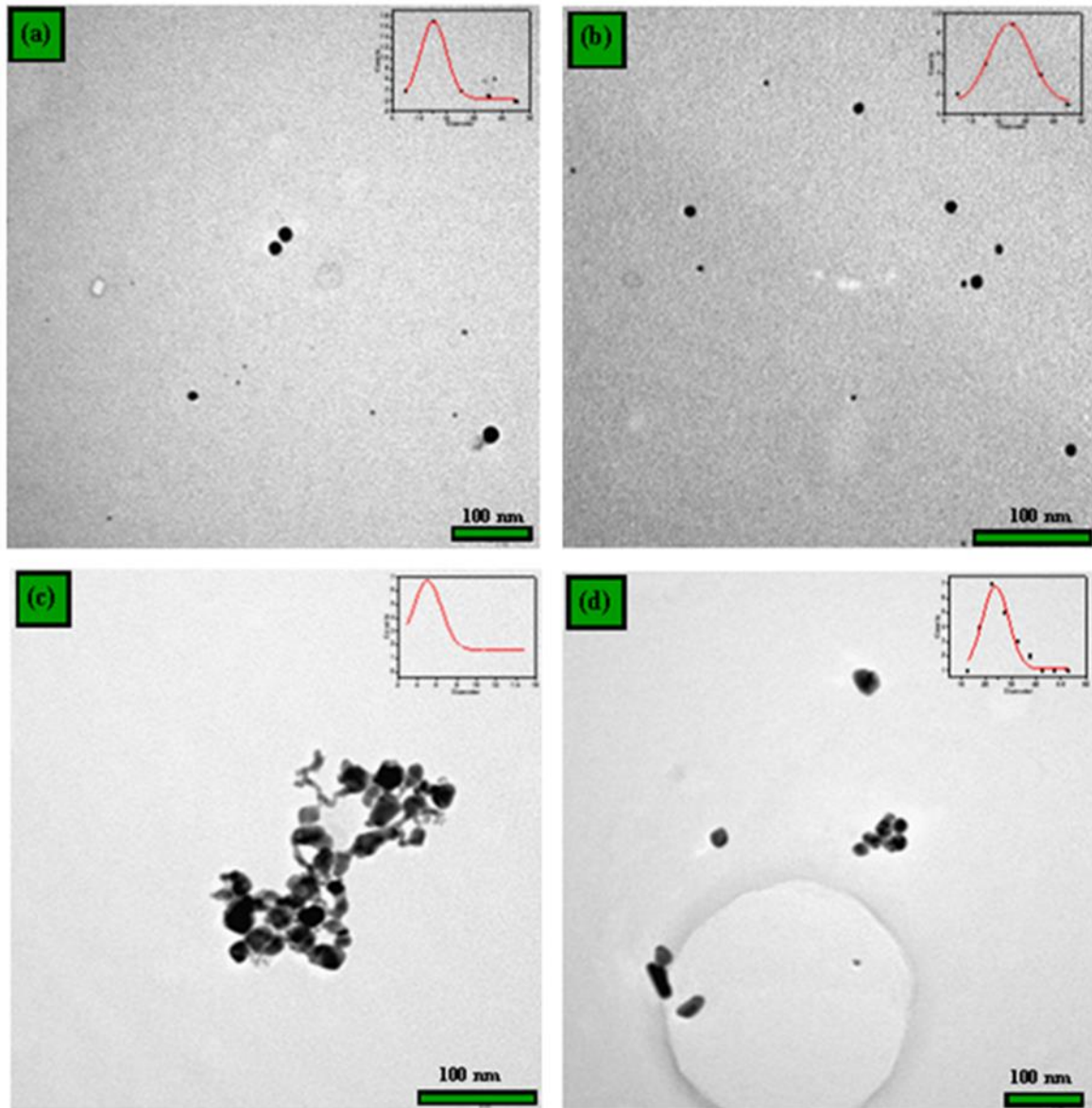


Figure 4.3: TEM images of Ag NPs with (a) 10 mM NaBH₄ and (b) 5 mM NaBH₄ along with Au NPs with (a) 0.1 M NaBH₄ and (b) without NaBH₄

4.3 Copper nanoparticles

4.3.1 Structural, optical and morphological properties

4.3.1.1 Structural properties

X-ray diffraction (XRD) patterns of Cu NPs for different concentrations of CuSO₄ are illustrated in Figure 4.4. All three samples have (111), (200) and (220) peaks indexed at around 42°, 49° and 74° respectively. These diffraction peaks confirm that Cu NPs produced in this study have an FCC crystal structure. The (111) peak has the highest intensity which indicates the crystallinity of Cu NPs [7, 8]. Cu NPs are very vulnerable to oxidation. This means that they can react very well with oxygen (in the atmosphere) to form copper oxides (CuO) and (Cu₂O) which can sometimes be a thin layer, and this happen during synthesis process. The three XRD patterns show no sign of crystallographic impurities in the produced NPs which shows that there was no oxidation that occurred. This may be the result of ascorbic acid (AA) which acted as an antioxidant in the synthesis. Analysis for XRD of Cu NPs are summarised in Table 4.2. The crystallite size increases with 2-theta while d-spacing decreases. The average lattice constant of Cu NPs was calculated to be 0.36 nm [7, 9].

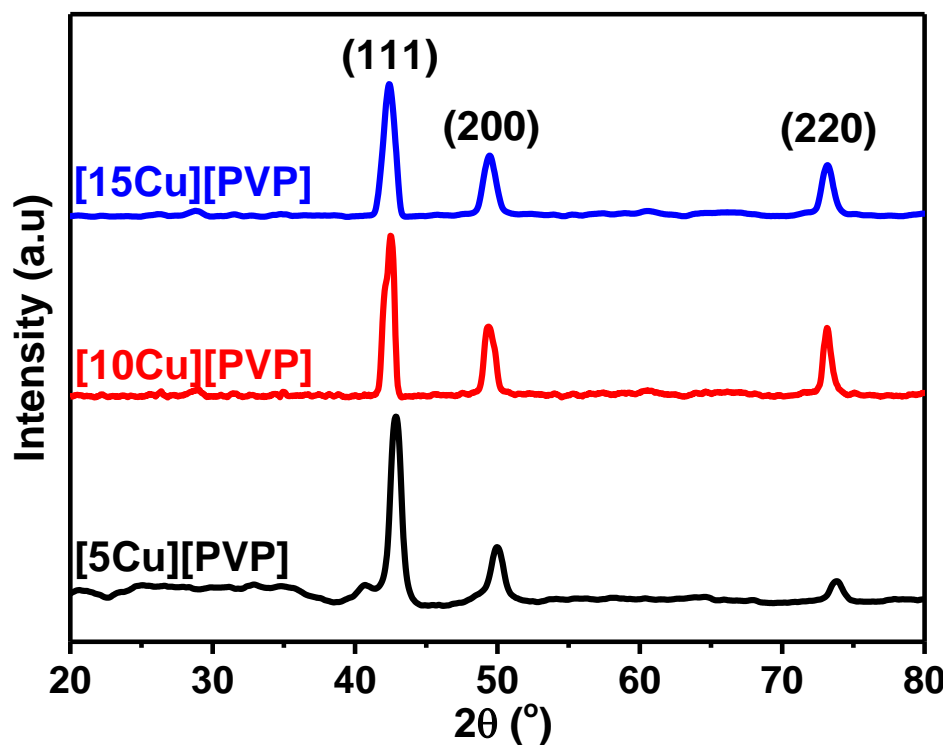


Figure 4.4: XRD patterns of Cu NPs at different concentrations of CuSO₄

Table 4.2: XRD analysis of the obtained Cu NPs

Sample	Peak	2θ (deg)	β (deg)	D (nm)	d-spacing (nm)	a (nm)
[5Cu] [PVP]	111	42,861	0,867	9,737	0,211	0,365
	200	49,976	0,964	8,999	0,182	0,365
	220	74,480	0,714	13,823	0,127	0,360
[10Cu] [PVP]	111	42,412	0,774	10,898	0,213	0,369
	200	49,449	0,846	10,237	0,184	0,368
	220	73,173	0,703	13,925	0,129	0,366
[15Cu] [PVP]	111	42,395	0,914	9,226	0,213	0,369
	200	49,456	1,007	8,598	0,184	0,368
	220	73,184	0,942	10,393	0,129	0,366

4.3.1.2 Optical properties

UV-Vis absorption spectra of Cu nanoparticles are shown in Figure 4.5. Cu NPs have been found to show absorption bands ranging from 500 - 600 nm which is in the (visible) region [10, 11]. However, Pham et al. have reported an absorption band at 618 nm. Muniz-Miranda et al. have also reported an absorption band of 636 nm, and in their conclusion, they said that their Cu NPs were oxidised [12]. The spectra in Figure 4.5 (a) and (b) show were for Cu NPs without AA which was indeed oxidised, this is also shown by the absorption band is 740 and 775 nm. The plasmonic resonance of Cu NPs with 5 mM concentration of CuSO_4 prepared in AA was around 560 nm whereas the ones with 10 and 15 mM CuSO_4 were both at around 562 nm. These absorption bands were not far from each other showing that the concentration did not play a role in the plasmonic resonance. Samim et al. have also observed absorption bands of their Cu NPs at 570 nm [8].

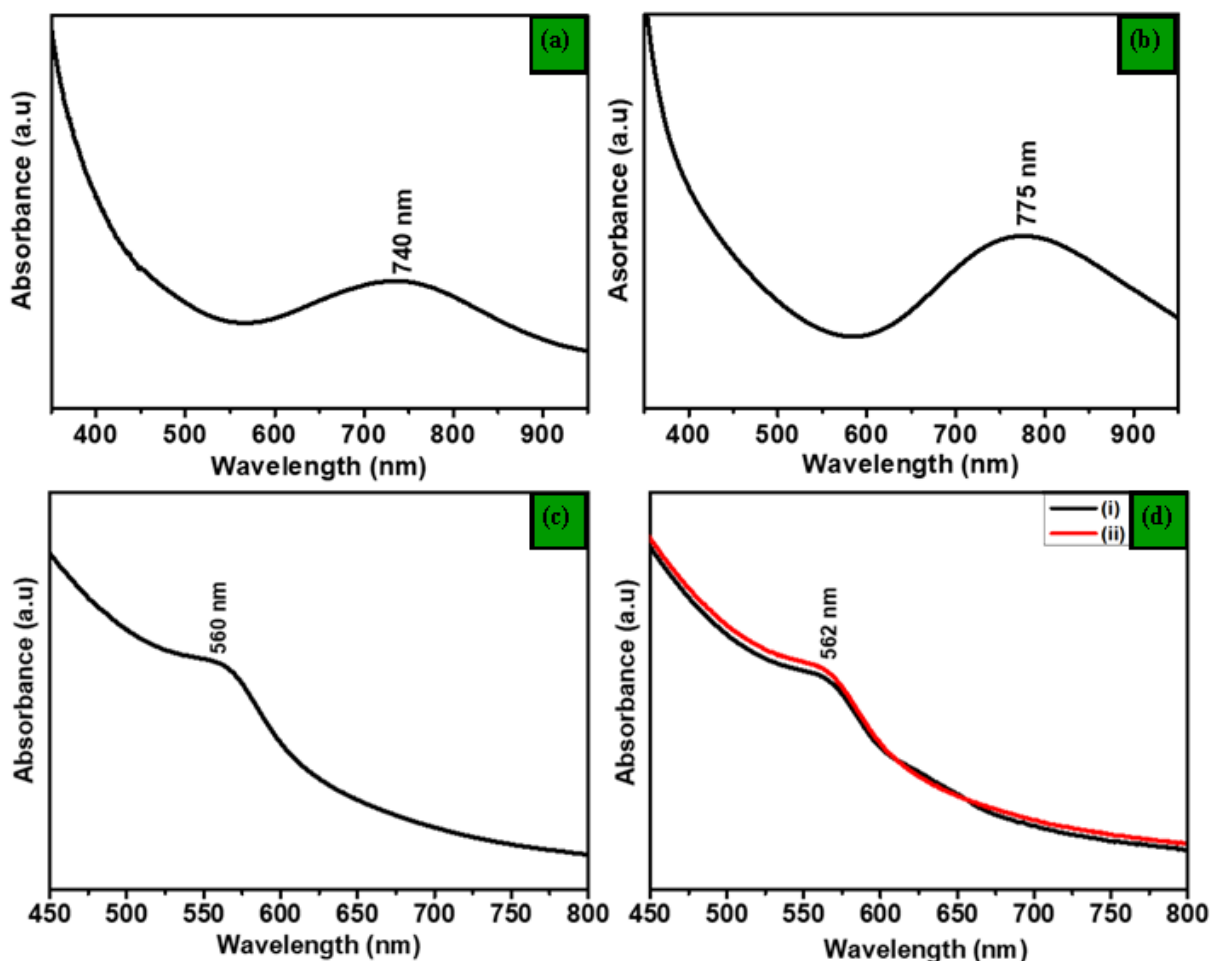


Figure 4.5: UV-Vis spectra of Cu NPs prepared without AA (a) immediately, (b) after 1 day and prepared with AA at (c) 5 mM, (d) (i) 10 mM and (ii) 15 mM CuSO_4

4.3.1.3 Morphological properties

TEM images of the water-soluble Cu nanoparticles with different concentrations of CuSO_4 are displayed in Figure 4.6. Cu NPs produced in this study are approximately spherical. The average grain sizes for Cu NPs containing 5, 10, and 15 mM CuSO_4 are 6.01 ± 0.89 nm, 17.32 ± 0.55 nm, and 32.00 ± 0.75 nm respectively. This suggests that the difference in concentration had a major effect on the size of the Cu NPs since they both increase. However, this effect is brought by the concentration of PVP as a ratio to the concentration of CuSO_4 . PVP works both as a size controller and as a polymeric capping agent because it hinders the nuclei from aggregation through the polar groups, which are strongly adsorbed at the surface of copper particles on the surface with coordination bonds [10].

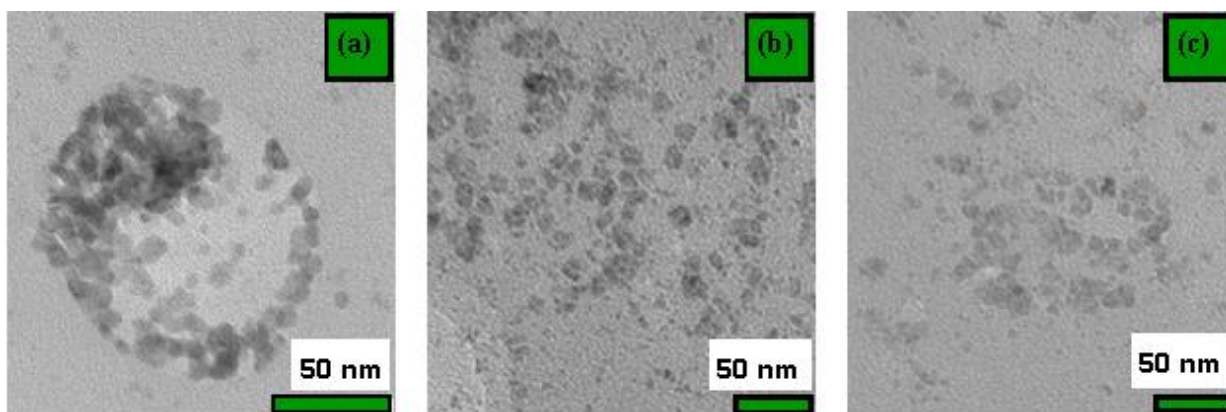


Figure 4.6: TEM images of Cu NPs with AA at (a) 5 mM, (b) 10 mM and (c) 15 mM CuSO_4

4.4 Organic solar cell

4.4.1 Structural, optical, morphological properties, and electrical properties

4.4.1.1 Raman

The Raman spectrum of PEDOT: PSS is illustrated in Figure 4.7 (a). The peaks at 997 , 1108 , and 1572 cm^{-1} , are assigned for PSS. The 449 , 701 , 1267 , 1373 , 1446 , and 1511 cm^{-1} peaks were assigned to the C–O–C deformation, C–S–C deformation [13], $\text{C}_\alpha\text{--C}_\alpha'$ inter-ring stretching, $\text{C}_\beta\text{--C}_\beta$ stretching, $\text{C}_\alpha\text{=C}_\beta$ symmetrical, and $\text{C}_\alpha\text{=C}_\beta$ asymmetrical vibrations modes for PEDOT, respectively [14-16]. The different volumes of Cu NPs have not changed the vibrational bonds but just slightly increased the intensity. The intensity increases with the increase in different volumes. However, the annealing temperatures have shown a decrease in intensity in $140\text{ }^\circ\text{C}$ as the pronounced peak is smaller than 120 and $160\text{ }^\circ\text{C}$.

The Raman spectrum of P3HT: PCBM is shown in Figure 4.7 (d). The most intense peak was at 1467 cm^{-1} which is assigned to $\text{C}_\alpha\text{=C}_\beta$ symmetric stretch mode while 1390 cm^{-1} represents $\text{C}_\beta\text{--C}_\beta'$ inter-ring stretch mode of aromatic thiophene ring [17]. The 731 cm^{-1} is assigned to $\text{C}_\alpha\text{--S--C}_\alpha'$ ring deformation [18]. The other smaller peaks (1099 , 1217 , and 1535 cm^{-1}) are assigned to the $\text{C}_\beta\text{--C}_{\text{alkyl}}$ stretching mode, $\text{C}_\beta\text{--H}$ stretching mode and $\text{C}_\alpha\text{=C}_\beta$ antisymmetric stretch mode, respectively [18, 19]. These results are in agreement with Yadav et al. in which the Raman spectra P3HT: PCBM blend thin films display the same modes as of pristine P3HT [19].

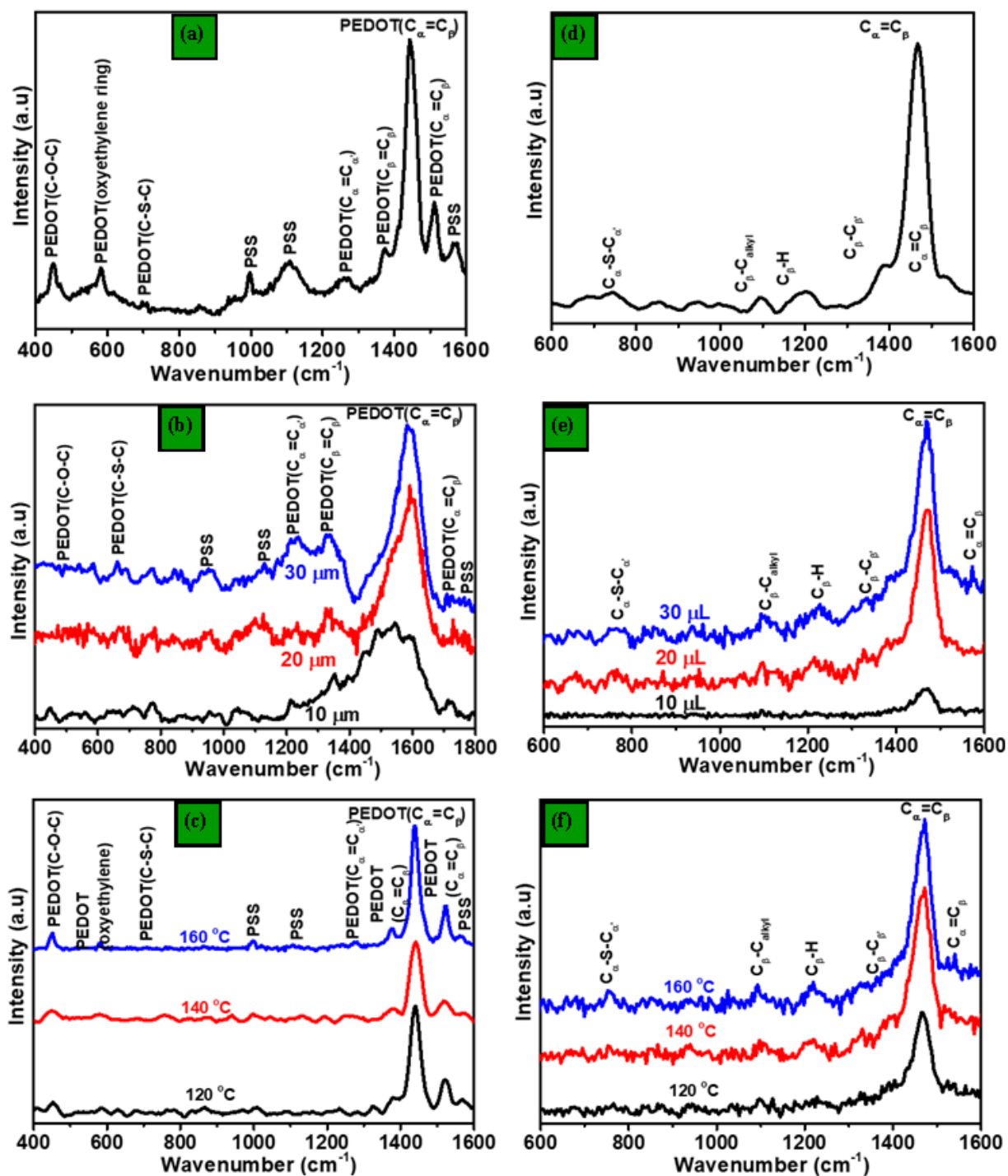


Figure 4.7: Raman spectra of PEDOT: PSS for (a) pristine, (b) different volumes of Cu NPs, and (c) different annealing temperatures. Raman spectra of P3HT: PCBM for (a) pristine, (b) different volumes of Cu NPs, and (c) different annealing temperatures.

4.4.1.2 Ultraviolet-visible

Figure 4.8 presents the UV-Vis spectra of PEDOT: PSS. The pristine PEDOT: PSS is a transparent polymer used in OSCs. This is shown by the absence of absorption peak in Figure 4.8 (a). The incorporation of Cu NPs had an effect on the PEDOT: PSS absorption since these introduced peaks at 533 nm which can be regarded as their plasmonic resonance as shown in Figure 4.8 (b). The increase in the volume of Cu NPs impacted the intensity of the absorption in the polymer. The 30 μL volume was very much higher than the 10 and 20 μL .

The UV-Vis spectra of P3HT: PCBM is shown in Figure 4.9. P3HT: PCBM resulted in a bimodal spectrum as shown in Figure 4.9 (a). P3HT and PCBM absorb at different wavelengths of 448 and 330 nm, respectively. This meant that only P3HT absorbs in the visible range and PCBM absorbs in the UV region. According to Shaban et al. the peak at ~ 487 nm is ascribed to band-to-band transitions inferred from $\pi-\pi^*$ transitions between the allowed highest occupied molecular orbital (HOMO) and the lowest unoccupied molecular orbital (LUMO) of P3HT: PCBM [17, 20]. The incorporation of Cu NPs in the active layer has resulted in the combination of the two peaks of P3HT and PCBM as shown in Figure 4.9 (b).

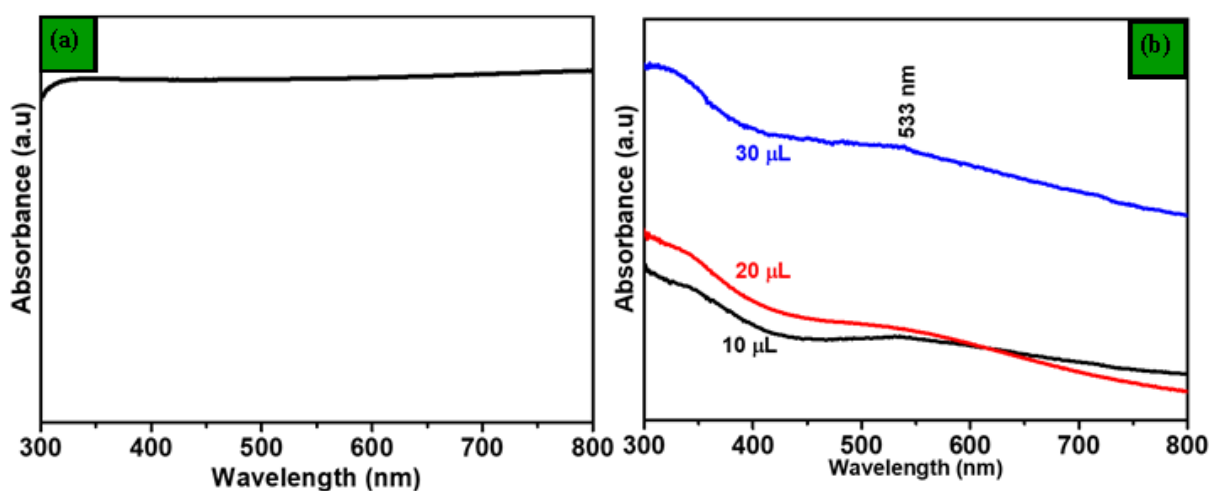


Figure 4.8: UV-Vis spectra of (a) pristine PEDOT: PSS and (b) PEDOT: PSS containing different volumes of Cu NPs

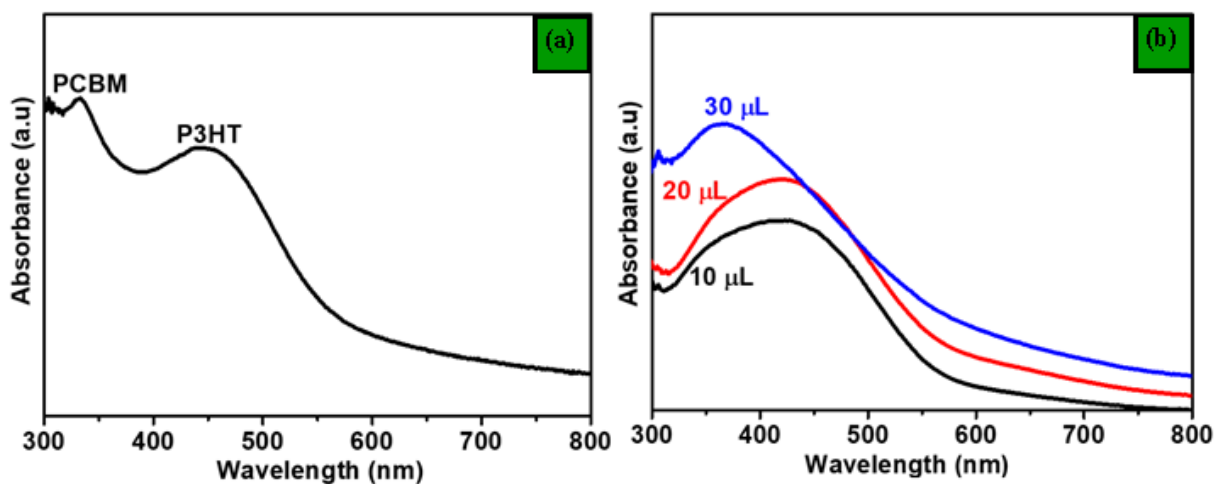


Figure 4.9: UV-Vis spectra of (a) pristine P3HT:PCBM and (b) P3HT:PCBM containing different volumes of Cu NPs

The UV-Vis absorption spectra of P3HT:PCBM containing Cu NPs annealed at different temperatures is presented in Figure 4.10 (a). The same broad peak between 320 and 500 nm present in the spectra of Figure 4.9 (b) is observed as a result of Cu NPs. At high annealing temperature ($>160^{\circ}\text{C}$), this peak displayed a small blue-shift, which might be attributed to the interruption of the structure and the orientation for the P3HT chain ordering due to the heat treatment. Absorption features (S0, S1, S2) corresponding to P3HT excitonic absorption with the participation of Frenkel excitons were found at ~ 602 , 550 , and 510 nm, respectively. Shaban has also observed that these excitonic absorptions correspond to the formation of a singlet exciton, one exciton, one phonon, and one exciton plus two phonons, respectively [20].

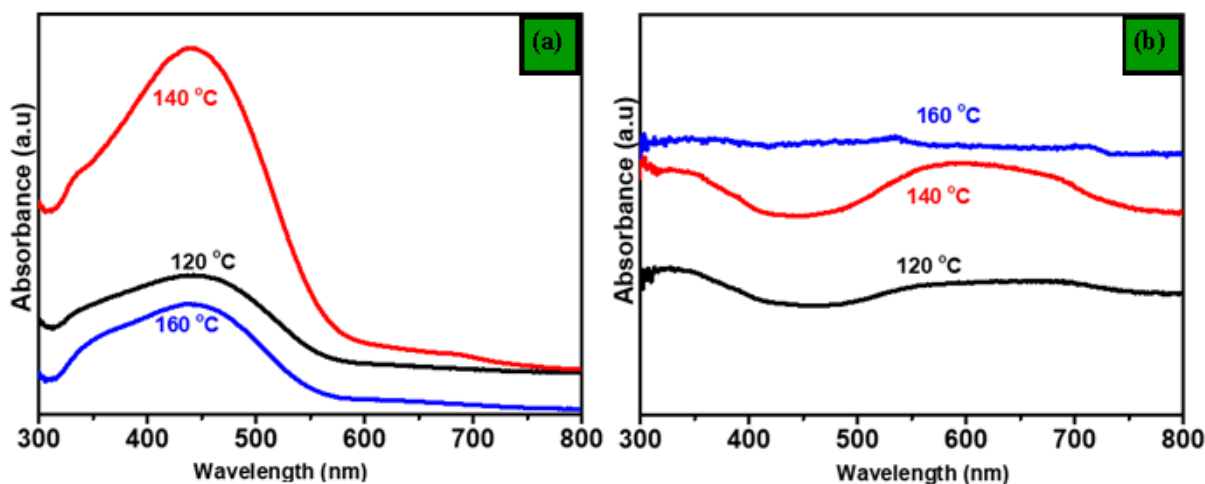


Figure 4.10: UV-Vis spectra of Cu NPs incorporated in (a) P3HT: PCBM and (b) PEDOT: PSS annealed at different temperatures

4.4.1.3 Morphological properties

Scanning electron microscopy (SEM) images of PEDOT: PSS and P3HT: PCBM with Cu NPs at different volumes are presented in Figure 4.11. The images show full coverage of the polymers on top of the ITO without any cracks. This full-coverage was influenced by the viscosity of ethanol ammine, which helped PEDOT: PSS to stick on top of the ITO substrate. The Cu NPs are not visible in any of the P3HT: PCBM polymers in Figure 4.11 (a) – (c). The different volumes of Cu NPs incorporated in PEDOT: PSS can be seen in Figure 4.11 (d) – (f) as white dots. The density of the incorporated Cu NPs increases with the H_{Au}Cl₄ amount. The Au NPs are well dispersed in PEDOT: PSS, with no significant aggregation; moreover, the particles are roughly spherical and have average diameters of 20 to approximately 40 nm. The NPs are uniform in size as it was the same concentration of CuSO₄ which was used to prepare them. The SEM results agree with Hassan et al. who observed similar morphology when they uniformly deposited PEDOT: PSS [21].

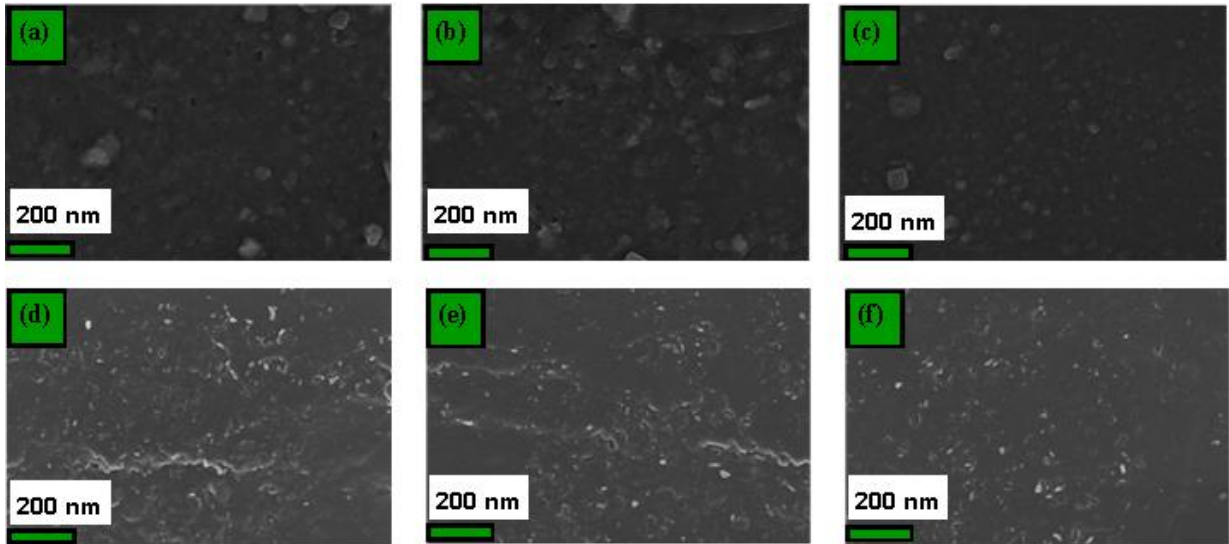


Figure 4.11: SEM images of Cu NPs incorporated in P3HT: PCBM for (a) 10 μL , (b) 20 μL and 30 μL ; and PEDOT: PSS for (d) 10 μL , (e) 20 μL and (d) 30 μL .

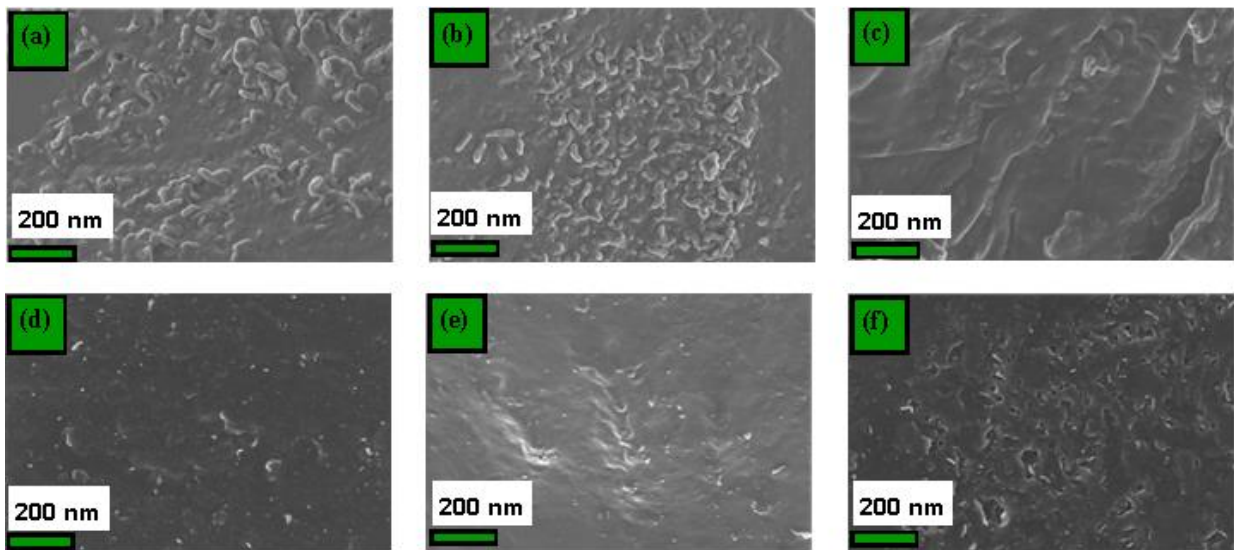


Figure 4.12: SEM images of Cu NPs incorporated in P3HT: PCBM at annealing temperatures of (a) 120 $^{\circ}\text{C}$, (b) 140 $^{\circ}\text{C}$ and 160 $^{\circ}\text{C}$; and PEDOT: PSS at annealing temperatures of (d) 120 $^{\circ}\text{C}$, (e) 140 $^{\circ}\text{C}$ and (f) 160 $^{\circ}\text{C}$.

4.4.1.4 Electrical properties

Figure 4.13 shows the direct measurement of the conductance of the OSC with and without Au NPs measured on the same day of fabrication. As observed in the representative of J–V characteristics of the ITO/PEDOT: PSS: Au NPs/P3HT: PCBM/Ag, the surface resistance of

PEDOT: PSS film reduces with the incorporation of Au NPs into the PEDOT: PSS layer. This is an indication of an enhanced conductivity of the PEDOT: PSS layer when Au NPs are added. The PCE of the OSC devices was improved by increasing the amount of Au NPs in PEDOT: PSS.

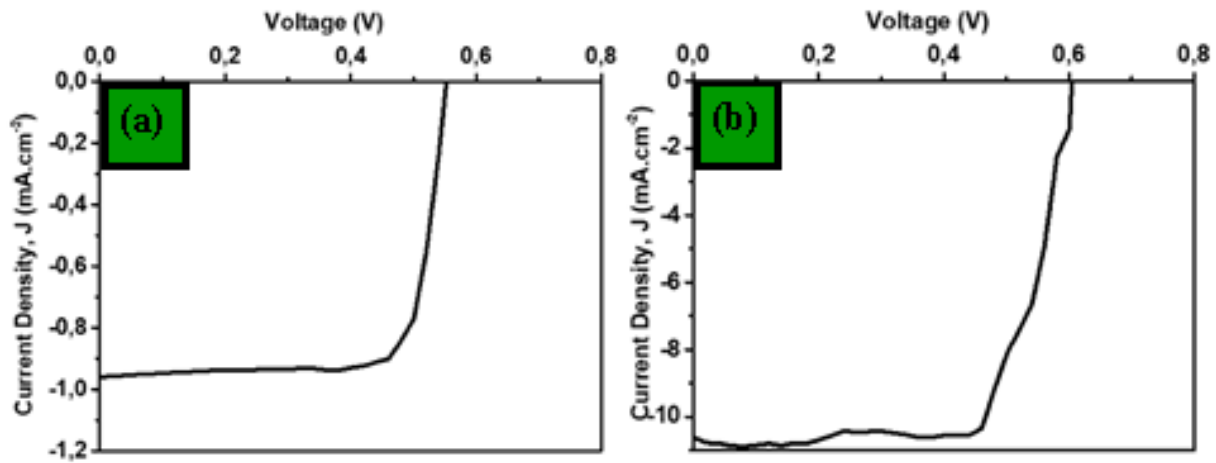


Figure 4.13: J–V characteristic curves under illumination that compared the performance of OSC of (a) pristine and (b) Au NPs

The use of PEDOT: PSS in organic solar cells usually improves the interface between the active layer and the ITO electrode. According to Girtan *et al.*, the use of more conductive films of PEDOT: PSS could lead to free ITO solar cells and consequently to lower cost and longer lifetime full organic solar cells [22]. The Au NPs mixed in the PEDOT: PSS layer is used as hole conductor interface enhancing better extraction of holes after dissociating from the excitons leading to better cell efficiency and even a step towards the realization of an ITO free organic solar cells.

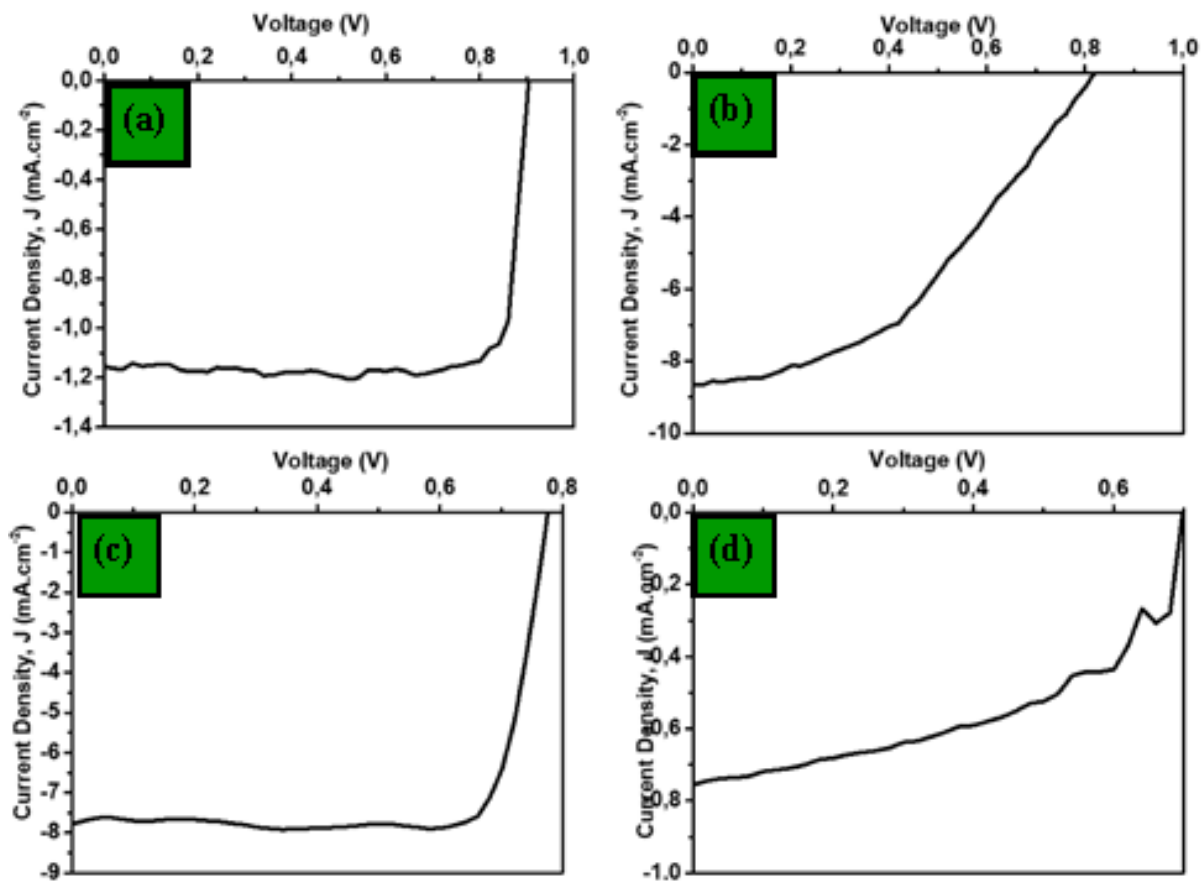


Figure 4.14: J–V characteristic curves under illumination that compared the performance of OSC measured on the same day for (a) pristine, (b) 10 μL Cu NPs, (c) 20 μL Cu NPs, and (d) 30 μL Cu NPs.

Figure 4.14 shows J–V characteristics curves of ITO/PEDOT: PSS/P3HT: PCBM/Ag solar cells with varied Cu NPs concentrations in the PEDOT: PSS and J-V characteristic of the pristine device without Cu NPs for comparison purposes. For further investigation of the effect of the Cu NPs on device performance when they are incorporated into PEDOT: PSS layer. The increase in current density could also be attributed to the modification of the PEDOT: PSS work function by the addition of Cu NPs. Otieno *et al.* have found that the decrease in R_s is attributed to the reduction of the work function of the PEDOT: PSS by Au NP [23]. This is plausible for the 30 μL Cu NPs for which a low intensity of the resonant absorption and high photocurrent is observed.

Figure 4.15 shows the J–V characteristics of devices with different Cu NPs concentrations in the PEDOT: PSS layer after 1 week of fabrication. The pixel area of the device was decreased to 0.001 cm^{-2} from 0.010 cm^{-2} . The detailed OPVs parameters are as outlined in

Table 4.3. The PCE from these results has shown improvement as compared to the previous measurements of the same devices containing Cu NPs.

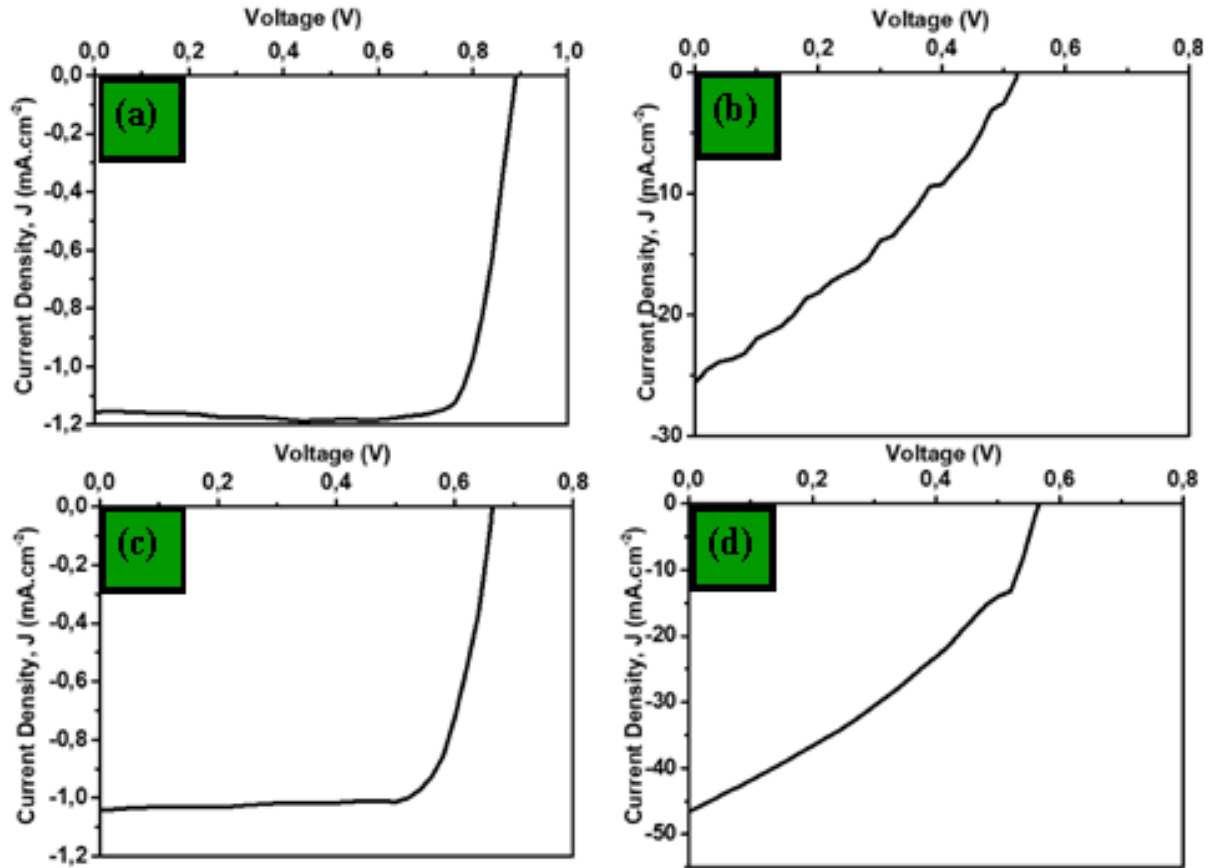


Figure 4.15: J–V characteristic curves under illumination that compared the performance of OSC measured after 1 week for (a) pristine, (b) 10 μL Cu NPs, (c) 20 μL Cu NPs, and (d) 30 μL Cu NPs.

The effect of annealing temperature of the ITO/PEDOT:PSS: Cu/P3HT: PCBM/Ag OSC was investigated. Figure 4.16 shows J-V characteristics curves of ITO/PEDOT: PSS/P3HT: PCBM/Ag solar cells with varied annealing temperatures.

Table 4.3: Summary of the obtained photovoltaic parameters from the J-V data for OSCs

Pixel	PCE (%)	FF (%)	Jsc (mA, cm ⁻²)
P	0,22	27,39	-11,86
Au NPs	5,35	87,62	-7,88
P	0,09	0,19	-8,58
10 μ L Cu NPs	0,14	26,64	-7,71
20 μ L Cu NPs	5,44	93,60	-10,70
30 μ L Cu NPs	0,67	26,68	-11,26
P	3,78	66,59	-7,86
10 μ L Cu NPs	0,54	23,42	-13,81
20 μ L Cu NPs	8,77	87,95	-12,86
30 μ L Cu NPs	0,53	24,95	-16,00
120 $^{\circ}$ C	0,67	26,68	-11,26
140 $^{\circ}$ C	0,90	27,95	-10,88
160 $^{\circ}$ C	0,55	30,52	-15,27

The optimized OSC device at 160 $^{\circ}$ C illustrated V_{oc} of 640 mV and JSC of 10.783 mA/cm². The values of J_{sc} are decreased after 160 $^{\circ}$ C, as shown in Figure 4.16 (c). The small change in J_{sc} at about 160 $^{\circ}$ C indicates that the increase in charge transportations is not accompanied by significant phase separation or breakdown in the active layer. The increase in J_{sc} values varied from 8.821 to 10.783 mA/cm² when increasing the annealing temperature from 130 to 160 $^{\circ}$ C, indicating the improvement of the photon-to-current conversion efficiency (EQE). Based on the obtained values of PCE, FF, V_{oc} , and J_{sc} ; the optimum annealing temperature was 160 $^{\circ}$ C for the preparation of the OSC.

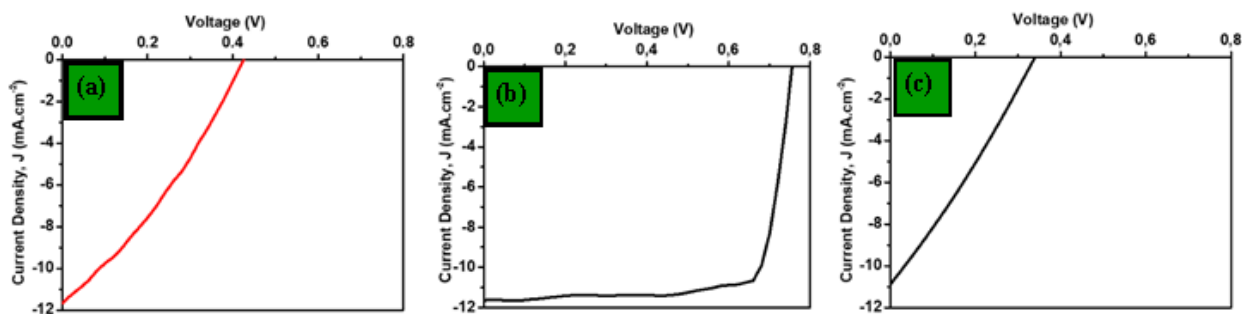


Figure 4.16: J–V characteristic curves under illumination that compared the performance of OSC at annealing temperatures of (a) 120 °C, (b) 140 °C and 160 °C.

4.5 Conclusions

In this study, Au, Ag and Cu NPs have been successfully synthesized using chemical reduction methods. XRD was used to determine the diffraction peaks of the different NPs. Au and Ag NPs both had four peaks between 20 - 80°, namely (111), (200), (220) and (311) which means that they have FCC crystal structures. Cu NPs had (111), (200) and (220) peaks between 20 - 80° which also confirmed the FCC crystal structure. All NPs had their plasmonic resonance in the visible region as confirmed by UV/Vis spectra. TEM has confirmed the presence of these NPs with spherical shapes. Some of the NPs were agglomerated and started to form ellipsoids. Au and Cu NPs were incorporated in the PEDOT: PSS layer as means to improve the absorbance of the organic solar cell (OSC). The different volumes of Cu NPs have affected the absorbance of PEDOT: PSS in which the intensity has increased as observed in Raman and UV/Vis spectra. There was no clear indication regarding the performance of the OSC in reference to the different volumes of Cu NPs and the annealing temperatures however, the 20 μ L had the best performance.

4.6 References

- [1] K. Sneha, A. Esterle, N. Sharma, and S. Sahi, "Yucca-derived synthesis of gold nanomaterial and their catalytic potential," *Nanoscale research letters*, vol. 9, p. 627, 11/23 2014.
- [2] J. Hu, Z. Wang, and J. Li, "Gold nanoparticles with special shapes: controlled synthesis, surface-enhanced Raman scattering, and the application in biodetection," *Sensors*, vol. 7, no. 12, pp. 3299-3311, 2007.
- [3] S. Peng, Y. Lee, C. Wang, H. Yin, S. Dai, and S. Sun, "A facile synthesis of monodisperse Au nanoparticles and their catalysis of CO oxidation," *Nano research*, vol. 1, no. 3, pp. 229-234, 2008.
- [4] R. C. Doty, T. R. Tshikhudo, M. Brust, and D. G. Fernig, "Extremely stable water-soluble Ag nanoparticles," *Chemistry of Materials*, vol. 17, no. 18, pp. 4630-4635, 2005.
- [5] D. T. Nguyen, T. Tran, L. Nguyen Ngoc, L. Long, and Vu, *SYNTHESIS OF GOLD NANOPARTICLES FROM BULK METALLIC GOLD BY A SONOELECTROCHEMICAL METHOD*. 2010.
- [6] D. L. Van Hyning, W. G. Klemperer, and C. F. Zukoski, "Characterization of colloidal stability during precipitation reactions," *Langmuir*, vol. 17, no. 11, pp. 3120-3127, 2001.
- [7] J. Suárez-Cerda, H. Espinoza-Gómez, G. Alonso-Núñez, I. A. Rivero, Y. Gochi-Ponce, and L. Z. Flores-López, "A green synthesis of copper nanoparticles using native cyclodextrins as stabilizing agents," *Journal of Saudi Chemical Society*, vol. 21, no. 3, pp. 341-348, 2017.
- [8] M. Samim, N. Kaushik, and A. Maitra, "Effect of size of copper nanoparticles on its catalytic behaviour in Ullman reaction," *Bulletin of Materials Science*, vol. 30, no. 5, pp. 535-540, 2007.
- [9] T. Thirugnanasambandan and M. Alagar, "X-Ray Diffraction Studies of Copper Nanopowder," *Arch Phys Res*, vol. 1, 03/31 2010.
- [10] T. M. Dung Dang, T. T. Tuyet Le, E. Fribourg-Blanc, and M. Chien Dang, "The influence of solvents and surfactants on the preparation of copper nanoparticles by a chemical reduction method," *Advances in Natural Sciences: Nanoscience and Nanotechnology*, vol. 2, no. 2, p. 025004, 2011/04/21 2011.

- [11] P. Khanna, P. More, J. Jawalkar, Y. Patil, and N. K. Rao, "Synthesis of hydrophilic copper nanoparticles: effect of reaction temperature," *Journal of Nanoparticle Research*, vol. 11, no. 4, pp. 793-799, 2009.
- [12] M. Muniz-Miranda, C. Gellini, and E. Giorgetti, "Surface-Enhanced Raman Scattering from Copper Nanoparticles Obtained by Laser Ablation," *The Journal of Physical Chemistry C*, vol. 115, no. 12, pp. 5021-5027, 2011/03/31 2011.
- [13] A. J. Olivares *et al.*, "Nanostructural Modification of PEDOT:PSS for High Charge Carrier Collection in Hybrid Frontal Interface of Solar Cells," *Polymers*, vol. 11, no. 6, Accessed on: 2019/06//. doi: 10.3390/polym11061034
- [14] P. V. Almeida, C. Izumi, H. F. D. Santos, and A. C. Sant'Ana, "Spectroscopic characterization of PEDOT: PSS conducting polymer by resonance Raman and serss spectroscopies," *Química Nova*, vol. 42, no. 9, pp. 1073-1080, 2019.
- [15] Y. Su, S. Qiu, Y. Liu, D. Yang, H. Zhao, and L. Wang, "PEDOT: PSS-exfoliated Graphene to Improve the Corrosion Resistance of Waterborne Epoxy Coating," *Int. J. Electrochem. Sci*, vol. 14, pp. 4595-4610, 2019.
- [16] S. Xiong, L. Zhang, and X. Lu, "Conductivities enhancement of poly(3,4-ethylenedioxythiophene)/poly(styrene sulfonate) transparent electrodes with diol additives," *Polymer Bulletin*, vol. 70, 01/01 2012.
- [17] P. Veerender *et al.*, "Probing the annealing induced molecular ordering in bulk heterojunction polymer solar cells using in-situ Raman spectroscopy," *Solar Energy Materials and Solar Cells*, vol. 120, pp. 526-535, 2014/01/01/ 2014.
- [18] F. Otieno *et al.*, "Enhancement of organic photovoltaic device performance via P3HT:PCBM solution heat treatment," *Thin Solid Films*, vol. 625, 01/25 2017.
- [19] A. Yadav, A. Upadhyaya, S. Gupta, A. Verma, and C. Mohan, "Solution processed graphene as electron transport layer for bulk heterojunction based devices," *Superlattices and Microstructures*, vol. 120, 06/01 2018.
- [20] M. Shaban, M. Benghanem, A. Almohammed, and M. Rabia, "Optimization of the active layer P3HT: PCBM for organic solar cell," *Coatings*, vol. 11, no. 7, p. 863, 2021.
- [21] G. Hassan, M. Sajid, and C. Choi, "Highly Sensitive and Full Range Detectable Humidity Sensor using PEDOT:PSS, Methyl Red and Graphene Oxide Materials," *Scientific Reports*, vol. 9, no. 1, p. 15227, 2019/10/23 2019.

- [22] M. Girtan and M. Rusu, "Role of ITO and PEDOT: PSS in stability/degradation of polymer: fullerene bulk heterojunctions solar cells," *Solar Energy Materials and Solar Cells*, vol. 94, no. 3, pp. 446-450, 2010.
- [23] F. Otieno *et al.*, "Improved efficiency of organic solar cells using Au NPs incorporated into PEDOT:PSS buffer layer," *AIP Advances*, vol. 7, p. 085302, 08/01 2017.

Chapter 5

Conclusions and future work

This chapter summarises the work done in this study including the experimental and results of the making and observing the plasmonic NPs and OSC devices. Future about this study is also discussed in which we look at what could be done to modify and improve the results.

5.1 Conclusions

This study was based on plasmonic NPs as a way to enhance absorption in the hole transport layer of OSCs. This was done by using the Au, Ag and Cu NPs to enhance the PEDOT: PSS in which the PCE of the overall OSC will increase. A two-step method was used to complete the OSC. First, the plasmonic NPs were synthesized by chemical reduction using their respective salts as precursors and reduced by NaBH_4 in the presence of trisodium citrate as a capping agent. Then, the solution of the NPs was mixed with PEDOT: PSS and spin-coated on ITO substrates along with P3HT: PCBM to complete the devices.

The Au and Ag NPs had similar XRD patterns revealing four peaks between $20 - 80^\circ$, namely (111), (200), (220) and (311) which meant that they have FCC crystal structures. Au and Ag NPs had similar average lattice parameters of 0.41 nm. Both Au and Ag NPs had no crystallographic impurities as there were no other peaks present in their XRD results. The plasmonic resonance of Au and Ag NPs was in the visible spectra as was expected, however, the Ag NPs containing 10 mM NaBH_4 started to absorb in the UV region. The sizes of NPs were all under 100 nm which is the required size for NPs as observed by TEM analysis. The NPs with a lower concentration of NaBH_4 resulted in a smaller grain size. The TEM micrographs also showed that the Au and Ag NPs were spherical in shape.

Cu NPs were synthesized with different concentrations of NaBH_4 . AA was used as an antioxidant since Cu NPs are easily oxidized in liquid. XRD patterns of three different volumes revealed three peaks between $20 - 80^\circ$ which were (111), (200) and (220). This has confirmed that Cu NPs have FCC crystal structures. The average lattice constant of Cu NPs was calculated to be 0.36 nm. The three XRD patterns for Cu NPs did not have any crystallographic impurities as there were no other peaks present, which means that they were not oxidised. The absorption peak of Cu NPs was at around 560 nm which meant that it was in the visible region. The sizes of Cu NPs depended on the concentration of PVP which was

used as a capping agent. As the PVP increased the sizes of Cu NPs decreased as showed by TEM micrographs. Cu NPs synthesized had spherical shapes.

The NPs were incorporated in PEDOT: PSS in order for them to complete the OSC. The Raman spectra for PEDOT: PSS showed the peaks created by the vibrational bonds between $400 - 1600 \text{ cm}^{-1}$. The incorporation of Cu NPs at different volumes has increased the intensity as was shown in the Raman spectra. At different annealing temperatures, $140 \text{ }^\circ\text{C}$ had the lowest intensity. The UV/Vis spectrum of pure PEDOT: PSS had no peak since it is transparent, however after the Cu NPs were incorporated, it started to show plasmonic resonance of the Cu NPs. The Cu NPs are clearly shown on SEM micrographs.

On top of the PEDOT: PSS was P3HT: PCBM which was the active layer of the solar cell. The Raman spectra of PCBM: P3HT showed the peaks which were representing vibrational bonds of P3HT in the $600 - 1600 \text{ cm}^{-1}$ range. The intensities of the spectra increased as the volume of the incorporated Cu NPs increased. The annealing temperatures also had a direct effect on the intensity in Raman spectra. The absorption spectrum of pure P3HT: PCBM had two peaks for PCBM and P3HT at 448 and 330 nm , respectively. Upon the incorporation of Cu NPs, the two peaks became one amorphous peak. The intensity of the absorption spectra increased with an increase in volumes, however, there was no clear relationship with the annealing temperatures. SEM has shown a full coverage morphology of P3HT: PCBM.

The IV measurements were done to investigate the performance of the OSC. The IV curves of the OSCs showed exponential lines which increased in the fourth quadrant. The underperformed OSC did not show a sharp increase as compared to the well-performed OSCs. The pristine OSCs had shown lower PCE than the plasmonic ones. The incorporation of Au NPs showed an increase of 5% as compared to the pristine one. The Cu NPs also showed increases in PCE for the ones measured on the same day, however, the OSC having $20 \text{ }\mu\text{L}$ of Cu NPs improved more by 5% . After one week of creating the OSCs, they were measured again and the pristine and $20 \text{ }\mu\text{L}$ were found to have improved. The annealing temperatures had shown the $140 \text{ }^\circ\text{C}$ having a better performance compared to 120 and $160 \text{ }^\circ\text{C}$.

Although there are still many questions to be answered, the overall study had many successes. The Au, Ag and Cu NPs were successfully synthesized by chemical reduction. Au and Cu NPs were successfully incorporated inside PEDOT: PSS showed by the different

characterization techniques. The PCE of OSC was improved by the incorporation of plasmonic NPs.

5.2 Future work

It has been shown that PEDOT: PSS is acidic and can harm the OSC, this means that new HTL must be found. The Cu NPs which were used in this study were spherical, this means that future studies must also include different shapes which can also be included in different layers of the OSC. Since volume and annealing temperature were the only parameters investigated in this study, future work may include more parameters such as size and time.